A NOVEL APPROACH FOR IDENTIFICATION OF THERMAL AND OPTICAL CHARACTERISTICS FOR THE ACTIVE LAYER OF HIGH POWER PHOTONIC DEVICES

A Thesis

By

Ahmet Mete Muslu

Submitted to the

Graduate School of Sciences and Engineering
in Partial Fulfillment of the Requirements for
the Degree of

Master of Science

in the
Department of Mechanical Engineering

Özyeğin University
December 2019

A NOVEL APPROACH FOR IDENTIFICATION OF THERMAL AND OPTICAL CHARACTERISTICS FOR THE ACTIVE LAYER OF HIGH POWER PHOTONIC DEVICES

Approved by:

Prof. Mehmet Arık, Advisor,
Department of
Mechanical Engineering
Özyeğin University

Prof. Fatih Uğurdağ
Department of
Electrical and Electronics Engineering
Özyeğin University

Asst. Prof. Mete Budaklı
Department of
Mechanical Engineering
Turkish-German University

To my family who always believed in me…

ABSTRACT

Considering a vast amount of electricity consumption for general lighting, the implementation of energy efficient technologies is highlighted in many platforms with the use of light emitting diodes (LEDs). Because of its environmentally friendly nature, LEDs offer a promising solution to minimize inefficient use of energy as the demanding operating conditions present new challenges. While they are taking place in a large number of applications, thermal challenges associated with the operation of LEDs have become a significant issue to address since their performance is greatly affected by thermal conditions. Reduction of lumen output, shorter lifetime and degradation of light characteristics with increasing package temperatures are critical issues that need to be addressed with innovative solutions. Especially in high power LEDs exposed to elevated heat fluxes, standard cooling methods fail to remove produced heat effectively.

As LED systems have been evolving today in a great number of niche applications including automotive lighting, water purification, and skin imaging etc., extensive studies of scientists and engineers in the field have been constantly looking for ways to reduce generated heat loads and maximize the light output to reach the highest efficiency ratios. While the current systems developed over the last years achieved to reach even a 40% LED light extraction efficiency, a higher portion of the electrical input energy of LEDs is still consumed as heat and it hinders their development potential. In addition, the compact size of the LED systems poses some challenges to the reliable characterization of their performance at low uncertainties. Especially, the performance considerations associated with thermal loads over a limited size of LED chips require the effective characterization of these systems for various operational conditions. One of the techniques used for this purpose is that an LED

package is characterized by a decrease in forward voltage with increasing junction temperature. As LEDs are operated at higher junction temperatures, the amount and quality of the light deteriorates significantly, and less efficient use of the LEDs results in additional operating costs and reduced lifetime of LEDs. In fact, accurate identification of thermal behavior of LED packages is one of the essential tasks towards improving the design of LED systems. If thermal characterization of LEDs is accurately done, performance parameters of LED packages are more reliably optimized to yield the highest possible performance ratios. In literature, there are some proposed junction temperature measurement methods such as Peak Wavelength Shift, Thermal (Infrared) Imaging and Forward Voltage Change methods mostly focused on blue LEDs. Most reliable method is cited as Forward Voltage Change Method based on the forward voltage drop over the active layer of an LED as a result of the rise in junction temperature. Therefore, FVCM has been regarded as the main method utilized in the study.

Since the optical behavior of LEDs is significantly affected by thermal conditions of the high-power lighting systems, a better understanding towards optothermal characterization of LEDs with accurate and reliable junction temperature measurements is needed in order to improve the current LED systems. Current junction temperature measurements applied in industry and literature are based on certain assumptions that are questioned in various studies and user application notes. In addition, some issues need to be addressed in open literature for the development of high-power LEDs designed with enhanced thermal and optical performance. These include insightful analysis of the differences in high power red, green and blue LEDs, the impact of an optical path in an LED package, interaction of optothermal characteristics and the LED performance, reliable thermal testing of multi-LED devices.

Thus, this thesis focused on filling these gaps in literature by offering a new measurement approach for junction temperature of multi-LED systems and proposing a highly accurate and rapid junction temperature measurement device.

First of all, identifying thermal, optical and electrical characteristics of high-power LEDs was critical to understand the behavior of these LEDs; therefore, an AlGaInP based red LED was chosen to consider the impact of an LED dome on the chip performance. In addition, prediction capability of thermal imaging method in junction temperature measurements was evaluated in comparison with Forward Voltage Change and numerical thermal methods. It was observed that an LED dome may critically affect the thermal, optical and electrical behaviors of an LED chip. In fact, a 3.7% increase in junction temperature and a 6.1% drop in optical conversion efficiency were found at the normal operation of the red LED after the LED dome was removed. The results were also compared with a blue LED and lower junction temperatures were measured for the red LED at each driving current. The difference in junction temperature became even more noticeable at higher driving currents. Results have shown a good agreement between three different methods with a maximum variation of 6.9%.

Later, three common types of LEDs (Red, Green, and Blue) were studied and their forward voltage drop (V_f) and optical behaviors with varying junction temperatures were compared. It is found that change in optical power with temperature are much higher in red LEDs compared to blue and green chips. On the other hand, a green LED chip experiences the largest change in forward voltage with respect to a unit change in junction temperature when compared to other type of LED chips.

A new approach towards Forward Voltage Change Method was also introduced for the measurement of junction temperatures in multi-LED systems. An Integrating Sphere System was utilized to characterize thermal and optical traits of white multi-

LED systems operating at different electrical conditions. Results show that additional electronic components in a multi-LED system can induce considerable thermal issues since it was determined that heat loads may reach up to total radiant power of LEDs and can decrease the conversion efficiency of a lighting unit by 6.1%. It was also shown that junction temperatures of LEDs can be affected by thermal conditions in the circuit and they need to be determined individually. Thermal imaging technique used to identify local hot spots in the study has shown even higher temperatures at the phosphor layer than the junction region so that the significance of thermal control in a phosphor layer has been understood in order to maximize the thermal and optical performance of a white LED package. As a result, with the proposed analysis and measurement technique in the study, a further understanding has been gained for developing better cooling techniques that will lead to more lumen extraction.

In order to conduct junction temperature measurements of LEDs, there are several thermal characterization and measurement devices in the market. However, existing temperature measurement devices are quite expensive for most of the LED manufacturers, thermal engineers and designers who need to measure only the junction temperature of LEDs. Existing products use a thermal transient test technique for the junction temperature measurement. This technique involves thermal characterization with high sampling rate and resolution of data collection, such as heat flow path construction, die attach qualification, and material property identification, all of which make the product quite expensive. Moreover, that thermal characterization approach uses a structure function based on the assumption of one-dimensional heat flow path. However, in various types of LEDs, there are thermal masses on top of the LED module such as phosphor and attached lens that change the heat flux symmetry. This issue brings difficulties for the interpretation of the structural function and leads to limitations

especially in junction temperature measurements of white LEDs. Consequently, there is a need in the state of the art for affordable, easy to produce and reliable systems which greatly facilitate thermal, optical and electrical design of future LED products with reliable junction temperature measurements.

With the experiences gained on junction temperature measurements, a novel junction temperature measurement device with a compact design and robust operation has been developed. In the thesis, the design and manufacturing process of the device have been described along with the used measurement methodology. After the analysis for the heating and cooling system, the required heating and cooling units are determined, and the corresponding design is presented as the final design. Thus, a highly efficient rapid heating and cooling test chamber is offered to users who demand cost effective thermal solutions.

ÖZETÇE

Önemli miktarda elektriğin dünya genelindeki genel aydınlatma amaçlı kullanımı düşünüldüğünde, ışık yayan diyotların (LED'ler) kullanımı ile yenilenebilir teknolojilerin hayata geçirilmesi her geçen gün daha çok gündeme gelmektedir. Çevre dostu yapısı nedeniyle, LED'ler, verimsiz enerji kullanımını en aza indirmek için zorlu koşullarda dahi umut verici çözümler sunar. Çok sayıda uygulamada yer almaları ile çalışma koşullarında ortaya çıkan zorlu ısıl koşullar, LED’lerin performansını büyük ölçüde etkileyerek önemli bir sorun haline gelmiştir. Işık miktarının azalması, kullanım ömrünün kısalması ve artan sıcaklık seviyeleri ile ışıksal özelliklerinin bozulması, yenilikçi çözümlerle ele alınması gereken kritik konulardır. Özellikle yoğun miktarda ısıl koşullara maruz kalan yüksek güçlü LED'lerde, üretilen ısının standart soğutma yöntemleri ile etkin bir şekilde uzaklaştırılması mümkün değildir.

Bugün LED sistemleri otomotiv aydınlatmaları, su arıtma ve cilt görüntüleme gibi farklı alanlar dahil çok sayıda uygulamada geliştirilirken, bu alanda çalışan birçok bilim adamı ve mühendisler daimî olarak üretilen ısı yüklerini azaltmanın ve ışık miktarı ile verimlilik oranını en üst düzeye çıkarmanın yollarını aramaktadır. Son yıllarda geliştirilen mevcut LED sistemleri, %40'lık bir ışıksal verimliliğe ulaşmayı başarmasına rağmen harcanan elektrik enerjisinin büyük bir kısmı hala ısı olarak üretilmekte ve LED’lerin gelişim potansiyellerini engellemektedir. Bununla beraber, LED sistemlerinin kompakt boyutlarda olması, performanslarının güvenilir şekilde düşük ölçüm belirsizlikleri ile tanımlanmasında bazı zorluklar doğurur. Özellikle, sınırlı boyutlardaki bir LED çipi üzerindeki termal yüklerle ilgili performans hususlarını belirlemek, çeşitli çalışma koşullarında çalışan bu sistemlerin etkin karakterizasyonunu gerektirir. Bu amaçla kullanılan tekniklerden biri LED paketinin artan jonksiyon

sıcaklığı ile ileri gerilimindeki düşüşünün karakterize edilmesidir. LED'ler daha yüksek birleşme sıcaklıklarında çalıştırılırken, ışığın miktarı ve kalitesi önemli ölçüde azalır ve LED'lerin daha az verimli kullanılması, ek işletme maliyetleri ve LED'lerin kullanım ömrünün kısalmasıyla sonuçlanır. Bu doğrultuda, LED paketlerinin termal davranışının doğru tanımlanması, LED sistemlerinin tasarımının iyileştirilmesine yönelik temel gerekliliklerden biridir. LED'lerin termal karakterizasyonu doğru yapılırsa, LED paketlerinin performans parametreleri mümkün olan en yüksek performans oranlarını elde etmek için daha güvenilir bir şekilde optimize edilir. Literatürde önerilen ve çoğunlukla mavi LED'lerin ölçümlerine odaklanan Tepe Dalga Boyu Kayması, Termal (Kızılötesi) Görüntüleme ve İleri Voltaj Değişimi yöntemleri gibi jonksiyon sıcaklık ölçüm yöntemleri vardır. En güvenilir yöntem, jonksiyon sıcaklığındaki yükselişin bir sonucu olarak LED'in aktif katmanı üzerindeki ileri gerilim düşüşüne dayanan İleri Voltaj Değişim Yöntemi olarak gösterilmektedir. Bu nedenle, bu teknik mevcut çalışmada kullanılan ana yöntem olarak kabul edilmiştir.

Yüksek güçlü aydınlatma sistemlerindeki LED'lerin optik davranışı, termal koşullardan önemli ölçüde etkilendiğinden, mevcut sistemleri iyileştirmek için doğru ve güvenilir jonksiyon sıcaklığı ölçümleri, optik ve termal karakterizasyonu gerekmektedir. Endüstride ve literatürde uygulanan güncel jonksiyon sıcaklık ölçümleri, çeşitli çalışmalarda ve kullanıcı uygulama notlarında sorgulanmakta olan bazı varsayımlara dayanmaktadır. Bununla beraber, gelişmiş termal ve optik performansa sahip yüksek güçlü LED'lerin geliştirilmesi için literatürde bazı konuların ele alınması gerekir. Bunlar arasında yüksek güçlü kırmızı, yeşil ve mavi LED'lerdeki farklılıklara yönelik analizler, bir LED paketindeki optik yolun etkisi, optotermal özelliklerin etkileşiminin kapsamlı bir analizi ve çok LEDli sistemlerin güvenilir termal testi sayılabilir. Bu nedenle, bu tez, literatürdeki bu boşlukları doldururken, çok LED'li sistemlerin bağlantı sıcaklığına yeni bir yaklaşım sunmaya ve güvenilir ve hızlı ölçümler gerçekleştiren bir jonksiyon sıcaklığı ölçüm cihazı önermeye odaklanmıştır.

Öncelikle, yüksek güçlü LED'lerin termal, optik ve elektriksel özelliklerini belirlemek, bu LED'lerin davranışını anlamak için kritiktir; bu nedenle, bir LED lensinin çip performansı üzerindeki etkisini araştırmak için AlGaInP tabanlı kırmızı bir LED seçilmiştir. Bununla beraber, jonksiyon sıcaklığı ölçümlerinde Termal Görüntüleme yönteminin ölçüm yeteneği, İleri Voltaj Değişimi ve Hesaplamalı Akışkanlar Dinamiği yöntemleriyle karşılaştırılarak değerlendirilmiştir. Bir LED lensin, LED çipinin termal, optik ve elektriksel davranışlarını kritik derecede etkileyebileceği gözlenmiştir. LED lensinin çıkarılması ile kırmızı LED'in normal çalışma koşullarındaki jonksiyon sıcaklığında %3.7'lik bir artış ve optik dönüşüm verimliliğinde %6.1'lik bir düşüş gözlemlenmiştir. Sonuçlar ayrıca mavi bir LED ile karşılaştırılmış ve her bir sürüş akımında kırmızı LED için daha düşük jonksiyon sıcaklıkları ölçülmüştür. Jonksiyon sıcaklıklarındaki fark, daha yüksek sürüş akımlarında daha da belirgin hale gelmiştir. Sonuçlar, maksimum %6.9'luk bir fark ile üç farklı yöntem arasında iyi bir uyum olduğunu göstermiştir.

Gerçekleştirilen çalışmalarda, farklı renklerde (Kırmızı, Yeşil ve Mavi) ışınım yapan üç LED'in değişen jonksiyon sıcaklıkları ile birlikte gözlemlenen ileri voltaj düşüşü (V_f) ve optik davranışları karşılaştırılmıştır. Optik güç değerlerinin sıcaklık ile değişiminin, kırmızı LED'lerde mavi ve yeşil LED'lere göre çok daha yüksek olduğu bulunmuştur. Öte yandan, jonksiyon sıcaklığındaki birim değişimde, yeşil bir LED çipi, diğer LED çiplerine kıyasla, en büyük ileri gerilim düşüşünü göstermektedir.

Ayrıca, çok LED'li sistemlerdeki jonksiyon sıcaklıklarının ölçümü için İleri Voltaj Değişim Yöntemi'ne yeni bir yaklaşım getirilmiştir. Farklı elektrik koşullarında çalışan beyaz çoklu LED sistemlerinin termal ve optik özelliklerini karakterize etmek için Ulbricht Küresi kullanılmıştır. Sonuçlar, çoklu bir LED sistemindeki elektronik bileşenlerin ürettiği ısı yüklerinin LED'lerin toplam ışıma gücüne ulaşabileceğini ve bir aydınlatma biriminin optik verimliliğini %6.1 oranında azaltabileceğini göstermektedir. Ayrıca LED'lerin jonksiyon sıcaklıklarının devredeki termal koşullardan etkilenebileceği ve ayrı ayrı belirlenmesi gerektiği gösterilmiştir. Çalışmada bölgesel sıcaklık noktalarını tanımlamak için kullanılan termal görüntüleme tekniği, fosfor tabakası üzerinde jonksiyon bölgesinde olduğundan daha yüksek sıcaklıklar göstermiştir. Bu sayede, termal ve optik performansın maksimuma çıkarılması için fosfor tabakasındaki ısıl kontrolün önemi anlaşılmıştır. Sonuç olarak, çalışmada önerilen ölçüm tekniği ve analizi ile daha fazla lümen çıkışına yol açan daha etkili soğutma teknikleri geliştirmek için derin bir anlayış kazanılmıştır.

LED'lerin jonksiyon sıcaklığı ölçümlerini yapmak için piyasada çeşitli termal karakterizasyon ve ölçüm cihazları bulunmaktadır. Bununla birlikte, mevcut sıcaklık ölçüm cihazları, sadece jonksiyon sıcaklık ölçümlerine ihtiyaç duyan LED üreticileri, termal mühendisleri ve tasarımcılar için oldukça pahalıdır. Mevcut ürünler, jonksiyon sıcaklığı ölçümü için zamana bağlı ısıl değişime dayanan test tekniğini kullanır. Bu teknik, yüksek örnekleme hızı ve veri toplama çözünürlüğü gerektiren ve ürünün maaliyetini oldukça arttıran termal karakterizasyon işlemlerini içerir. Ayrıca, bahsedilen termal karakterizasyon, bir boyutlu ısı akış yolunun varsayımına dayanan bir ölçüm tekniğine dayanmaktadır. Bununla birlikte, çeşitli LED paketlerde, ısı akısı simetrisini değiştiren fosfor ve lens gibi termal kütleler vardır. Bu sorun ölçüm tekniği ile türetilen yapısal fonksiyonun (structure function) doğru bir şekilde yorumlanmasında zorluklar doğurmakta ve özellikle beyaz LED'lerin jonksiyon sıcaklık ölçümlerinde sınırlamalara yol açmaktadır. Sonuç olarak, gelecek LED teknolojilerinin; güvenilir jonksiyon sıcaklığı ölçümleriyle ısıl, optik ve elektriksel tasarımını büyük ölçüde kolaylaştıran; uygun maliyetli, üretilmesi kolay ve güvenilir sistemlere ihtiyaç duyulmaktadır.

Jonksiyon sıcaklık ölçümlerinde edinilen deneyimlerle, kompakt tasarımlı ve güvenilir yeni bir jonksiyon sıcaklık ölçüm cihazı geliştirilmiştir. Mevcut tez çalışmasında, cihazın tasarım ve üretim süreci kullanılan ölçüm metodolojisi ile birlikte tarif edilmiştir. Isıtma ve soğutma sistemi analizinden sonra, gerekli ısıtma ve soğutma birimleri belirlenmiş ve ilgili sistem tasarımı sunulmuştur. Böylece, uygun maliyetli termal çözümler isteyen kullanıcılara yönelik yüksek verimli hızlı bir ısıtma ve soğutma düzeneği sunulmuştur.

ACKNOWLEDGEMENTS

First and foremost, I want to thank my advisor Prof. Dr. Mehmet Arik for all the support and opportunities that he provided during my undergraduate and graduate studies at Ozyegin University. It has been a great honor to be one of his students since my first year at university. I also thank him for sharing his knowledge and experience at every opportunity and keeping our motivation high even during the most challenging times. His legacy and perspective will always remain as a source of motivation to keep our flag upright as ARTgroup family.

The members of the ARTgroup have also contributed immensely to my personal and professional development at Ozyegin University. I feel truly lucky to work under supervisions of Arzu Aras, Dr. Enes Tamdogan, Dr. Thamer Khalif Salem and Assistant Prof. Mete Budakli with whom I had all valuable discussions. I also thank to all my colleagues at EVATEG and ARTgroup for their contributions to my work, having great friendship and lifelong support. I specially thank to Burak Ozluk, Onuralp Isil, Enes Oksuz, Ceren Cengiz and Alper Saygin for all unforgettable conversations and discussions during all the works we had together.

I extend my deepest appreciation to my family for all their love, support and encouragement no matter what. I especially thank them for teaching me that being a good man and respecting others is what matters most.

I thankfully acknowledge the funding sources that made my M.Sc. thesis possible. I was funded by the Scientific and Technological Research Council of Turkey (TÜBİTAK) during my research and none of these would be possible without the utilization of great resources at Ozyegin University and EVATEG Laboratories. I am really appreciated to be allowed to use all necessary facilities in my research.

TABLE OF CONTENTS

LIST OF FIGURES

LIST OF TABLES

NOMENCLATURE

GaAs	Gallium Arsenide
GaAsP	Gallium Arsenide Phosphide
GaP	Gallium Phosphide
AlGaAs	Aluminium Gallium Arsenide
AlGaInP	Aluminum Gallium Indium Phosphide
GaN	Gallium Nitride
InGaN	Indium Gallium Nitride
LED	Light Emitting Diodes
RGB	Red, green, blue
CTE	Thermal expansion mismatch
CCT	Correlated color temperature
CRI	Color rendering index
FVCM	Forward voltage change method
TIM	Thermal imaging method
IR	Infrared
PCB	Printed circuit board
R^2	Coefficient of determination
DUT	Device under test
PLC	Programmable Logical Controller
EES	Engineering Equation Solver
PID	Proportional-integral-derivative
EVAtherm	Proposed junction temperature measurement system

IoT	Internet of Things
CFD	Computational fluid dynamics
Si	Silicon
Au	Gold
Al	Aluminum
x	Measurement data of an independent variable
x_n	Measurement data of the nth independent variable
$\bar{x}$	Average of measurement data
x_k	Measurement data of an independent variable
X_i	Input value that affects the measurement result
$\bar{X}$	Average of input values
y	Output value
OP	Objective parameter to be measured
n	Total number of measurements
σ_x	Standard deviation of measurement data
$\sigma_{\bar{x}}$	Mean standard deviation
$t_{(n-1),95\%}$	Student t-distribution
P_x	Precision limit
P	Final precision error
P_n	Precision error of a group of data
B_x	Bias error
B	Final bias error
B_n	Bias error of a group of data
R	Resolution

A	Accuracy
U_x	Absolute uncertainty
$U_n = U_{x_n}$	Absolute uncertainty of the nth independent variable
U_{R_x}	Relative uncertainty
U	Extended measurement uncertainty
$u(x_i)$	Standard measurement uncertainty
$u_c(y)$	Compound uncertainty
$u^2(x_i)$	Uncertainty magnitude
a_i	Reference uncertainty value
S	Experimental standard deviation value
$S_{\bar{q}}$	Standard measurement uncertainty
S_q	Experimental standard deviation
c_i	Sensitivity coefficient
k	Coverage factor
V_{f_c}	Forward voltage data at the calibration phase of measurements
V_{f_t}	Forward voltage data at the actual test phase of measurements
T_{j_c}	Junction temperature data at calibration phase of measurements
I_{p_c}	Pulse current magnitude at the calibration phase of measurements
I_{p_t}	Pulse current magnitude at the actual test phase of measurements
t_{p_c}	Pulse current duration at the calibration phase of measurements
t_{p_t}	Pulse current duration at the actual test phase of measurements
I_t	Driving current magnitude at the actual test phase of measurements
U_{OP}	Uncertainty of objective parameter to be measured

U_{T_j}	Absolute uncertainty of junction temperature at the actual test phase
$U_{V_{f_c}}$	Absolute uncertainty of forward voltage data at the calibration phase
$U_{V_{f_t}}$	Absolute uncertainty of forward voltage data at the actual test phase
$U_{T_{j_c}}$	Absolute uncertainty of junction temperature data at calibration phase
$U_{I_{p_c}}$	Absolute uncertainty of pulse current magnitude at the calibration phase
$U_{I_{p_t}}$	Absolute uncertainty of pulse current magnitude at the actual test phase
$U_{t_{p_c}}$	Absolute uncertainty of pulse current duration at the calibration phase
$U_{t_{p_t}}$	Absolute uncertainty of pulse current duration at the actual test phase
U_{I_t}	Absolute uncertainty of driving current magnitude at the actual test phase
Pr	Prandtl number of water
$K_{bend,180}$	Correction coefficient for 180° bend
$K_{bend,90}$	Correction coefficient for 180° bend
K_{valve}	Correction coefficient for valves
$K_{orifice}$	Correction coefficient for orifices
$n_{bend,180,oven}$	Number of 180° bend in oven
$n_{bend,90,oven}$	Number of 90° bend in oven
$n_{valve,oven}$	Number of valves in oven
$eoverD$	Ratio of surface roughness to hydraulic diameter
Re	Reynolds number of water
f_{oven}	Friction factor in oven

Characters with units

g	[m/s^2]	Acceleration of gravity
P_{air}	[kPa]	Air pressure
P_{water}	[kPa]	Pressure at which water properties are evaluated
ΔP	[Bar]	Pressure drop between inlet and outlet of water
$\delta P_{total,pascal,oven}$	[Pa]	Pressure drop in oven in Pa
δP_{total_oven}	[Bar]	Pressure drop in oven in Bar
T_a	[°C]	Ambient temperature
T_b	[°C]	Board temperature
T_j	[°C]	Junction temperature
$T_{initial}$	[°C]	Initial temperature
T_{final}	[°C]	Final temperature
δT	[°C]	Temperature difference of water between inlet and outlet
ΔT^1	[°C]	Temperature difference between LED junction and ambient
ΔT^2	[°C]	Temperature difference of water between inlet and outlet
δT_{lm}	[°C]	Logarithmic mean temperature difference
T_{mean}	[°C]	Mean temperature
$T_{water,in}$	[°C]	Inlet water temperature
$T_{water,out}$	[°C]	Outlet water temperature
$T_{air,in}$	[°C]	Inlet air temperature of heat exchanger
$T_{air,out}$	[°C]	Outlet air temperature of heat exchanger
T_{in}	[°C]	Inlet temperature of water
T_{out}	[°C]	Outlet temperature of water

V_f	[V]	Forward voltage
E_{in}	[W]	Input power
Er	[W]	Radiant power
E_{LED}	[W]	Input power to LEDs
E_{PCB}	[W]	Input power to PCB
P	[W]	Power
Q	[W]	Heat generation
Q_{dot}	[W]	Cooling power needed
Q_{Al}	[J]	Energy required to change by ΔT_{Al}
Q_{air}	[J]	Energy required to change by ΔT_{air}
Q_{total}	[J]	Total energy required to change by ΔT_{total}
W_{pump}	[W]	Required pumping power
ρ	[kg/m^3]	Density of water
c_v	[J/kg-K]	Specific heat capacity of water
k	[W/m-K]	Thermal conductivity of water
μ	[Pa.s]	Dynamic viscosity of water
υ	[m^2/s]	Kinematic viscosity of water
e	[m]	Surface roughness
D_{holes}	[m]	Hydraulic diameter of holes
$L_{channel}$	[m]	Channel length
$A_{channel}$	[m^2]	Cross section area of channels
$\dot{V}_{1,oven}$	[m^3/h]	Volumetric flow rate in m^3/h
$\dot{V}_{2,oven}$	[L/min]	Volumetric flow rate in L/min
$\dot{V}_{3,oven}$	[gpm]	Volumetric flow rate in gpm

$\dot{V}_{m3s,oven}$	[m^3/s]	Volumetric flow rate in m^3/s
$V_{mean,oven}$	[m/s]	Mean velocity of water in oven
$h_{major,oven}$	[m]	Major head loss in oven
$h_{minor,oven}$	[m]	Minor head loss in oven
$h_{total,oven}$	[m]	Total head loss in oven
R_{th}	[K/W]	Thermal resistance
C_{th}	[J/K]	Thermal capacitance
$Goal_{rate}$	[K/min]	Aimed cooling rate
$t_{process}$	[s]	Time required for cooling by ΔT_{air}
U	[W/m²-K]	Total heat transfer coefficient
$lumen$	[lm]	Luminous flux
-	[lm/W]	Luminous efficacy
-	[nm]	Dominant wavelength
A_{hx}	[m^2]	Required heat exchanger surface area
V_{al}	[m^3]	Volume of aluminum chamber
V_{air}	[m^3]	Volume of air in the chamber
ρ_{Al}	[kg/m^3]	Density of aluminum
ρ_{air}	[kg/m^3]	Density of air
c_{Al}	[J/kg-K]	Specific heat of aluminum
c_{air}	[J/kg-K]	Specific heat of air
m_{Al}	[kg]	Mass of aluminum volume
m_{air}	[kg]	Mass of air volume

CHAPTER I

INTRODUCTION

1.1 Historical Evolution of Lighting

Over the centuries, the emergence and evolution of lighting have shaped the most fundamental life habits of society in almost every aspect from enriched lifestyle of humanity to productive industrial practices. From the very first lighting sources to today’s multi-purpose lighting technologies, lighting technology has undoubtly come a long way to be more reliable, practical and effective than its ancestors.

Figure 1: Old lighting sources (Pantheon, torch, candles, gas lamp) ([1] –[3])

Historical evolution of lighting sources dates back to significant use of lighting with smart use of daily light through an architectural style as observed in “Pantheon” built during Roman Empire. Initial attempts to man-made lighting dates back to around 70,000 years ago with the emergence of torches which carried its main principles to later advancement of lighting sources. As commonly seen in early days of history, fire has been widely used for lighting with the effective use of tubes and chimneys.

However, a critical advancement in lighting was achieved with the discovery of the wick and the production of candles with the impact of Greeks and Romans on Egypt culture as early as the fourth century B.C [4].

Industrial revolution has offered a big jump for the modern progress of lighting technology. Gas lamps and electric lamps discovered in this era has formed the basis for later advancements. Shortly after gas lamps were discovered in England in 1790, they had been seen in different cities and the streets of the Europe and the United States. As they fundamentally changed the structure of cities, they also laid the foundation of environmental issues leading to the wide production of hydrocarbon fuel resources and establishment of giant gas companies. In the early years of 1900s, gas lamps were widespread across European and American streets and houses, but the discovery of electric light deeply challenged the use of gas lamps and put it into end in daily life uses. After a while, gas lamps were only seen in some touristic places or recreational areas to attract people’s attention.

Figure 2: Incandescent, high intensity discharge, compact fluorescent lamps ([5]– [7])

Thomas Edison was the inventor who developed an effective electric light bulb that replaced the gas lighting used especially in houses. His invention in 1879 was termed as “incandescent bulb” and it was working in a deep vacuum with a high-resistance illuminant (“filament”) made of bamboo [8]. His continued works resulted in elongated lifetime of incandescent bulbs and revolutionized the society to use electricity as the main source of lighting in a wide range of applications. With electricity being widely used to produce light, alternative lighting sources with increased efficiency have been introduced respectively including the fluorescent lights and high intensity discharge (HID) lamps. Incandescent light technology was further improved in this competition with the introduction of the tungsten filament and the mercury-vapor light.

HID lamps gained a huge popularity during the 20th century with various kinds of products such as fluorescent, mercury-vapor, high pressure sodium and metal-halide lamps. Main working principle of these was based on the generation of visible light as a result of transferring electrical current between electrodes in a glass container with an inert gas inside. However, this technique was wasting almost all electrical energy as heat only to produce a small fraction of light and it was quite inefficient in terms of economic and environmental aspects.

Early attempts in the beginning 20th century to improve radio detectors paved a new way to produce light without requiring the conventional bulbs, heating up any filament and wasting too much energy. Light Emitting Diodes (LEDs) were a game changer concept for light generation since light was being produced with a totally new technique in newly developed semiconductor materials which formed a solid-state device. Although low power LEDs were utilized for very basic tasks in early days, understanding unique advantages provided with LEDs has resulted in a huge popularity and market for LEDs in many modern life applications by addressing critical issues in economy and environment.

1.2 Historical Background of LEDs

Electroluminescence phenomenon, which is the technology behind how LEDs work, was discovered in the early years of the 20th century. Briefly, this phenomenon is defined as the creation of light by passing the electrical current through a suitable semiconductor material capable of producing light with certain electrical and optical properties.

The first observations of the light emitting diode were made in 1907 by a British engineer H.J. Round, who was working at Marconi to investigate and improve the performance of radio detectors at that time. Radio detectors were made of certain crystals (silicon carbide) and Round had noticed the light generation after he applied a current to his detectors. While Round was the first person who found electroluminescence phenomenon, he also observed the change of the color with different voltage applications at various crystals and realized the impact of the voltage on the light output across the junction. These findings were published in 1907 in “Electrical World” in the name of the report “A Note on Carborundum” [9].

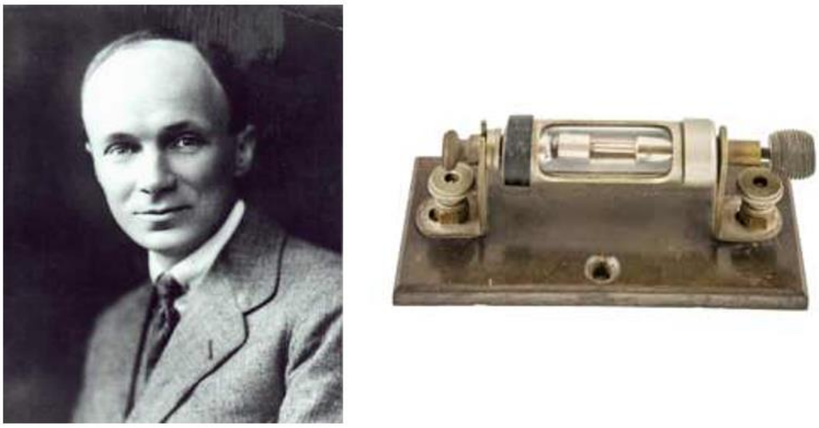

Figure 3: H.J. Round and his cat's whisker detector ([9], [10])

Between 1924 and 1930, Russian radio researcher Oleg Vladimirovich Losev published significant findings related to the invention of LED with the initial works on silicon carbide diodes. His research continued with understanding current-voltage behavior of the LEDs, temperature effects on the emission, and the dependence of the LED spectra on the driving current. Thus, although LEDs were not practically created at that time, Losev’s works provided a deeper understanding of the operation of LEDs and helped later inventors during the development of LEDs [11].

A major progress in light-emitting diodes was realized in 1960s. During their works on a laser diode, Robert Biard and Gary Pittman accidentally discovered that Gallium Arsenide (GaAs) emitted infrared light with the application of an electrical current. Following their invention, they filed a patent on GaAs LED and their company Texas Instruments initiated the first release of commercial infrared LEDs. However, the first LEDs were not visible to human eye since the wavelength spectrum of infrared region is beyond the visible region. Thus, these LED were not practical to use at that time [12].

The first visible LED was invented by Dr. Nick Holonyak from General Electric Company in 1962. Holonyack developed gallium arsenide phosphide (GaAsP) material and he used it as a substrate for the diode to have a wider bandwidth that produces the red visible light. With this achievement, LEDs found a practical use and Holonyack was named as “Father of the Light-Emitting Diode”. After the invention of Holonyack, LEDs were mainly used in indicators or small power applications in laboratories or electronic equipment; however, their price was enormously high (around $200) at that time [11], [13].

Figure 4: N. Holonyak and blue LEDs ([14], [15])

Holonyack’s earlier graduate student M. George Crawford achieved to improve the brightness of red LEDs pretty much (ten times higher than previous red LEDs). He also invented the first yellow emitting LED using gallium arsenide phosphide in the diode when he was working for the Monsanto Company. Thus, the Monsanto Company became the first company to release the visible LEDs on the market on a large scale. This significantly cut the LED price in these years [12]. Between 1960 and 1970, M. George Crawford, Russell D. Dupuis and Nick Holonyak played a significant role in commercialization of light emitting diodes (LEDs).

In 1970s, new materials for LED semiconductors were explored and utilized. With the advancement in semiconductor material technology and new processing techniques, the cost of single LEDs was remarkably lowered to around $0.05 and this brought new opportunities for LEDs to become more common in other applications other than in only indicators [12]. Dr. Jean Hoerni’s works at Fairchild Semiconductor on planar process for semiconductor chip production and packaging techniques contributed a lot to the drop in prices and increased popularity of LED devices. Pure green light was also produced in the mid-1970s by using only Gallium Phosphide. Although LEDs became much more affordable in 1970s, they were not a plug-and-play technology yet and their use was very limited until 1990s [13].

In 1980s, ten times brighter red, yellow, orange and green LEDs were invented with the developments in semiconductor materials and LEDs started to be considered as a viable lighting solution for various applications. The light output of LEDs was further enhanced with the experiments on newly produced materials of semiconductor diodes including Aluminium Gallium Arsenide (AlGaAs) and Aluminum Gallium Indium Phosphide (AlGaInP) (with doubled light output compared to AlGaAs) [9].

Although a variety of colors with high brightness were obtained, blue light was not produced reliably until 1994 due to material growth problems and semiconductor doping issues. In fact, growing larger crystals and forming quality p-n junctions suitable to the production of blue light were impossible in previous years. Therefore, GaP as a semiconductor material was the main focus of researchers instead of GaN material in these years. With the advancement in material technology and fabrication techniques, Shuji Nakamura invented the first powerful blue LED with Gallium Nitride and shortly after; high-intensity blue and green LEDs appeared with the use of Indium Gallium Nitride [16].

The progress in LED technology and the invention of blue LEDs paved the way for the invention of white LEDs as well. Combination of red, green and blue LEDs and phosphor coating techniques over the blue LEDs enabled the production of white LEDs. The invention of efficient blue LEDs and the development of white LEDs with blue LEDs was a huge step in lighting history to provide bright lighting and significant energy savings. As a result, Isamu Akasaki, Hiroshi Amano and Shuji Nakamura were awarded to receive the Nobel Physics Prize in 2014 with their invention of blue light-emitting diodes and their contribution to the efficient white light emission with solid-state devices.

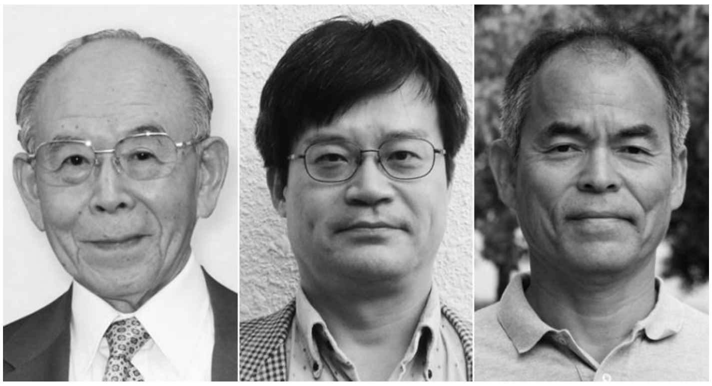

Figure 5: I. Akasaki, H. Amano, S. Nakamura [17]

Advancement in LED lighting technology led to the development of LED products with higher light intensities but minimum power requirements over the years. In 2001, 3,590 traffic lights were converted to the LEDs in Santa Monica, USA and saved around $90,000 annually in energy costs [18]. The U.S. Department of Energy and many other governments recognized the importance of LEDs in cutting worldwide energy expenses and put it into implementation as one of their effective policies. Especially, the use of white LEDs in general lighting was considered to be both cost-effective solution for many businesses and environmentally friendly choice for the planet. Compared to traditional lighting sources such as incandescent products, LEDs were found to consume less energy by 80% and operate 25 times longer [16]. Thus, LEDs are shown to be much more efficient than conventional light sources.

1.3 Advantages of LEDs

As LED systems have more penetrated in various indoor and outdoor lighting applications, the demand for having more efficient LED products with less power consumption has also gradually increased over this decade. Due to recent improvements, LEDs have gained outstanding traits over its conventional counterparts in terms of efficiency, optical performance, lifetime, durability, and safety. As a result, LEDs rapidly replaced their conventional counterparts, and they took an extensive part in various application areas including displays, mobile devices, medical services and automotive lighting, etc. ([19]-[22]).

Figure 6: LED products with different designs and uses in daily life ([23]-[25])

Especially, generating white light with blue LEDs has found a great use in indoor and outdoor lighting, display and automotive lighting applications and eventually enabled a great reduction in worldwide energy expenses. To exemplify, when a 9W ENERGY STAR certified LED bulb is compared with a 43W halogen bulb with the same brightness, estimated energy cost of an LED product is found to be almost five times less than the energy cost of a halogen bulb (LED: $1.26 per year, Halogen: $6.02 per year) [26].

The growing interest towards LEDs has greatly enhanced over the last two decades with better capabilities in LED packaging that resulted in an elongated lifetime, higher energy efficiency and increased lumen amount. LEDs with their superior characteristics and outstanding growth potential have been one of the hot topics for many researchers over the last two decades. Policymakers and government authorities also support this growing interest to reduce energy consumption and encourage a better use of the limited energy resources for a sustainable future. It has been reported that lighting industry plays a very significant role in sustainability since indoor and outdoor lighting applications constitute around 21% of total energy consumption [27]. The role of LEDs in lighting industry is even more remarkable. It is foreseen that energy savings with LEDs could reach up to 348 TWh by 2027 compared to the energy saving with no LED use. This corresponds to the electrical power output of 44 huge electric power plants each of which produce 1000 MW energy. Thus, with the ongoing use of LEDs, total savings over $30 billion USD is estimated at the current electrical prices [28].

Figure 7: Comparison of a 9W ENERGY STAR certified LED bulb with a 43W Halogen bulb emitting the same amount of light [26]

Considering their high efficiency, exceptional reliability, low power consumption and environmentally friendly nature, LEDs exist not only in a traditional lighting field but also in many other interesting applications such as automotive [22], displays [29], visible light communication (VLC) [20], medical diagnosis [21] and skin imaging [30] etc.

A recent statistical data published in 2019 shows the projection of global light-emitting diode (LED) market size from 2019 to 2023 and the market size is expected to reach around 98.5 billion USD as seen in Figure 9 [31].

As one of the LED technology giants, CREE’s net revenue is represented in Figure 10 from the fiscal year of 2015 to the fiscal year of 2019. The company achieved to go beyond over 1 billion USD dollars in net revenue in 2019 [31].

Figure 8: Various application areas of LEDs ([23]-[25])

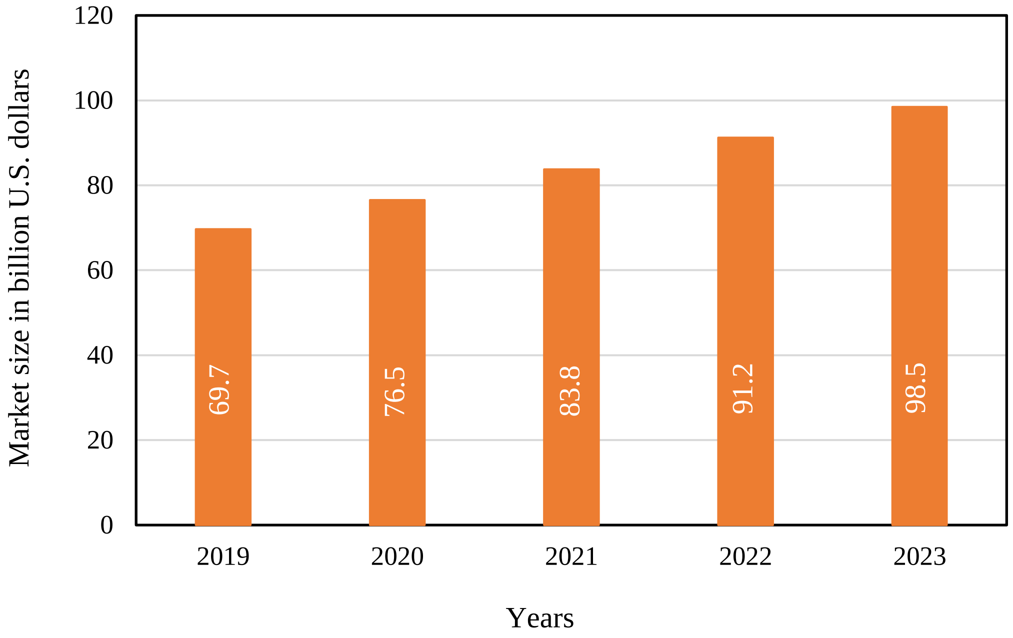

Figure 9: Global LED lighting market size from 2019 to 2023 [31]

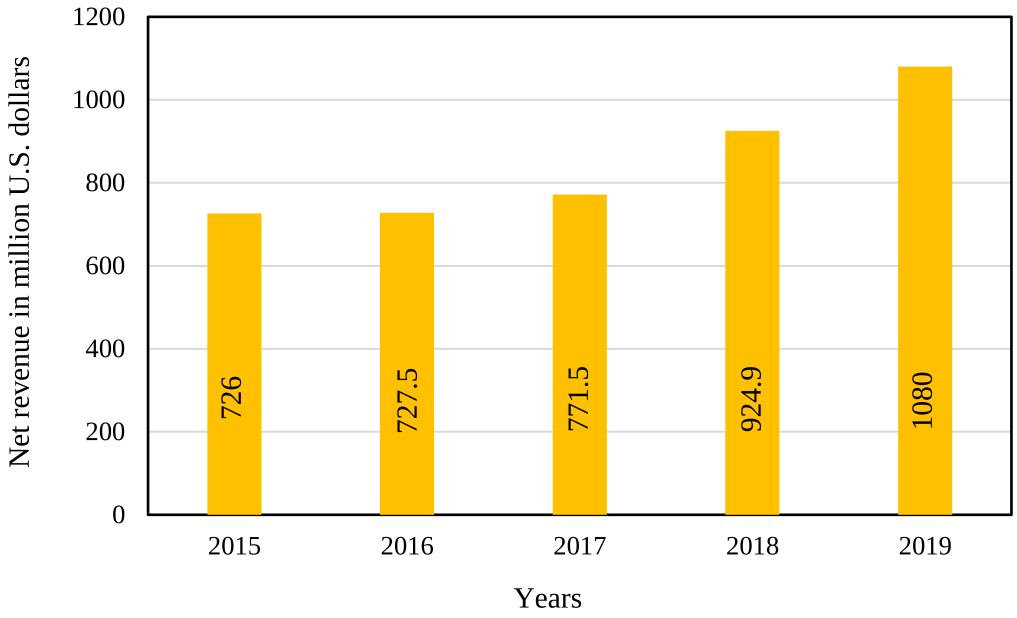

Figure 10: CREE’s net revenue from fiscal year of 2015 to fiscal year of 2019 [31]

Today, general illumination with LEDs is achieved either by incorporating red, green and blue LEDs in an LED package or incorporating phosphor over a blue LED die inside an epoxy resin [32]. While the users who demand a large color gamut and variable color options typically choose RGB LEDs in their applications, phosphor coated white LEDs are more preferred when a higher efficiency is considered [33]. However, both LED types require better handling of thermal issues since light output, efficiency, color and wavelength characteristics of LEDs are all greatly affected by generated heat loads [34].

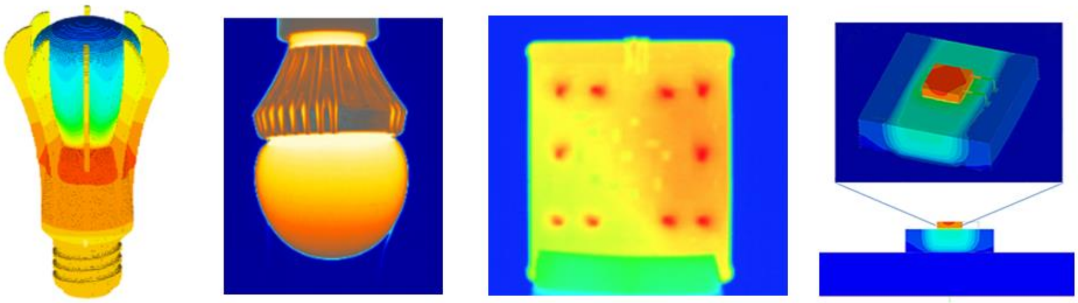

Figure 11: Thermal issues in LEDs ([35]-[36])

In order to address thermal issues in LEDs, understanding the working mechanism of LEDs and interaction of thermal and optical characteristics of LEDs is critical. Thus, the following sections are dedicated to working mechanism of LEDs and thermal issues in LEDs.

1.4 Working Mechanism of LEDs

Diodes are semiconductor circuit elements and light-emitting diodes are sort of diodes which emit light when a voltage is applied on it. In LEDs, semiconductor material may differ depending on the desired color of light output. Normally, atoms are strongly bounded each other inside the semiconductor material which does not allow any free electron to move and conduct electric current. Semiconductor materials mostly have impurities which are atoms of another material and the process of adding these atoms is called “doping”. By changing the doping ratios, different conduction rates can be obtained with the change of charge balance inside the material. After doping process, a semiconductor which has extra electrons is called N-type semiconductor while a semiconductor with extra holes is called P-type semiconductor. It is important to note that while free electrons move from a negative charged area to positive charged area, holes move from a positive charged area to negative charged area.

When no voltage is applied, electrons in N-type semiconductor jump from hole to hole moving from N-type area to P-type area. When there is no voltage applied to diode, along the junction, a depletion zone occur over the junction since the electrons from N-type area fill the holes from P-type area. The size of the depletion zone determines the bigness of the insulating layer between P and N type areas. Once the depletion zone is set, there is no free electrons and charge flowing.

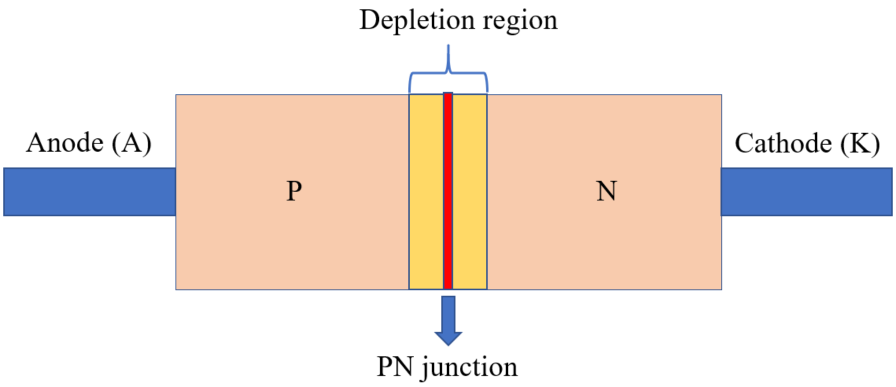

Figure 12: Basic structure of an LED p-n junction region

In order to eliminate the depletion zone and provide a charge flow between two areas, a circuit should be created with the use of a battery. To achieve this, the positive side of a circuit is connected to a P-type semiconductor while the negative side of the circuit is connected to a N-type semiconductor. This enables the flow of holes and electrons across the junction with the effect of a repelling force from the diode ends. If the circuit voltage is applied high enough, depletion zone disappears and the circuit charges flow smoothly.

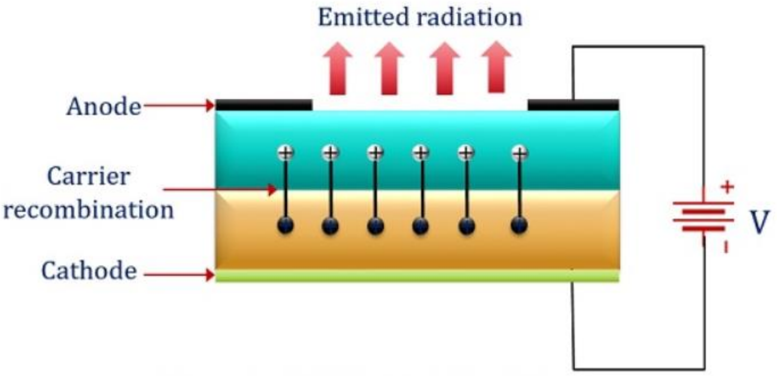

Figure 13: LED operation in forward bias condition [37]

If the different sides of the circuit are connected to the semiconductors in the opposite way, other than a repelling force, an attraction force is observed on the diode ends and no current flow occurs across the junction; thus, the depletion zone gets bigger.

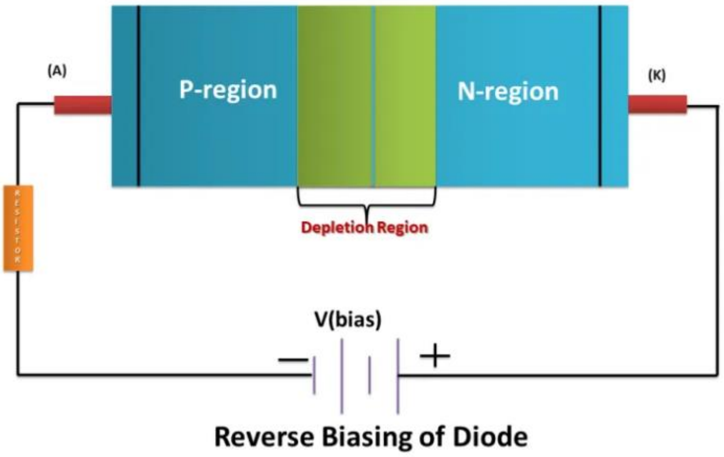

Figure 14: No current flow across the junction in reverse bias condition [38]

If the high enough voltage is applied and the current flow is generated across a diode, electrons and holes move in the opposite direction and meet in the junction. When a free electron from conduction band falls into a hole, the electron loses energy since its energy level is normally higher than the energy level of holes. Interaction between the electrons and holes results in an energy release in the form of photon, which is the most basic form of light. However, the produced photons may not be visible if the magnitude of the fall in the energy level is not large enough. The size of the fall varies with the use of different diode materials. If the semiconductor material allows a large difference in the energy levels of electrical charges on the conduction band and a lower orbital, then the photons become visible. On the other hand, if the difference in energy levels is not big enough, the photons may then be emitted in the infrared region, which is invisible to the human eye. Thus, it must be noted that the wideness of gap between the conduction band and the lower orbital determines the characteristics of the light. However, both types of visible and invisible emissions are found to be useful in many applications of LEDs.

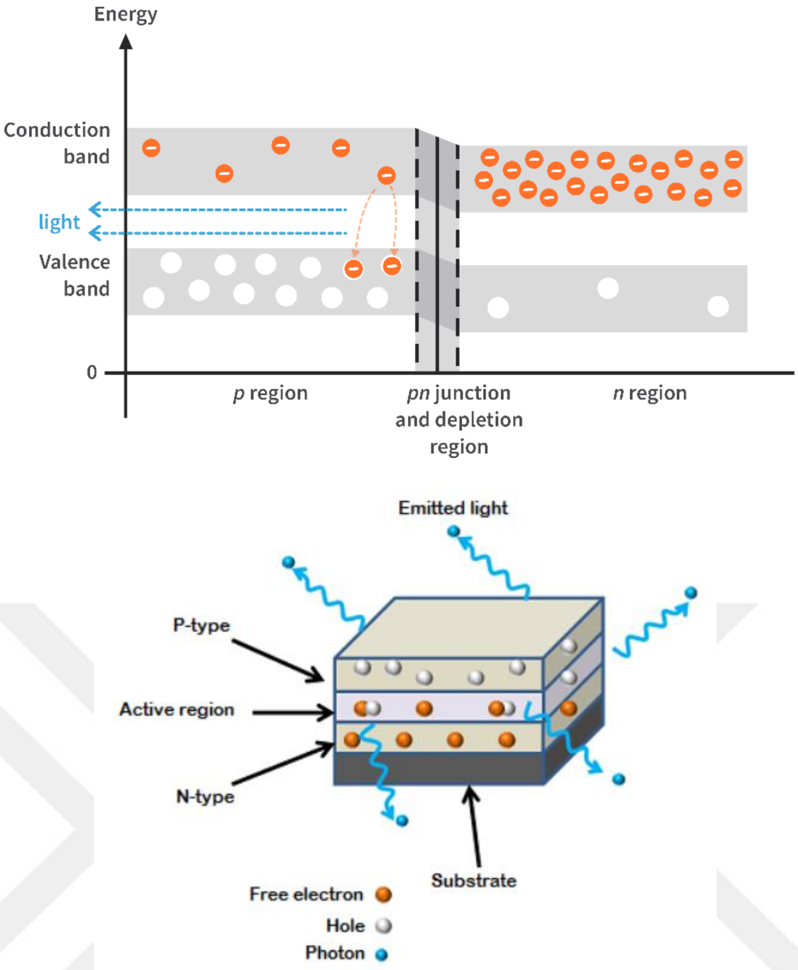

Figure 15: Change in the energy level of charge carriers and emission of light from the active region of an LED ([39], [40])

1.5 Thermal Issues in LEDs

While the combination of electrons and holes produces light emission, a significant portion of the given energy is converted into heat during the combination process. In addition, after the combination of charges in the junction region, electromagnetic rays released at different wavelengths may remain reflected in the chip itself and eventually turn into heat before leaving the chip surface. Since the optical performance and lifetime of LEDs are strongly dependent on the thermal state of LEDs, it is critical to discuss why heat generation occurs in an LED package and how it affects the performance of the LED.

1.6 Reasons of Heat Generation in an LED Package

Degradation of LED components with generated heat is one of the most critical issues that directly affect the efficiency and lifetime of LEDs. While approximately 45% of electrical energy is converted into heat directly at an LED die, this becomes around 70% after considering the additional heating inside an LED package [41]. Consequently, temperature of different components in an LED package is elevated and leads to performance loss as observed in many electronics. The components of an LED package in addition to the LED chip are seen as named in Figure 16.

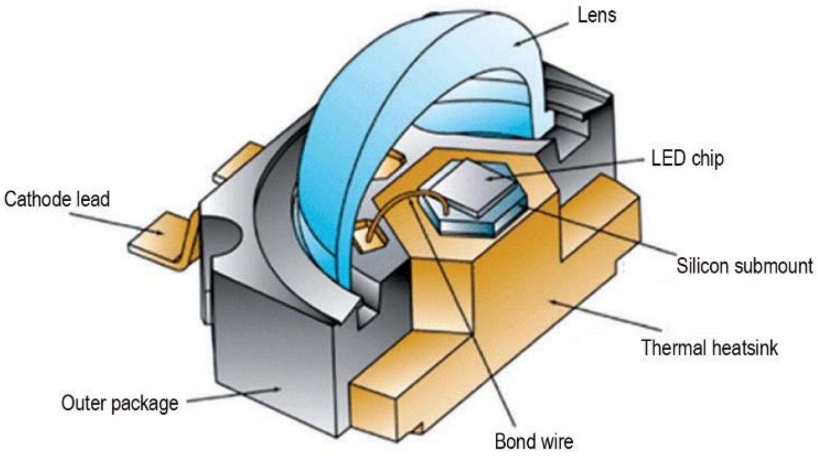

Figure 16: Basic structure of an LED package [42]

Degradation of LED components with generated heat and increased temperatures is a significant problem to be solved. In white LED packages, degradation comes into play with the yellowing of the epoxy encapsulant and there are several reasons why it occurs and even accelerates. It is mainly attributed to the excessive heat generation at the p-n junction and resulting rise in junction temperature, the amplitude of short-wavelength radiation, motion of light between phosphor and LED lens, presence of phosphor, its location and temperature [43]. Among various factors, the temperature rise of the junction region and phosphor has been shown as the primary cause of the degradation due to the heat generation that occurs in the package mainly due to non-combined radiation in the junction, losses during the shift of the wavelength of the blue light in the phosphor layer (Stokes shift) and re-absorption of back scattered light in the package [44].

1.7 Effects of Heat Generation in an LED Package

Because of the elevated temperatures in phosphor, the conversion efficiency of phosphor is significantly deteriorated, and the light output is lowered while more heat is produced. Temperature of the LED chip also rises by causing the existing defects within the p-n junction to grow bigger, impurities to diffuse faster and dislocations to migrate longer over the active region [45]. This also leads to a fall in light output. In addition, thermal stresses are exerted in the package because of the coefficient of thermal expansion (CTE) mismatch. As a result, dramatic failure of wire bonds may occur if the package design is not done so well or an adequate cooling is not provided over the operation cycles [46].

Heat generation in an LED package results in a significant rise in junction temperature (T_j) and affects the system performance. The previous studies demonstrated that as the device temperature increases from 120˚C to 150˚C at a driving current of 1.5A, the lifetime is reduced from 60,000 h to 10,000 h [47]. Figure 17 shows the temperature versus lifetime behavior of a high-power LED. As it can be seen from the figure that the lifetime of the chip is significantly reduced with the increase in junction temperature after reaching a critical value. For this reason, it is important for both industry and users to measure the temperature of the chips in both design and application phases. An increase in junction temperature also causes a linear drop in radiant power of an LED (see Figure 18) [48].

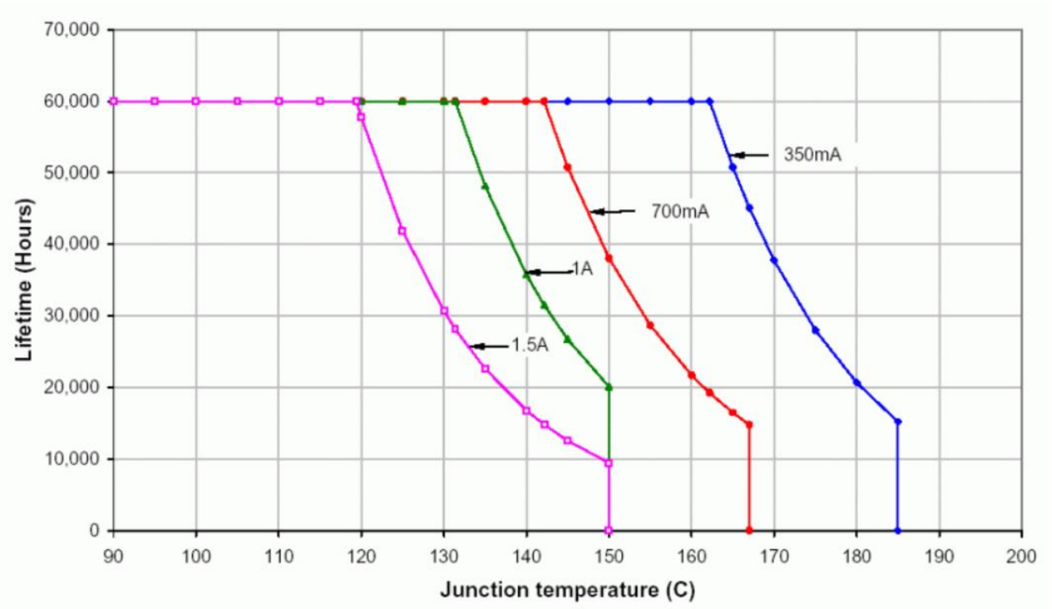

Figure 17: Relationship between junction temperature and lifetime of an LED operating at different current magnitudes [47]

In Figure 18, it is observed that the luminous flux produced decreases with the increase of the junction temperature of the LED. As the junction temperature rises, energy wastage increases, and LEDs' efficiency and performance values drop dramatically. Therefore, in order to obtain the desired luminous flux values, the thermal management of the LED systems must be performed correctly.

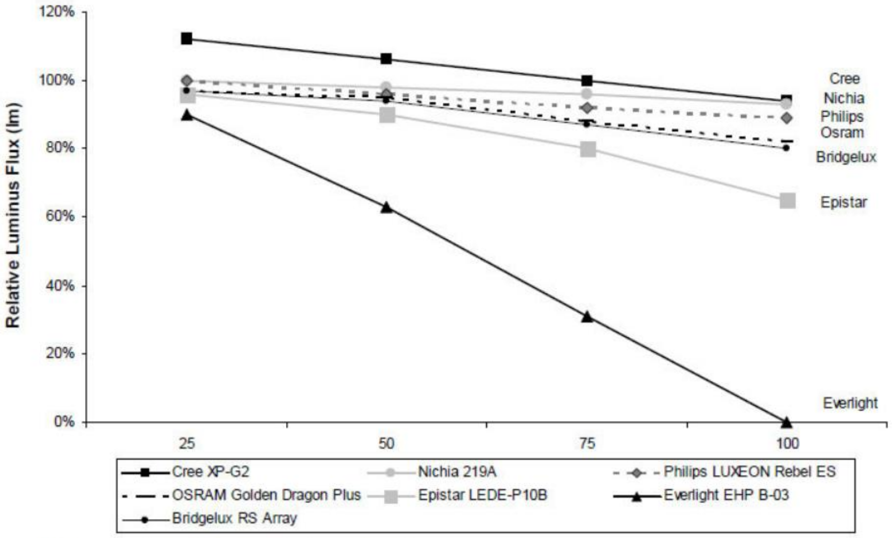

Figure 18: Variation of relative luminous flux with junction temperature [48]

In addition to electrical properties, optical parameters such as luminous flux, CCT, CRI of a lighting unit also vary directly with the junction temperature (Figure 19) [49].

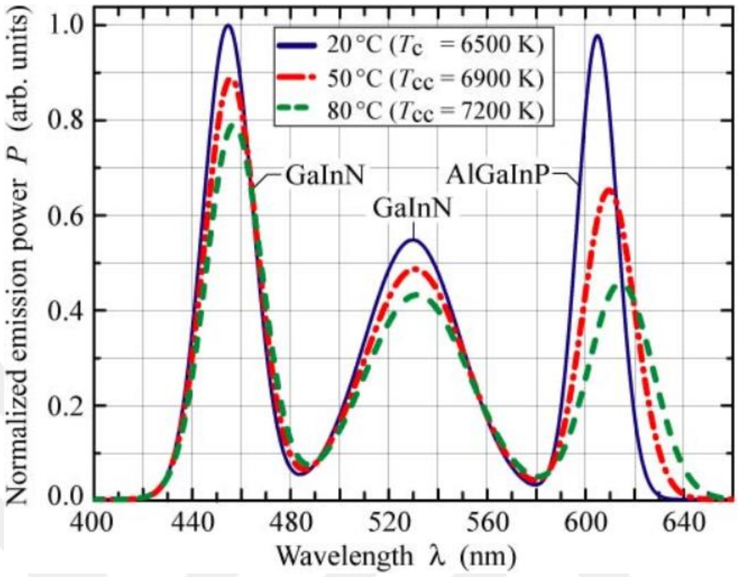

Figure 19: Change in optical traits of an LED with the increase in junction temperature [49]

Due to the significant effect of thermal issues on optical traits, previous studies put efforts for an effective thermal management of LED packages by working on the package geometry, material characteristics and innovative cooling designs. In addition, different phosphor coating techniques and dielectric optical fluids as coolants have been studied in order to improve white LED packages ([50], [51]).

In fact, in order to obtain the desired light output and efficiency, thermal resistance and temperature distribution of the LED systems are critical parameters to examine during the LED development process. On top of that, an accurate measurement of junction temperature allows the thermal resistance calculations of the package and prediction of the optical performance of the lighting system.

In many industrial applications, instead of junction temperature measurements, temperature measurements are done at the nearest soldering point on the electronic board or CFD simulations are preferred to predict and improve optical performance. One of the reasons of this practice can be explained with the difficulty that the companies face to afford highly expensive junction temperature measurement devices on the market. However, solder point measurements are not enough to characterize the optical behavior and improve the lighting systems effectively since optical performance is in fact mostly affected by junction temperature or the temperature of components on the optical path. Since there is an extra resistance between the junction and the outer region (solder), solder point measurements lead to the unreliable estimation of the performance of LEDs. For this reason, it is necessary to determine the temperature in the junction region accurately in order to facilitate the design process and offer more effective cooling solutions.

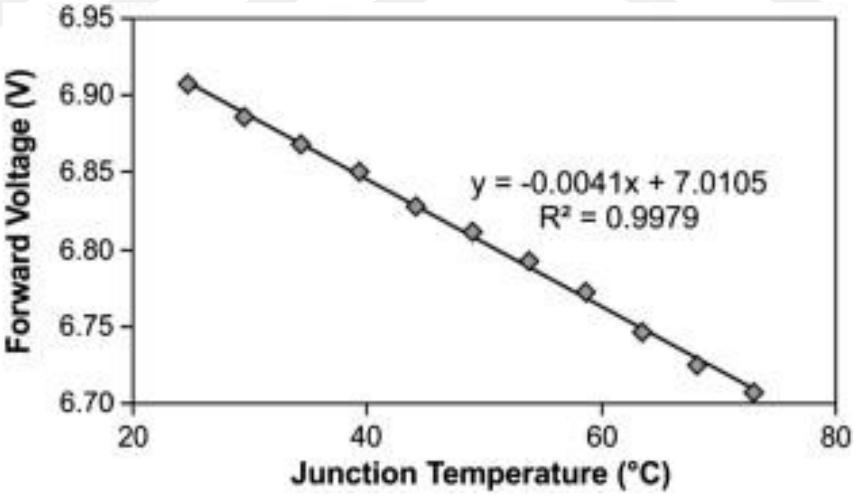

Figure 20: Relationship between junction temperature and forward voltage of an LED [52]

1.8 Junction Temperature Measurements

As discussed in previous sections, accurate identification of thermal behavior of LED packages is one of the essential tasks towards improving the design of LED systems. However, these efforts can be safely adopted to the newly developed LED packages if and only if the junction temperature of LED chips can be made accurately. Considering the measurement techniques for the junction temperature measurement, the previous studies pointed out different approaches including Raman Spectroscopy, Photothermal Reflectance Microscopy, Thermal Imaging, and Forward Voltage Change ([53]-[55]). However, Forward Voltage Change Method was suggested as the most applicable technique in terms of yielding the highest accuracy and offering the most practicability [56].

The current junction temperature measurement devices utilize transient measurement techniques and the accuracy of this technique is questioned in different studies and user application notes. At the same time, current measurement systems are too expensive for many companies to afford and use in their design process. For this reason, optothermal analysis of LEDs need to be done with alternative measurement techniques and measurement devices that provide enough accuracy for users.

In the thesis, junction temperature measurements of single and multi-LED systems are handled with two different measurement techniques. Before getting into the details, it is important to understand the difference between two LED systems and the existing issues with the current methods and measurement systems.

1.9 Single RGBW and Multi-LED Systems

In existing LED lighting systems, it is possible to achieve highly improved brightness levels with less power consumption by using monochromatic (red, green, blue or other) LEDs integrated in a multi-LED system. However, in general lighting applications, single LEDs with different color emissions can work together in a multi-LED system to produce white light. Alternatively, white light can be produced with single blue LED packages containing phosphorus particles coated on the LED chip or LED lens or suspended in the optical liquid. Each configuration brings optically and thermally different pros and cons, while directly affecting the performance, efficiency and lifetime of the device. Therefore, it is necessary to understand single and multi-LED based light engines to improve overall lighting system performance and to provide more efficient alternatives.

Red, green and blue LEDs are different due to materials in their structure, which leads to different band-gap energies and wavelengths ([57], [58]). While the band gap energy is related with the energy of photons released by an LED, the wavelength of light is a phenomenon that determines the LED color directly. Typically, green, blue and white LEDs contain InGaN (indium gallium nitride), while red, orange and yellow LEDs use AlGaInP (aluminum gallium indium phosphide) in their chips ([59],[60]).

Because of the difference in active layer materials and compositions, difference between thermal characteristics of red, green and blue LEDs are inevitable and need to be determined for the better design of lighting systems.

In a large number of previous studies, junction temperature measurement of LEDs has focused on single LEDs with transient thermal methods implemented by a commercially available system ([61]-[63]). However, junction temperature of a multi-chip LED system has not been studied widely due to lack of appropriate measurement methods for these systems. In fact, transient measurement method is found to be complicated, time consuming, costly and it is not capable of determining junction temperature of multi-LEDs connected in series [55].

Considering a significant amount of heat loss in current single LED chips (approximately 60 to 70% of electrical input power [41]), thermal issues are still significant and better cooling techniques or low power consumption technologies are required since the optical performance of LEDs is directly affected by thermal conditions ([64]-[66]). Individual LEDs in multi-chip systems are even more affected by the existence of electrical components in the circuits and thermal loads induced by other LED chips. In fact, it has been shown that thermal losses due to electrical components in a circuit could reach to the almost same levels as the radiant energy.

In junction temperature measurements of multi-chip LED systems, one dimensional heat flux assumption raises even more concerns due to the increased thermal interaction between LEDs and electrical components in the lighting unit, the generated local hot spots over the electrical board and three-dimensional heat flow in those systems.

In addition, many studies focused on determining the average junction temperature of multichip LED packages instead of measuring the individual LEDs ([67]-[68]). However, in LED systems where heat flux symmetry is changed, it is unreliable to trust on average junction temperatures of LEDs since internal quantum efficiency of LEDs may show a different behavior due to non-uniform distribution of junction temperature. Considering alternative cooling systems developed for future lighting systems and the inclusion of IoT sensors in these units, accurate measurement of junction temperature of LED chips in this system will be critical to ensure that the lighting unit is designed to operate in its optimum condition. In addition to those raised concerns about heat flux assumption in measurements, the current measurement systems are not applicable to measure junction temperature of LEDs serially connected in multi-LED systems.

In line with the described issues in high power LEDs, this thesis aims:

In Chapter II:

- To investigate the reliable ways of junction temperature measurements of high-power LEDs and compare different junction temperature measurement methods.
- To analyze the impact of an optical path in high power single red LEDs with thorough understanding of optothermal characteristics in the LED package.
- To characterize the differences in forward voltage drop and optothermal behaviors of high power RGB LEDs as a result of different materials utilized in the active layer.
- To propose a novel junction temperature measurement technique for Multi-LED systems and investigate the impact of electronics and local hot spots on optical performance.

In Chapter III:

- To figure out the problems in current junction temperature measurement techniques and available junction temperature measurement devices.
- To propose a highly functional junction temperature measurement system and introduce the system advantages.
- To define the measurement approach used in the proposed junction temperature measurement system (EVAtherm).
- To describe the design, analysis and manufacturing processes of EVAtherm in three versions.
- To analyze junction temperature measurements conducted in EVAtherm.

CHAPTER II

EXPERIMENTAL STUDY

2.1 Junction Temperature Measurement Techniques

Junction temperature is a critical parameter since it directly affects the performance of solid-state devices such as LEDs [69]. Given the thermal problems in LED systems, the cooling techniques for these systems are more effectively developed when the temperature of the junction region is accurately determined. Although this region cannot be accessed directly, there are a number of methods for the junction temperature measurements. One of those, forward voltage change method, was selected as the main method and utilized during the different phases of the study. Thermal imaging method and computational tools were also utilized in order to assure the results obtained from the forward voltage change method are reliable. In fact, it was aimed to investigate the junction temperature measurement capability of a high-resolution IR camera and to develop a robust numerical model that is validated with experimental results.

2.1.1 Forward Voltage Change Method (FVCM)

Forward voltage change method has been reported as the most reliable and practical way of measuring junction temperature and it includes calibration and test phases ([70]-[54]).

During the calibration phase, LEDs are inserted in a temperature-controlled chamber where the temperature of the chamber is adjusted with a maximum variation of ±0.2˚C. Temperature inside the oven is set to different temperatures respectively and LEDs are pulsed with a sourcemeter device when the thermal equilibrium is achieved at each temperature. A pulse current of 1 milliampere (mA) is applied for 1 millisecond (ms) duration and forward voltage readings are made with the sourcemeter system. Application of the pulse current for 1 ms ensures that a negligible amount of heat generation occurs over the junction region. Thus, it can be assumed that the junction temperature is the same as the oven temperature under thermal equilibrium conditions. During the application of pulse currents, the repeated forward voltage readings of the LED chip are recorded and averaged to use for constructing the final calibration equation.

In the test phase of the FVCM, the LED chip is operated with the sourcemeter system at its nominal current. After the LED chip reaches electrically (±0.1 mV) and thermally steady state conditions (±0.2°C), the nominal current is dropped to the pulse current (1 mA) for 1 ms [71]. Steady state condition is decided based on the variation in forward voltage readings of the repeated pulse current applications and the change in the LED board temperature. The corresponding forward voltage after applying the pulse current is measured at the test condition and plugged into the calibration equation derived in the calibration phase. In this way, junction temperature of an LED chip is determined at a specified operating current.

An integrating sphere system is also utilized to measure radiant flux at steady state (±0.2°C) [72] and the test phase of the junction temperature measurements is conducted in this system with simultaneous optical measurements. Different calibrations are made for the optical test in the integrating sphere and they include reference lamp calibration, auxiliary reference calibration and auxiliary test calibration. A reference lamp whose optical characteristics are already defined under certain limits and an auxiliary lamp are utilized to calibrate the integrating sphere and spectrometer response. As a result, the absorption correction of the LED product is made. Uncertainty at spectral flux measurements is determined as 1.3% [73].

As seen in Figure 21, optical measurements are made spectrally in the integrating sphere system, and the spectral distribution of a high-power red LED is obtained with the radiant flux measurements. In order to conduct optical performance tests, LEDs are located at the center of the integrating sphere and hemispheres are closed to provide light leak free and temperature controllable environment for the measurements of the LED. After the system and test calibrations are made, the LED is run at a driving current with the use of a sourcemeter system until steady state is reached. The emitted light from LED is reflected at the inner surface of the sphere system, which is smooth and coated with a highly reflective material [72]. Finally, the emitted light is collected at the attached detector on the sphere wall and meaningful optical data is derived for the operation of the LED using a spectrophotometer unit. The measurement results are monitored and analyzed in the computer software.

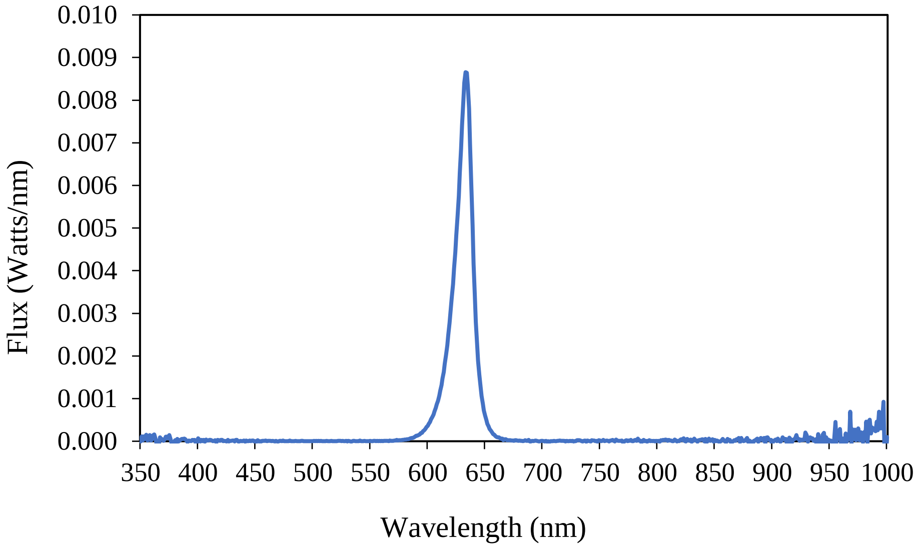

Figure 21: Spectral distribution of radiant flux

when the red LED is operated at 200 mA

The experimental methods utilized in different phases of the studies are seen in Figure 22. A temperature controllable oven, an integrating sphere, a sourcemeter system, an (IR) thermal camera, a DC power supply, a data acquisition system (with T-type thermocouple connections) and a personal computer are utilized in the experimental setup.

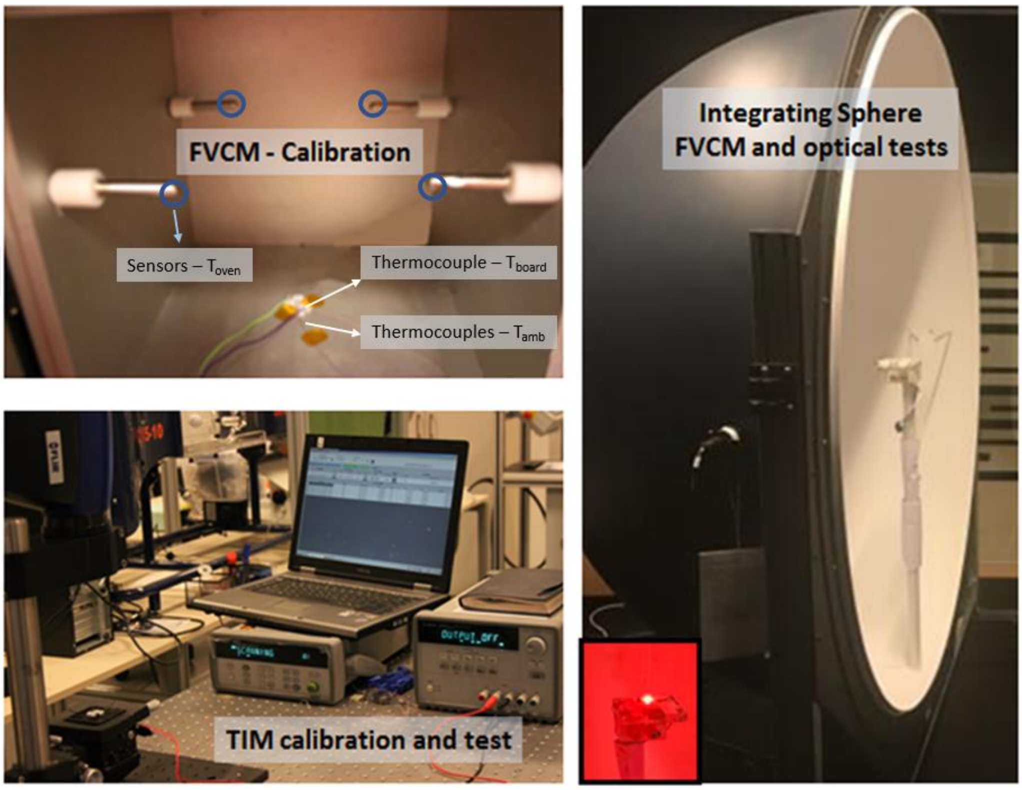

Figure 22: Experimental setup prepared for conducting Forward Voltage Change (FVCM), thermal imaging (TIM) and optical measurements

Temperature measurements are conducted to determine the steady state and thermal equilibrium conditions in calibration and test phases. In all experiments, thermal condition of an LED is monitored with T-type thermocouples attached on the LED board (PCB) and kept in ambient nearby the LED as seen in Figure 23. In addition, in the calibration phase of the FVCM approach, the oven temperature is monitored with temperature sensors embedded at the half-height of the chamber walls.

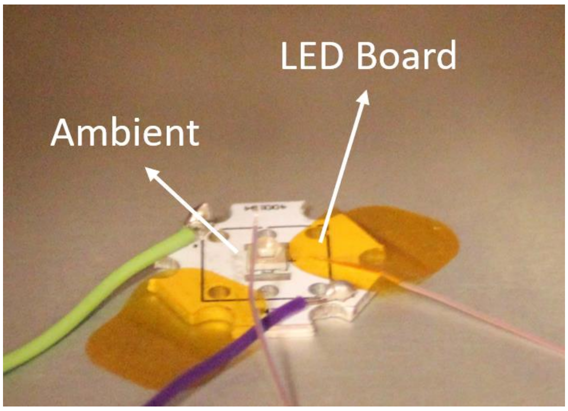

Figure 23: Attachment of thermocouples on the LED for temperature monitoring

2.1.2 Thermal Imaging Method (TIM)

Infrared thermal imaging method (TIM) is based on non-contact measurements by using a calibrated IR camera in order to obtain the temperature distribution over an object. To improve the reliability of the results, a mid-wave infrared thermal camera (FLIR SC5000) with a resolution of 640x512 pixels and an accuracy of ±1˚C was used to verify the junction temperature measurements obtained by forward voltage change method.

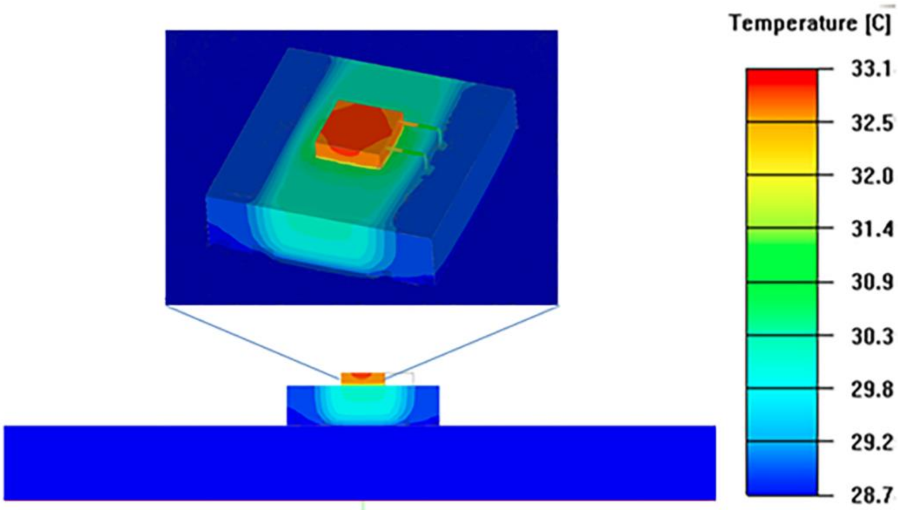

Figure 24: Temperature distribution over the LED system

Although the camera provides the temperature distribution of the LED chip surface instead of the device junction, the temperature of the LED chip surface was expected to be very close to the junction temperature and vary less than 1˚C. A numerical model of a red LED chip operating at 200 mA current was simulated to show the temperature distribution over the region and it was understood that the direct measurement of the surface temperature of an LED chip enables the approximated junction temperature to be obtained in a practical way (see Figure 24).

For the accuracy of the results, it is important to know how some parameters affect the IR measurements, such as emissivity of the surface, the viewing angle of the camera, surface reflections, transmission characteristics and atmospheric attenuation [74]. In this study, the emissivity of the target surface was determined with an experimental calibration performed with T-type thermocouples. The viewing angle of the camera was adjusted by using a readily available experimental apparatus as seen in Figure 25.

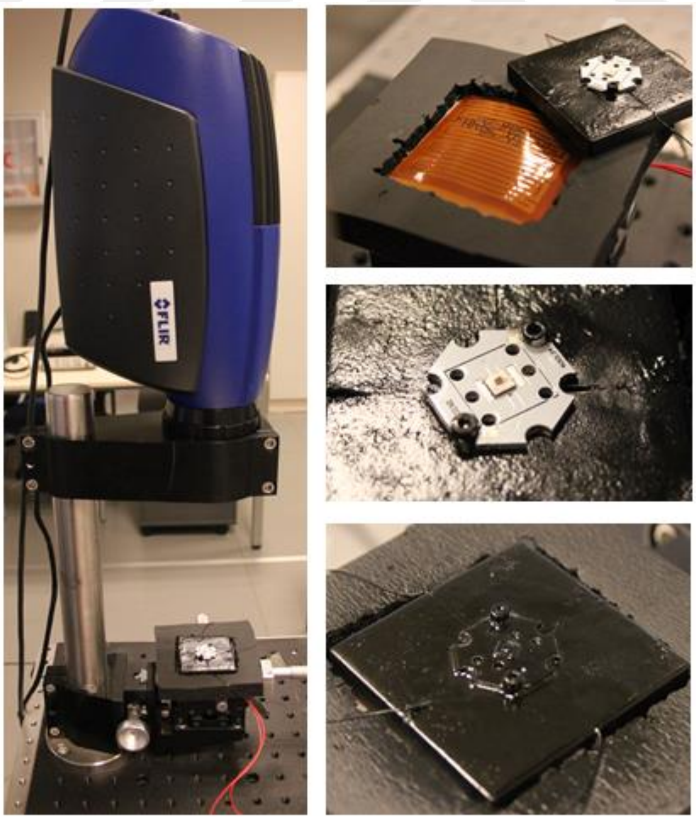

Figure 25: Experimental study for IR thermal measurements

Special attention was given to align the IR camera parallel to the target region in order to prevent some of the emitted energy from escaping at a certain angle. Thus, the thermal energy emitted from the LED chip is directly perceived by the sensors of the camera without any loss due to the viewing angle and the measurement error is significantly reduced. Surface reflections were eliminated and there was no intermediary substance used in between the target surface and IR camera that affected the transmission. Finally, auto-correction for atmospheric attenuation was applied by the IR camera software.

An experimental validation study was conducted to increase the reliability of the IR camera measurements by verifying the results with a T type thermocouple over the same chip surface. A relationship between two measurements was created for unpainted and painted LED chip surfaces after the LED dome was removed. First, the temperature results of four thermocouples were compared among themselves and the results differed by approximately 0.2°C. Then, one of those thermocouples was chosen and utilized in further experiments.

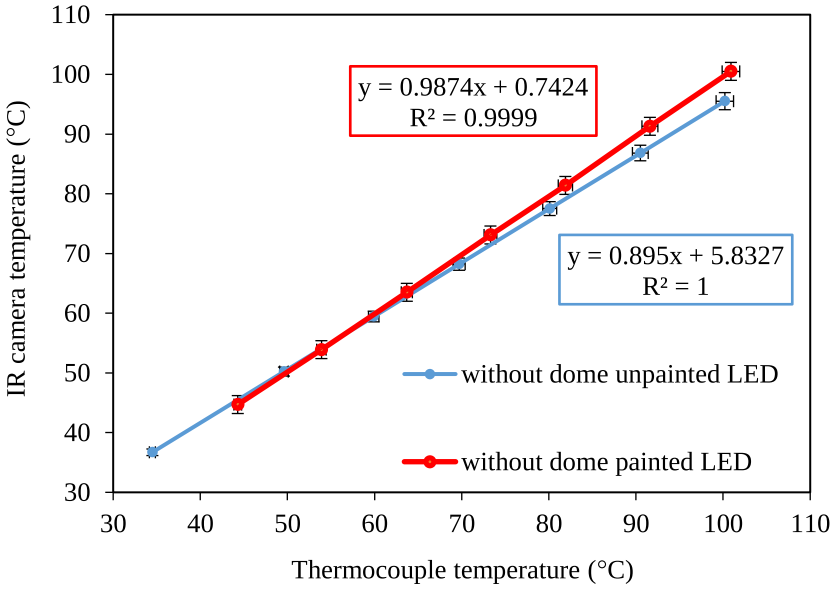

Figure 26: Emissivity calibration for IR temperature measurements

In order to derive the correlation between thermocouple and IR readings over the same surface, the tip of the thermocouple was identified in the IR camera image and a very small circle was selected. Then, the average temperature was obtained in the circle as the corresponding temperature measured by the IR camera. The measurements were conducted for seven different temperatures, which cover a wide range of values between 35 and 105˚C. Emissivity of the target surfaces was found by matching thermocouple and IR camera results.

The measurement results and the equations derived for two different surfaces are given in Figure 26 for the unpainted LED without dome and the painted LED without dome configurations. The LED without dome was painted with Rust-Oleum High Heat 2000 Degree black spray paint and no light output or leakage was allowed from the chip surface. An emissivity calibration study was performed as suggested in a previous research ([75],[76]). As a result, emissivity of the surfaces was found to be 0.84 for the unpainted LED, and 0.98 for the painted LED without dome.

Simultaneous junction temperature measurements were conducted for the forward voltage change and thermal imaging methods. Since board temperatures were measured via T-type thermocouples during the calibration phase of forward voltage change method, junction temperatures derived using these calibration equations in a test phase can be treated as temperatures measured by thermocouples. In order to convert junction temperature results derived in forward voltage change method into the corresponding chip temperature of the IR measurement, the validation equations derived in Figure 26 were utilized. It was observed that junction temperature results obtained using the validation equations (considering 57.7˚C for the unpainted LED without dome driven at 500 mA) are in good agreement with the direct IR measurements in the test phase as seen in Figure 27.

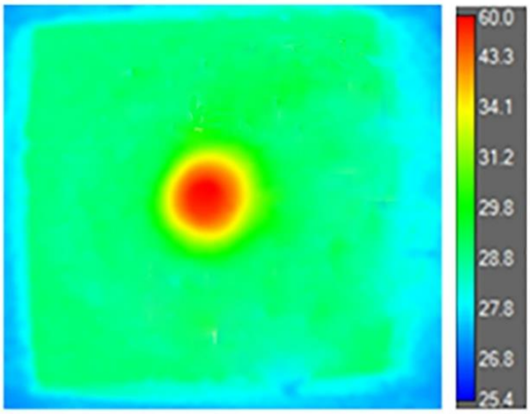

Figure 27: Temperature distribution of the unpainted LED without dome running at 500 mA operating current

2.1.3 Computational Fluid Dynamics (CFD) Models

Computational approaches are very helpful in engineering design to provide pre or post design conditions. It is very practical to develop numerical models and provide further insights without conducting expensive and time-consuming experimental studies. A computational model was developed by using ANSYS Icepak [77] in order to validate experimental results and establish a numerical approach for the junction temperature measurements of LEDs under various conditions.

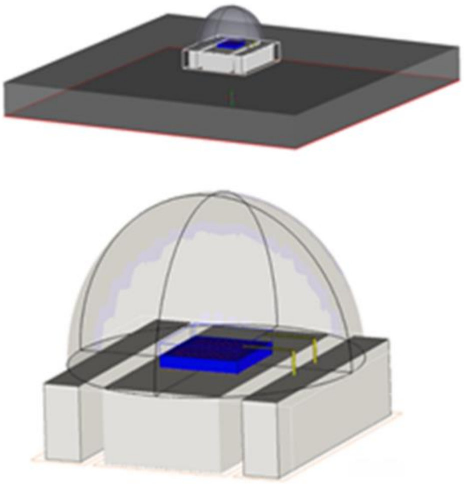

Figure 28: Modeling the tested LED system (top) and LED chip (bottom)

A numerical model was created by referring to the LED structure as it is seen in Figure 28. Boundary and operating conditions were set in ANSYS mimicking real conditions and material properties. The main components in the LED model are LED chip, LED dome, active layer (heat source), wire bonding, leadframe, mold base, die attach and PCB. The LED dome in the package has a hollow elliptic shape and it is connected to the substrate other than the gold wire and the LED chip. Material properties and geometric details for these components are given in Table 1.

Table 1: Thermal and physical properties of LED components in the numerical model

Components	Properties
LED chip	Si (k = 180 W/m-K) 1x0.15x1 mm^3
LED dome	Epoxy-glass fiber (k = 0.17 W/m-K)
Heat source	Heat source 0.75 x 0.75 mm^2
Wire bonding	Wire bonding - Au (k = 313 W/m-K) 0.65 x 0.07 mm^2
Inner lead	Al Die Cast90 (k = 105 W/m-K) 1.5 x 0.92 x 3.2 mm^3
Mold base	Mold material (k = 0.8 W/m-K) 3.5 x 0.92 x 3.5 mm^3
Die attach	Die attach material (k = 2.5 W/m-K) 1 x 1 mm^2
PCB	Al Die Cast90 (k = 105 W/m-K) 16.5 x 1.7 x 16.5 mm^2

The final number of elements was selected as 969,527 in order to reduce the computational time and reach a converged solution. The meshed model is seen in Figure 29.

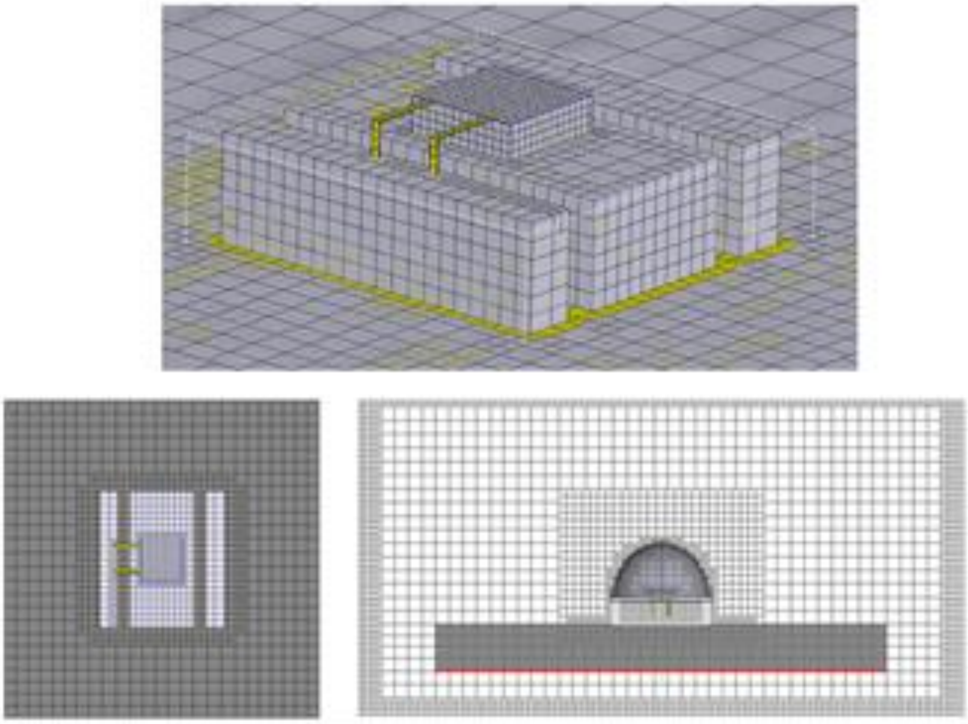

Figure 29: Mesh distribution on the LED system; 3D view (top), top view (bottom left) and front view (bottom right)

Ambient temperatures (T_a), input (E_{in}) and radiant powers (E_r), generated heat (Q) and board temperatures (T_b) were directly taken from experimental data for three different configurations and operation currents of 200, 350 and 500 mA in the numerical model (see Table 2). The LED configurations are represented by the numbers in the table: the LED with dome (1), the unpainted LED without dome (2) and the painted LED without dome (3).

Table 2: Boundary and operating conditions during the experiments

Current (mA)	Configuration	Ambient temp. (T_a,˚C)	Input power (E_{in}, W)	Radiant power (E_r, W)	Generated heat (Q, W)	Board temp. (T_b,˚C)
200	1	23.3	0.4879	0.1892	0.2988	28.8
	2	23.1	0.3947	0.1097	0.2851	29.6
	3	22.5	0.3928	-	0.3928	33.2
350	1	23.3	1.0128	0.3339	0.6789	34.4
	2	23.1	0.7253	0.1949	0.5304	36.1
	3	22.5	0.7201	-	0.7201	42.4
500	1	23.3	1.6592	0.4595	1.1997	40.3
	2	23.3	1.0790	0.2758	0.8032	43.5
	3	22.5	1.0708	-	1.0708	51.6

2.2 Impact of the Optical Path in a Single Red LED

2.2.1 LED Configurations

LEDs utilized in this study are CREE XLamp XP-E2 high power red and blue LEDs. Three different LED configurations were studied in order to predict thermal, optical and electrical characteristics of the LED. These include an LED with a dome, an unpainted LED without a dome (bare chip), and a painted LED without a dome (see Figure 30). The comparisons of three configurations give significant understanding on the effects of the LED dome and heat generation on thermal, optical and electrical behaviors of LEDs.

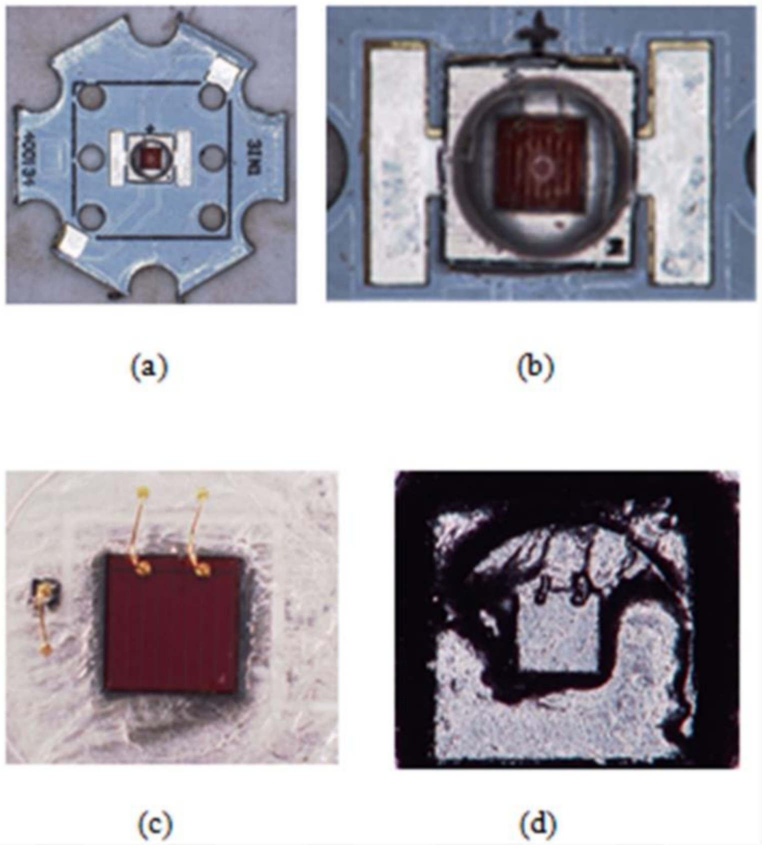

Figure 30: CREE XLamp XP-E2 (a) high power red LED, (b) unpainted LED with dome, (c) unpainted LED without dome, (d) black painted LED without dome

The dome was removed safely based on a technique suggested by Ozluk et al. [78]. This technique was applied using a WXR3 hot gun at the optimum distance required to soften the dome below melting temperature. The dome was then slightly moved by using a tweezer, and it was removed after air penetrated into the dome. The technique has shown a successful yield for ten samples without any wire bonding breakage, failure in operation, and residual particles on top of the junction area. A safety check was made with an optical microscope to examine the structure of the LED package before and after the dome removal. Safe removal of the dome was ensured with the clear removal of the dome (see Figure 31) and successful operation of the LED.

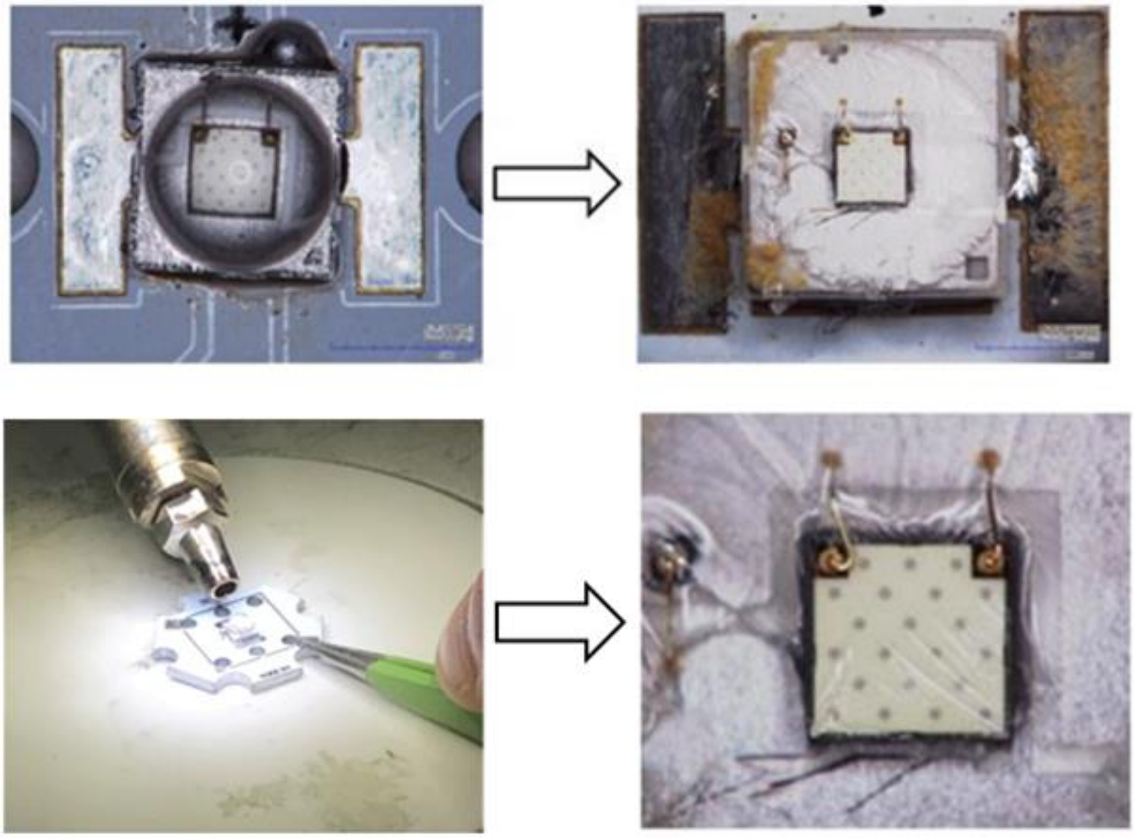

Figure 31: Safe removal of an LED dome with a technique suggested by Ozluk et al. [78]

In order to provide the same boundary conditions during the experiments, the LED board temperature was set to 40˚C during the test phase of the forward voltage change method, and the junction temperatures were obtained accordingly.

2.2.2 Optothermal Characteristics

The impact of an LED dome on the thermal, optical and electrical characteristics of the LED package was studied in order to understand the role of an LED dome in the package and compare junction temperature methods more accurately. First, the change in the junction temperature over the ambient temperature with respect to the generated heat was analyzed in Figure 32.

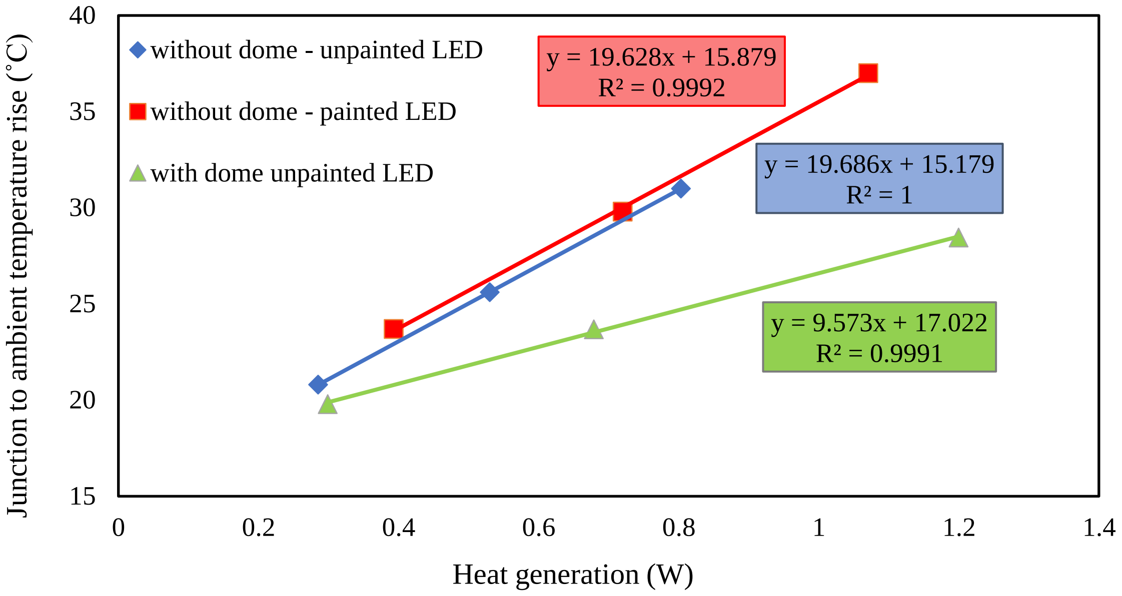

Figure 32: Relationship between temperature difference and heat generation at the active layer

As expected, the slopes for the unpainted and painted LED without dome in Figure 32 are found to be very close to each other since the LED package has the same components in both cases. On the other hand, the slope for the LED with dome is smaller since thermal resistance of the LED package is lower when another heat flow path with the LED dome is provided. It is also observed that the line for the LED without dome is a little bit shifted after painting the LED chip since the radiant energy is converted into heat and the highest junction temperatures are measured in this case. However, the LED with dome has a lower temperature rise in the junction for the same heat generation.

The amount of heat generation was determined for the unpainted LED with and without dome by subtracting the radiant power from the electrical power. On the other hand, the heat generation for the painted LED without dome was determined by taking the electrical power directly since it is all converted into heat due to the absorbing nature of the black paint over the chip. At the lower operating currents, the amounts of generated heat were close to each other in the configurations of LEDs with and without dome. However, as the operating current is increased, junction temperature of the LED with dome increased less although it produced more heat than the LED without dome. In fact, the only difference between two configurations is the presence of the LED dome. Therefore, when two configurations are compared, less increase in the junction temperature of the LED with dome can be explained by the presence of the LED dome, which is the extra conductive path in the LED with dome configuration. As the higher forward voltage is measured at the lower junction temperature, the LED with dome is expected to have a higher voltage drop, therefore a higher electrical input power at a certain current. Since the amount of heat produced in the junction region is proportional to the electrical input power, more heat generation is also expected in the LED with dome. All these findings are supported by the experimental results given in Figure 32 and Figure 33.

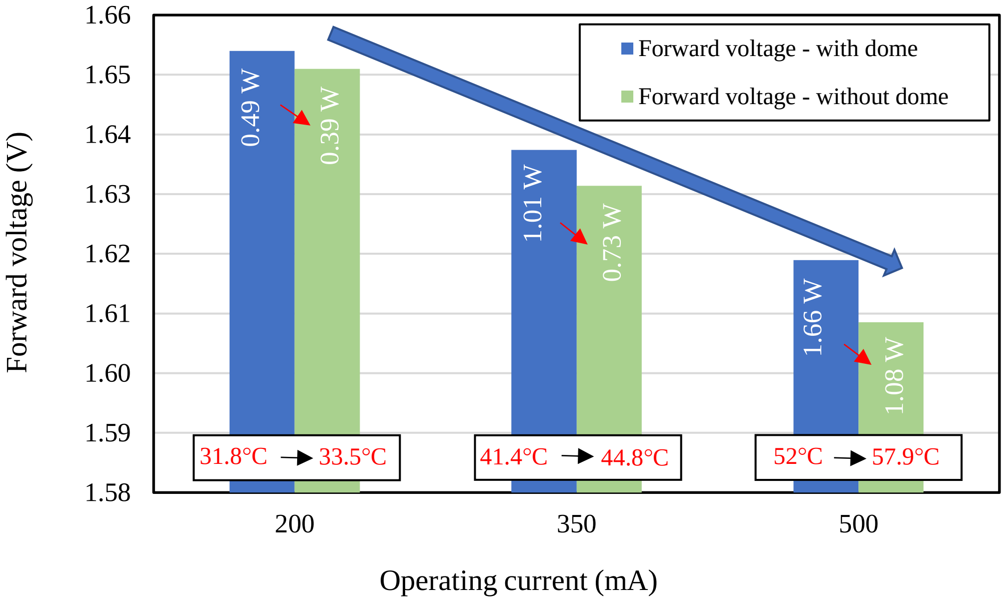

Figure 33: The impact of junction temperature on forward voltage of a red LED after removing the LED dome

Figure 33 demonstrates the forward voltage drop with the rise in junction temperature after the LED dome was removed at three operating currents. Electrical powers are also indicated for each driving current and LED configuration. As it was expected at all driving currents, higher forward voltage readings were recorded for the LED with dome since the lower junction temperatures were obtained. At higher driving currents, the removal of the dome led to a more increase in the forward voltage drop as a result of a large shift in junction temperature. In addition, electrical power values followed a similar trend with the growing decrease in forward voltage values when with-dome and without-dome cases were compared at each current magnitude. After the dome was removed, electrical power was lowered by 19.1%, 28.4% and 35% respectively at 200, 350 and 500 mA. In general, it was observed that the junction temperature increases with the removal of the dome, however; the forward voltage and electrical power are inversely affected by this trend.

The junction temperatures of unpainted and painted configurations of LED without dome were also compared with respect to the driving currents as seen in Figure 34. Thus, the rise in junction temperature was observed when the total radiant power was converted to heat and absorbed by the surface paint. As a result, the comparison of junction temperatures in three different configurations given in Figure 33 and Figure 34 provided an insight into the impact of the LED dome on junction temperature and how the generated heat affects junction temperature of a red LED.

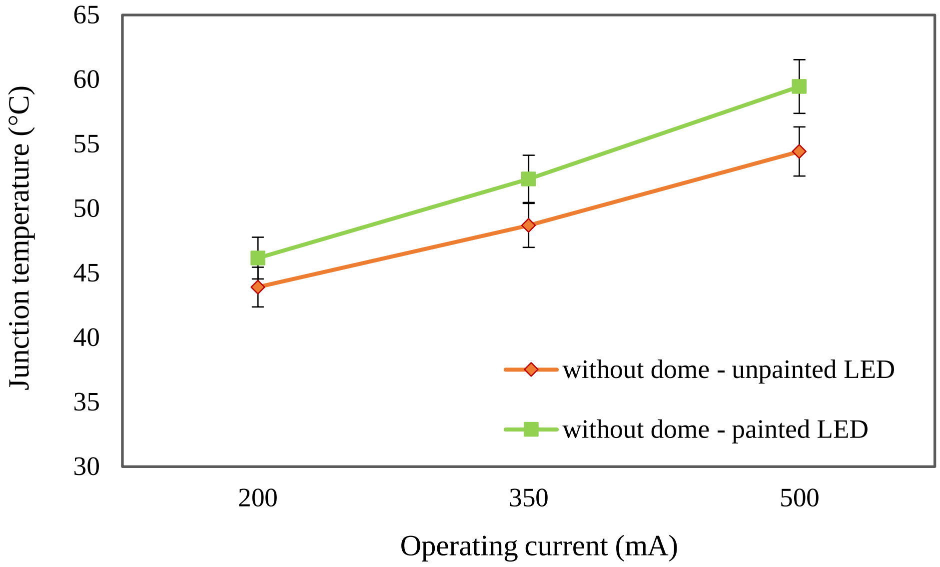

Figure 34: Junction temperatures with respect to three operating currents for the unpainted/painted LED without dome

The painted LED without dome operating at 500 mA had the highest junction temperature while the least junction temperature was measured when the unpainted LED with dome was driven at 200 mA. Moreover, the difference of junction temperatures between various LED configurations was raised as the application current was elevated. As a result, from 200 to 500 mA, the change in junction temperature is 20.1%, 23.9% and 28.8% respectively for the LED with dome, unpainted and painted LEDs without dome. Junction temperature increased by 0.8 to 2.7˚C depending on the current magnitude (200 mA to 500 mA). These results demonstrate that an LED dome might play a critical role both in magnitude and change of junction temperature as the LED is driven at higher currents. Furthermore, the conversion of optical power to generated heat may critically affect the thermal performance of a red LED due to a considerable increase in junction temperature. After removing the dome and painting the LED, a larger shift in junction temperature was observed by 2.2 to 5˚C depending on the application current (200 mA to 500 mA).

In addition to junction temperature behavior, the alterations in radiant power and conversion efficiency were seen after the LED dome was removed at three driving currents (200, 350 and 500 mA) as shown in Figure 35 and Figure 36. Thus, the impact of the dome on optothermal characteristics of the red LED was examined and the performance of the red LEDs was further characterized. The drop in radiant power and conversion efficiency was noticed at each operating current when the dome was removed.

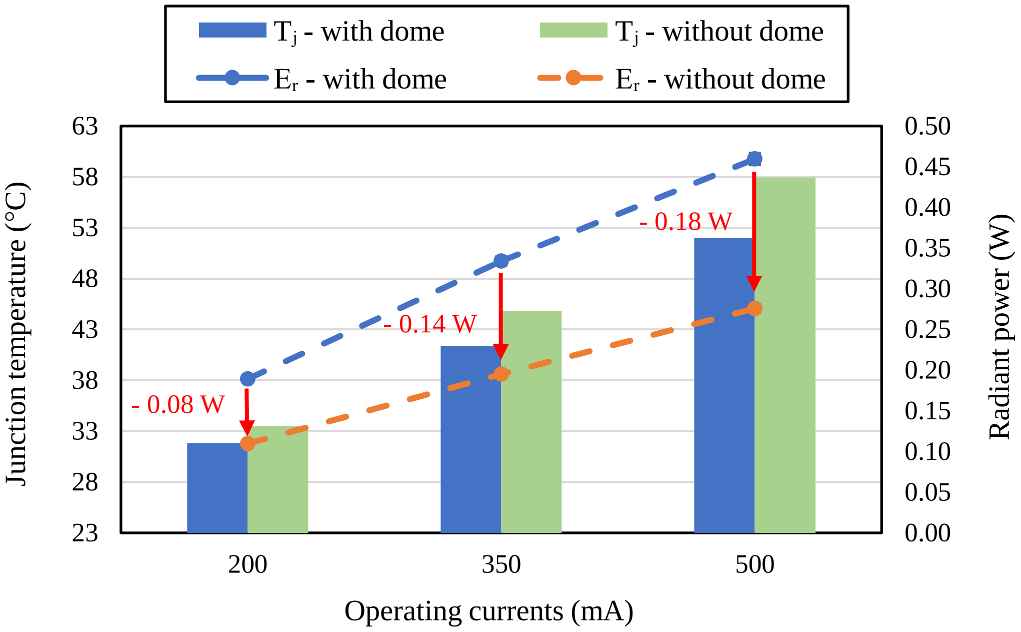

Figure 35: Change in radiant power and junction temperature of a red LED after removing the LED dome

After the removal of the LED dome, radiant powers at each current were observed to drop by 0.08 W (42%), 0.14 W (42%) and 0.18 W (40%) respectively with the rise in junction temperatures. Considering the significant impact of junction temperature on light output and the effect of an LED lens on light extraction, the LED without dome emitted a less amount of light at each application current.

2.2.3 Conversion Efficiency

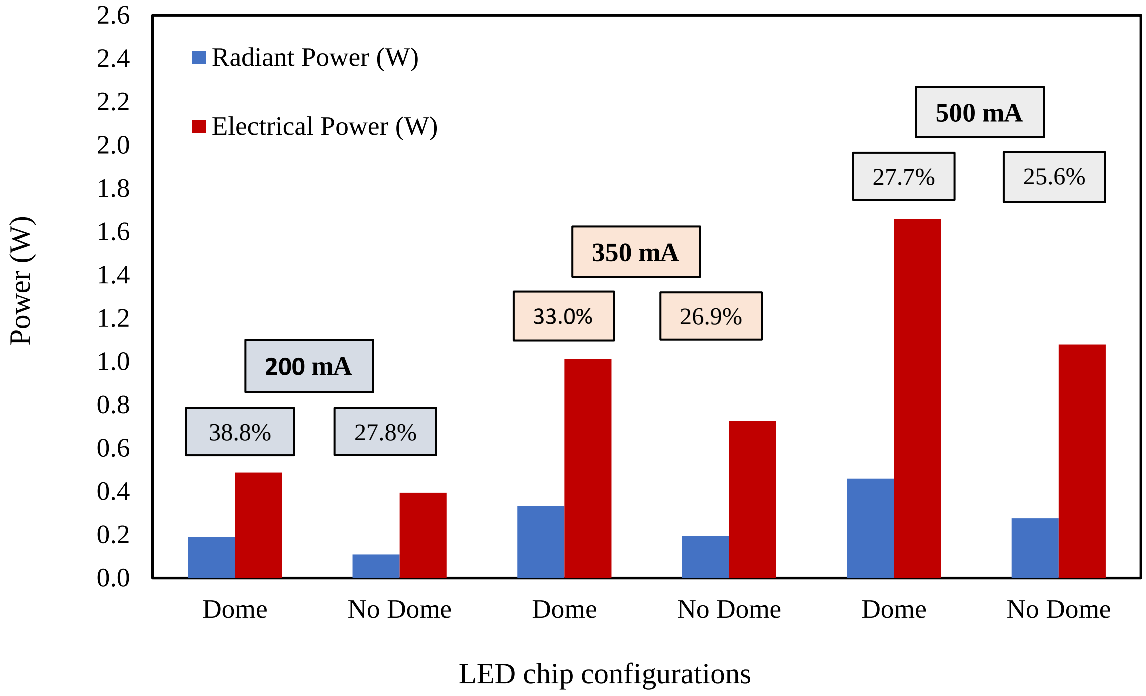

Figure 36: Change in the chip conversion efficiency with respect to the applied current and LED configuration

The conversion efficiency of red LEDs with dome was found to be higher at all three operating currents (see Figure 36) although some optical losses and reduced efficiency were expected compared to the LED without dome. The underlying reason behind a higher efficiency when the dome remains attached is related to the thermal and optical effects of an LED dome on the chip. The existence of a dome provides another heat flow path by changing the heat flux symmetry [79]. Thus, while the most heat is dissipated through the "lower path" including the chip, lead frame and substrate, a portion of the generated heat is also transferred to the "upper path" through dome [41]. However, when the LED package does not have a dome, heat flow path is limited to only the lower path; therefore, the junction area is exposed to larger heat and the junction temperature rises up. This also causes a drop in radiant energy since the junction temperature is inversely proportional to radiant energy [80]. It is noteworthy that as the operating current increases, the positive effect of a dome on conversion efficiency is less or optical losses become more dominant. While there was a 11% difference in conversion efficiency between the LED with and without dome operating at 200 mA, it decreased to 2.1% when the operation current was elevated to 500 mA.

In addition to the effect of junction temperature on optical power, the positive effect of an LED dome on light extraction should also be noticed. Due to the refractive index mismatch between the LED chip and other components of the package, a portion of the generated light is lost as heat as a result of total internal reflections in the chip. On the other hand, if the refractive index contrast is reduced in the package with the use of other components, total internal reflections can be lowered, and more light can be extracted since the critical angle of total internal reflection is enlarged [81]. This would also result in a drop in heat losses.

The use of an LED dome does not only provide a mechanical protection to the chip but also reduces the refractive index contrast so that light extraction is enhanced. On the other hand, the removal of the dome leads to additional heat losses and the rise in junction temperature. Thus, radiant power of an LED with dome is expected to be higher.

Junction temperature, radiant power and conversion efficiency of red LEDs were also compared with the same type of high-power blue LEDs at three different driving currents (200, 350 and 500 mA) (see Figure 37). This analysis was useful to make a better interpretation of the optothermal behavior of red LEDs as the blue LEDs can be considered as a reference and commonly studied type of LEDs.

2.2.4 Comparison with InGaN LEDs

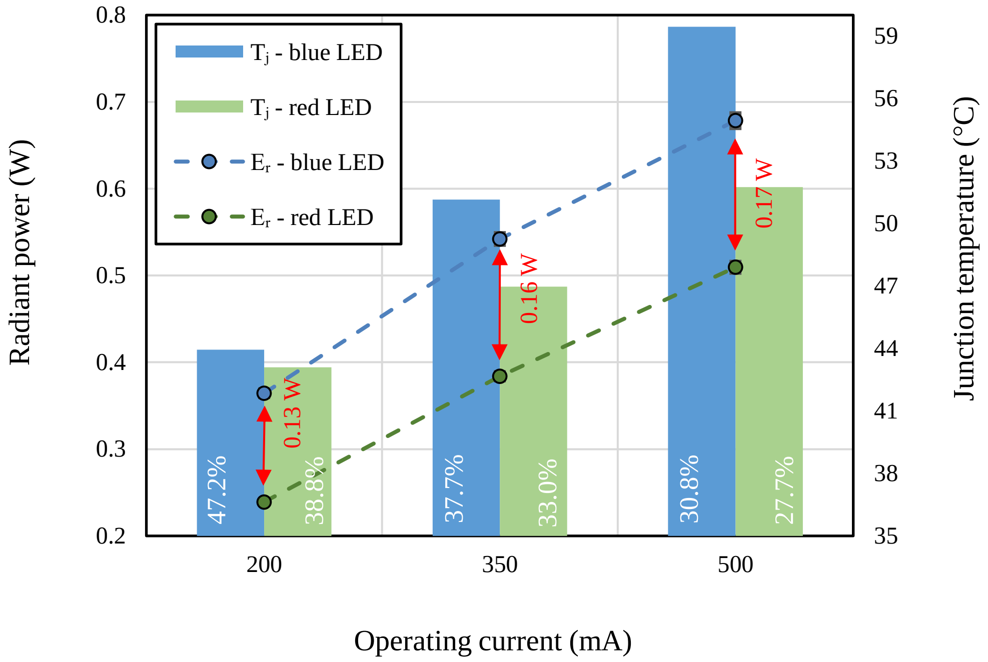

Figure 37: Comparison of junction temperature, radiant power and conversion efficiency of red and blue LEDs with respect to applied operation currents

The results show that the blue LED is operated at higher junction temperatures and the difference between the temperatures of blue and red LEDs is getting larger as the operating current is increased. Especially, at higher operating currents, the junction region of blue LEDs becomes much hotter (around 7°C at 500 mA driving current) compared to the red LEDs. The impact of the junction temperature on radiant power and conversion efficiency of LEDs has also been compared to reveal thermal and optical mechanisms in two types of LEDs. At all operating currents, the red LED has produced lower radiant power although it was operated at lower junction temperatures. On the other hand, the blue LED has yielded 8.8%, 4.7% and 3.1% higher conversion efficiency at 200, 350 and 500 mA respectively. Thus, it has been understood that although red LEDs can thermally be a better solution; they offer lower light efficiency than blue LEDs.

Since the same model red and blue LEDs were used, the difference is mainly attributed to the chip material in the LED package and red LEDs operate at much lower forward voltages relative to the blue LEDs when the same magnitude of current is applied (typically around 1.6 V for red LEDs and 2.4 V for blue LEDs). The effects of the material properties on the junction temperature and generated heat over the junction region can be examined in a future study.

An uncertainty analysis was conducted for junction temperature measurements based on the forward voltage change method. Uncertainties contributed from the measurement devices and experiments were taken into consideration. Methodology and details of the uncertainty calculations are given in Appendix A.

2.3 Optothermal Characterization of Single RGB LEDs

Red, green and blue LEDs are different due to the materials used in in their structure, which leads to different band-gap energies and wavelengths ([57], [58]). While the band gap energy is related with the energy of photons released by an LED, the wavelength of light is a phenomenon that determines the LED color directly. Typically, green, blue and white LEDs contain InGaN (indium gallium nitride), while red, orange and yellow LEDs use AlGaInP (aluminum gallium indium phosphide) ([59], [60]) in their chips. Because of the difference in active layer materials and compositions, difference between thermal characteristics of red, green and blue LEDs are inevitable and need to be determined.

In this study, an experimental and computational study has been performed to understand the impact of the chip temperature over forward voltage and radiant power of red, green and blue LEDs.

2.3.1 Development of Calibration Curve for Single RGB LEDs

In order to measure junction temperature of single RGB LEDs, junction temperature versus forward voltage behaviors of LEDs have been investigated in steady state and thermal equilibrium conditions. Calibration equations have been created to form the relationship between two significant parameters for each LED. During the calibration phase of the measurements, oven temperatures have been set to approximately 30, 50 and 70˚C and experiments have been repeated for each LED three times. Forward voltages of pulse current applications at different oven temperatures are given as follows both in the text and the graphs for each LED type.

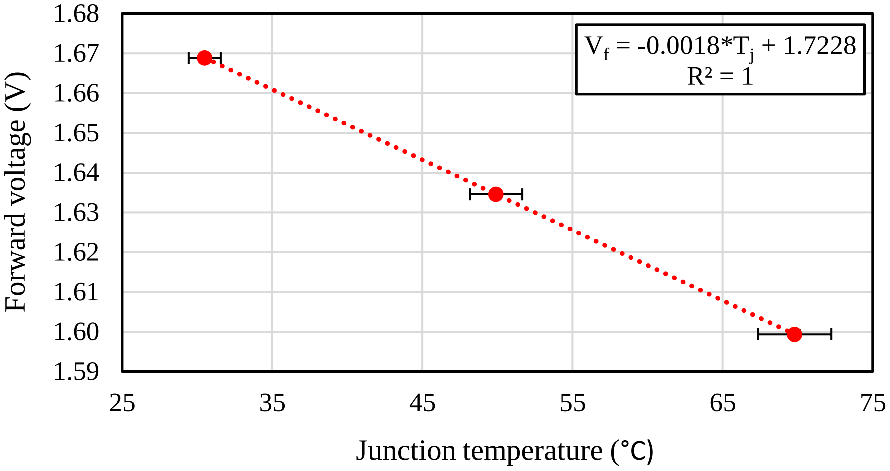

Figure 38: Calibration equation for a red LED chip

1.66887, 1.63454 and 1.59935 V forward voltage results have been obtained respectively in 30.5, 49.9 and 69.8˚C oven temperatures for a red LED chip. The slope of calibration equation for the red LED chip has been calculated bigger than the slope of the blue LED chip and smaller than the slope of green LED chip.

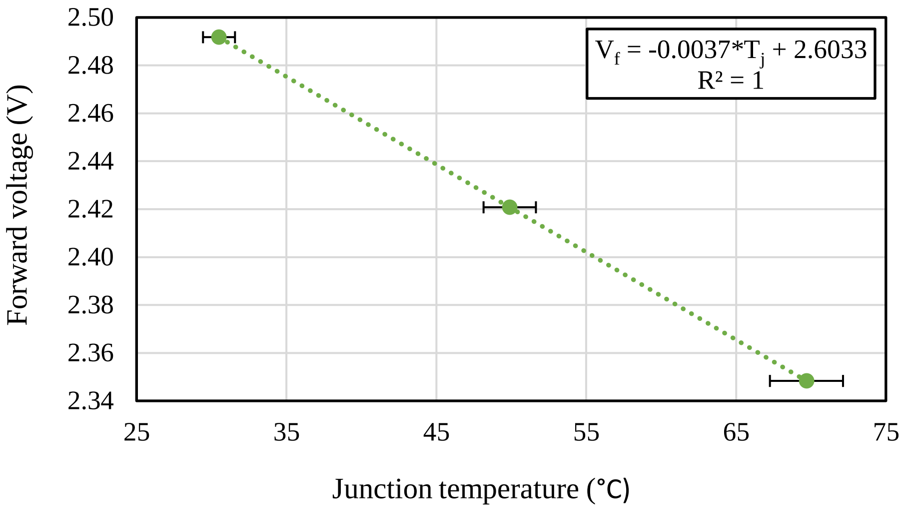

Figure 39: Calibration equation for a green LED chip

2.49174, 2.42077 and 2.34831 V forward voltage results have been obtained respectively in 30.5, 49.9 and 69.7˚C oven temperatures for a green LED chip. The slope of calibration equation for the green LED chip has been found to be the largest one among other chips.

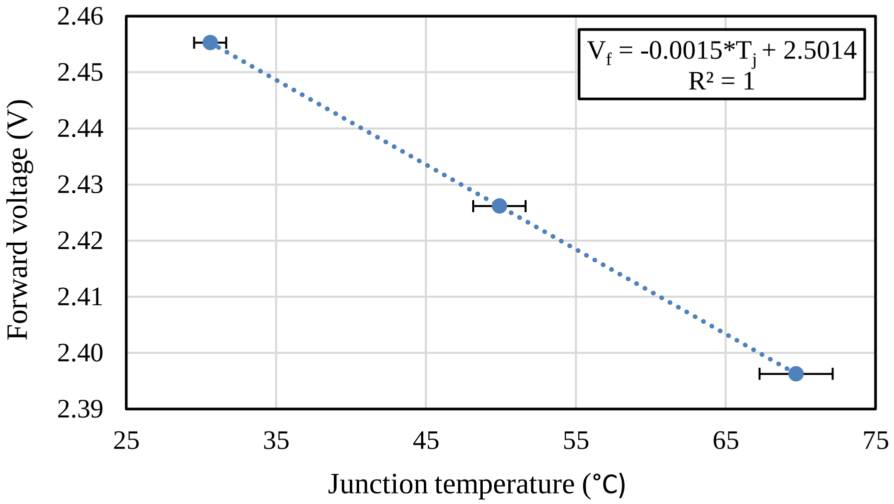

Figure 40: Calibration equation for a blue LED chip

2.45527, 2.42615 and 2.39628 V forward voltage results have been obtained respectively in 30.6, 49.9 and 69.7˚C oven temperatures for a blue LED chip. The slope of calibration equation for the blue LED chip has been found to be the smallest one among other chips.

After setting the relationship between junction temperature and forward voltage of LEDs, LEDs were operated at their normal working condition at 100 and 200 mA driving currents and forward voltage, junction temperature, radiant power and heat generation behaviors of each LED have been characterized and compared.

2.3.2 Electrical, Thermal and Optical Behaviors of Single RGB LEDs

Test phase of the junction temperature measurements has been conducted as described in Section 2.1.1. After steady state and thermal equilibrium conditions are reached, the driving current was dropped to the pulse current and forward voltage data of a pulse current was recorded for RGB LEDs for the 100 mA and 200 mA application currents. Measurements were conducted at 22.7°C ambient temperature.

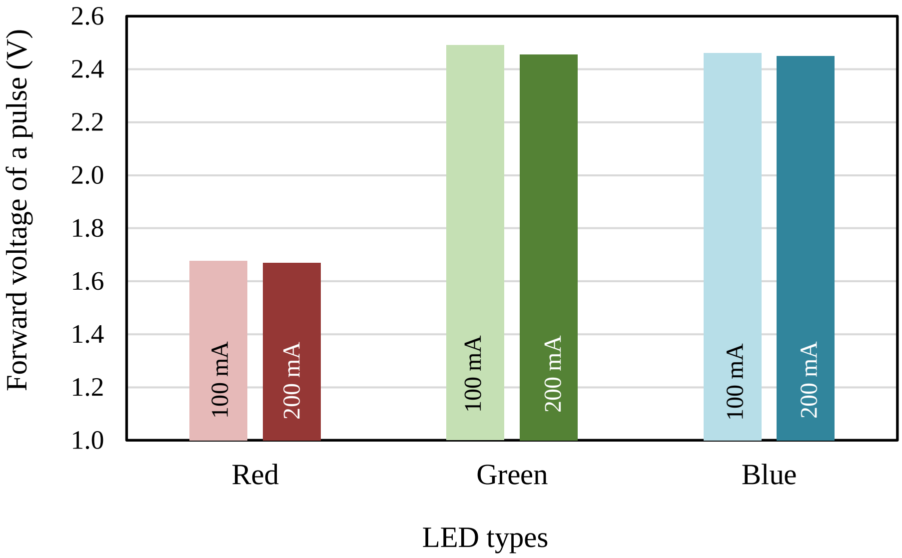

Figure 41: Comparison of RGB LEDs in terms of forward voltage behaviors after the pulse current application (1 mA for 1 ms)

Comparison of forward voltage of a pulse current application was made between two driving currents and RGB LEDs in Figure 41. As it can be seen from the figure, from 100 mA to 200 mA, the largest drop was observed in the green LED as 0.03 V while the smallest shift was seen in the red LED as 0.008 V. When different types of LEDs are compared, the difference between InGaN (green and blue) and AlGaInP (red) LEDs is clearly seen. Upon pulse current application, InGaN LEDs had much higher forward voltage (around 32%) than AlGaInP LEDs, while green and blue LEDs have shown a very close behavior with around only 1% difference. Variation in forward voltage behavior of LEDs critically affected the junction temperature behavior of LEDs as observed in Figure 42.

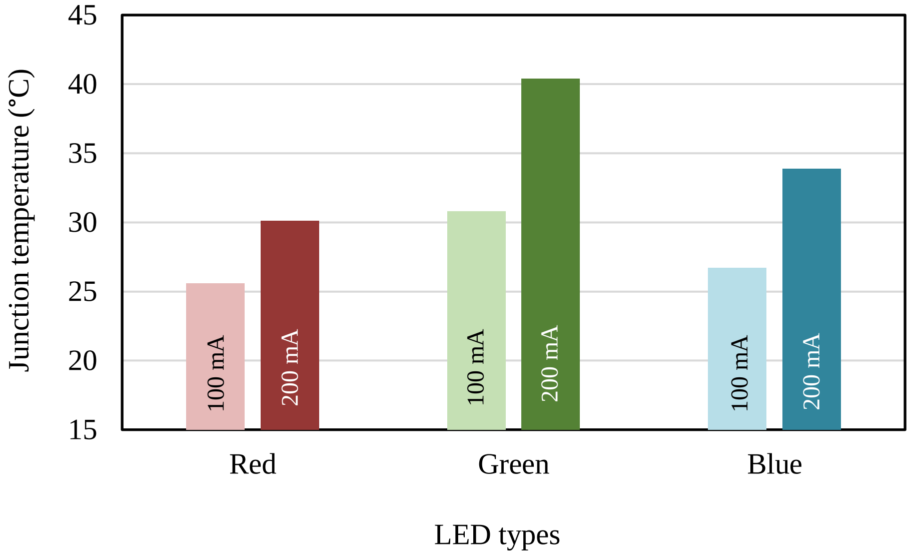

Figure 42: Comparison of RGB LEDs in terms of junction temperatures obtained at two different driving currents (100 and 200 mA)

With the use of calibration equations, junction temperatures of RGB LEDs have been determined for 100 and 200 mA driving currents. The most change in junction temperature was noticed in the green LED by 9.6°C after rising the driving current to 200 mA. On the other hand, the red LED showed the minimum change by 4.5°C. In order to better characterize thermal conditions of LEDs in terms of heat generation and the impact of thermal state on optical performance, radiant power was measured at steady state operations of LEDs.

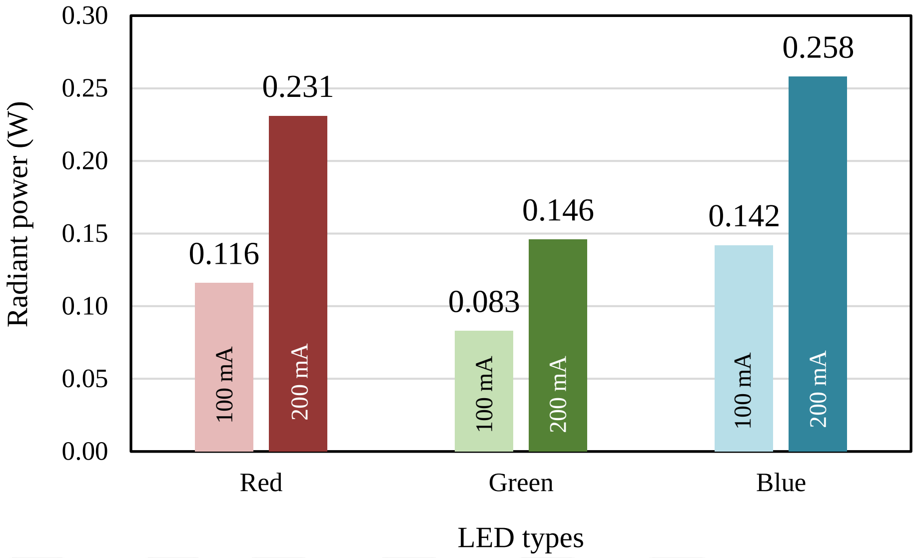

Figure 43: Comparison of RGB LEDs in terms of radiant power values obtained at two different driving currents (100 and 200 mA)

Optical measurements have been conducted in an Integrating Sphere as described in Section 2.1.1. As one of the most significant parameters, the change in radiant power of LEDs was measured and different behaviors of RGB LEDs were compared along with the junction temperature measurements. From 100 mA to 200 mA, the red LED chip indicated a much higher change with a 99.1% increase in radiant power while other LEDs showed a close behavior. (75.9% for the green, 81.7% for the blue LED chip).

Electrical input powers of LEDs were also determined with the measurements of forward voltage and driving current and heat generation rates were found for each LED with the subtraction of radiant power from electrical input power as seen in Figure 44. The largest amount of heat generation (0.519 W) was observed in the green LED operating at 200 mA driving current while the lowest heat generation at 200 mA was measured for the red LED as 0.206 W.

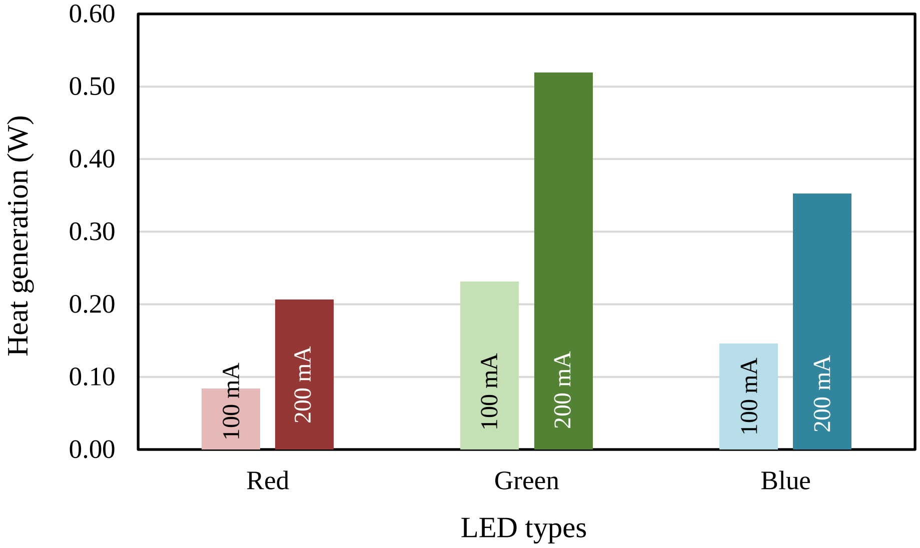

Figure 44: Comparison of RGB LEDs in terms of heat generation values obtained at two different driving currents (100 and 200 mA)

As a result of the analysis, at 200 mA driving current, radiant power to electrical input power ratio was found to be the highest for the red LED (52.9%) while having the lowest junction temperature at the same time (30.1°C). Thus, special attention was given to characterization of high-power red LEDs in terms of thermal, optical and electrical behaviors in Section 2.2.

2.4 A Novel Junction Temperature Measurement Technique for Multi-LED Systems

2.4.1 Measurement Approach

In a previous study, it was described that as a single LED is running at its normal driving current, the current is dropped to the pulse current suddenly when it reaches to the steady state for a very small duration and the forward voltage is recorded at that pulse current. This voltage reading is then plugged into the calibration equation and the junction temperature is determined. However, in the case of a multi-LED system, a single LED cannot be controlled individually because the only way to run the LEDs is to power the electrical circuit. Thus, a multi-channel sourcemeter system is required to perform junction temperature measurements of each LED in a multi-LED system. To control each LED, additional electrical wires were soldered to the conductive leadframe of LEDs and then those wires were connected to the second channel of a sourcemeter. The electrical cable of the PCB circuit was also connected to the first channel to run the multi-LED system in normal operation. These electrical connections are described in Figure 45, where the LED-1 is controlled in this case.

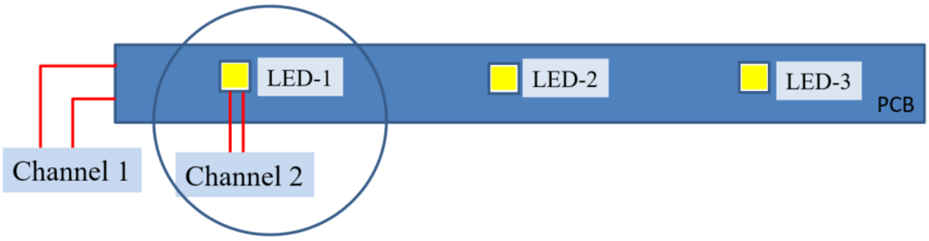

Figure 45: Electrical connections of two channels of a source-meter device for junction temperature measurements of LEDs

When the steady state is reached, all LEDs are switched off for 1 ms and the LED whose junction temperature is to be measured is pulsed simultaneously with a 1 mA current for 1 ms. Junction temperatures of other LEDs are also determined when the extension cable from the second channel is connected to the electrical wires of individual LEDs and the same procedure is applied respectively. As a result, junction temperature of each LED chip on the PCB can be determined separately. The simultaneous operation of two channels and measurement procedure can be seen more clearly in Figure 46. It should be noted that pulse currents are applied ten times and average forward voltage reading is recorded to increase the accuracy of the measurements.

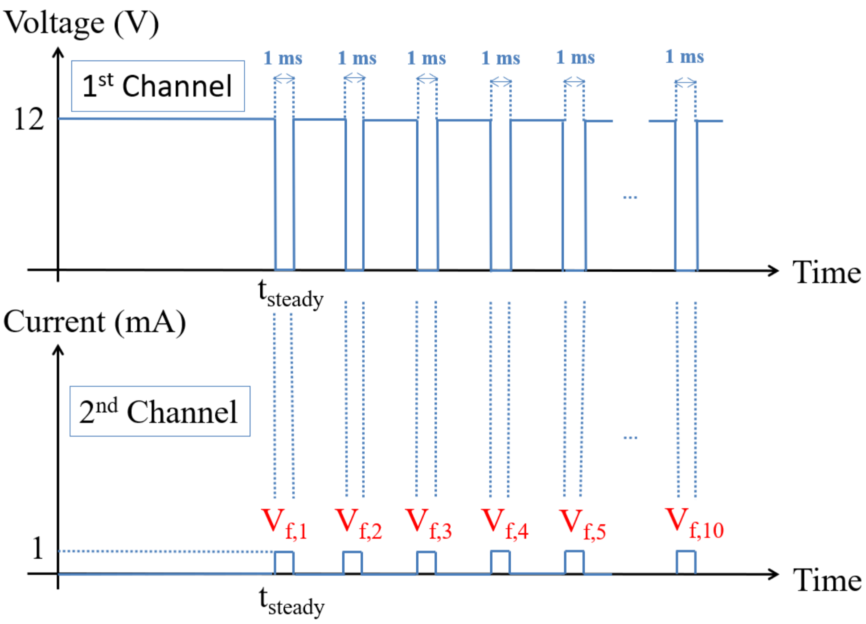

Figure 46: Junction temperature measurement technique for multi-LED systems

2.4.2 Multi-chip LED System Measurements

In order to have more reliable results, V_f measurements were repeated ten times and a special care was given to the variation in repeated V_f readings. After the small pulse currents (1 mA) were applied, the average forward voltage readings were matched with the PCB temperature of LEDs in steady state and thermal equilibrium conditions. Table 3 shows the calibration data sets which relate the junction temperature of LEDs with their forward voltages.

Table 3: T_j versus V_f calibration data set

Junction temperature (°C)	Forward voltage (V)		
	LED-1	LED-2	LED-3
30	2.5547	2.5529	2.5538
40	2.5417	2.5399	2.5408
50	2.5287	2.5269	2.5278
60	2.5157	2.5139	2.5148
70	2.5027	2.5009	2.5018

Using these datasets, the calibration equations were derived for each LED presented in Figure 47, Figure 48 and Figure 49. It can be observed that the calibration equations are very similar since the same type of LED is used.

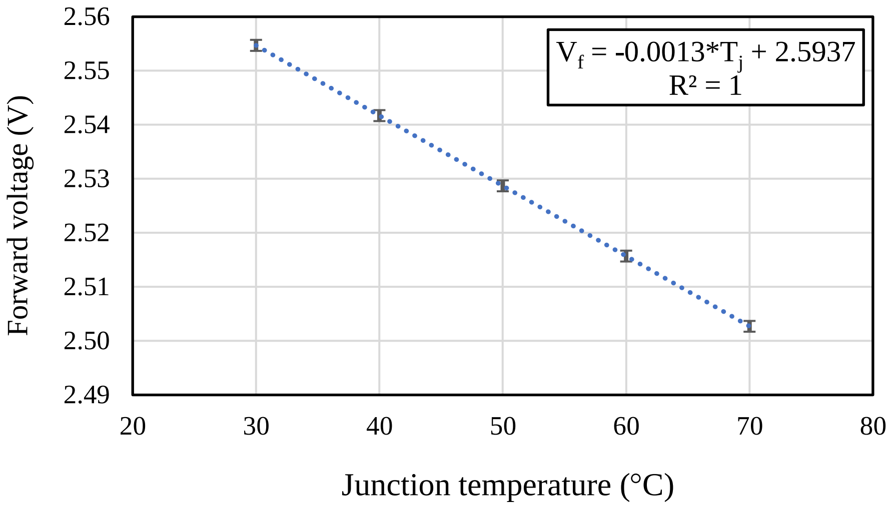

Figure 47: Derivation of a calibration equation for LED-1

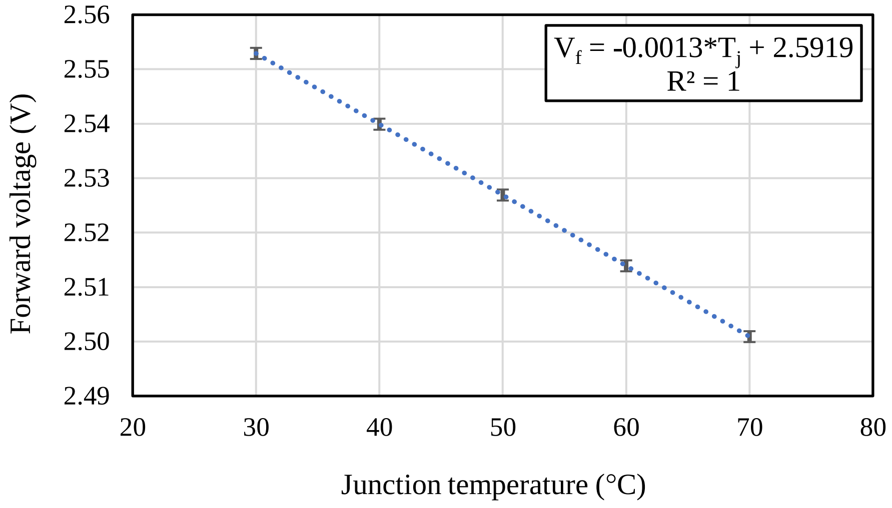

Figure 48: Derivation of a calibration equation for LED-2

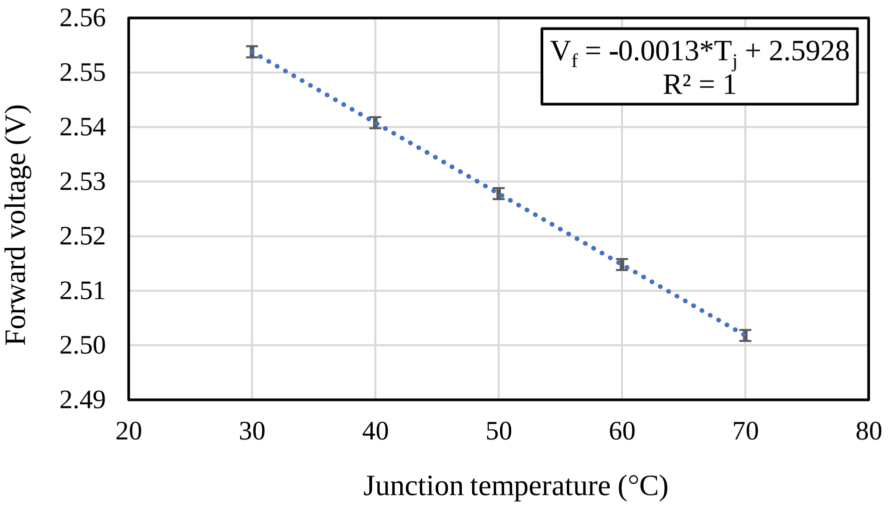

Figure 49: Derivation of a calibration equation for LED-3

These calibration equations were utilized to determine the junction temperature of each LED. Therefore, it is very important to establish a correct relationship between the junction temperature of LEDs and the forward voltage drop. Although relationship between junction temperature and forward voltage is very similar for each LED, LED-2 is slightly more sensitive to junction temperature while LED-1 is slightly less affected by the junction temperature.

Test phase of the junction temperature measurements and optical tests were conducted in normal ambient conditions and all tests were made in a steady state operation, which we defined as a variation of 0.1°C in board temperature over a period of 15 minutes for the current system. Although normal operation of the system is realized by applying 12 V, experiments were conducted in five different voltages (10 V, 10.5 V, 11 V, 11.5 V and 12 V) to observe thermal and optical behavior of LEDs under various electrical conditions.

Voltage and current measurements were carried out during the tests performed just before the pulse current application, and potential difference on each LED was recorded. For more detailed characterization of the PCB, PCB voltage, PCB driving current, LED voltage and electrical power values of each LED at five voltages were determined respectively as it is seen in Table 4 and Table 5.

Table 4: LED voltages for various PCB voltage and current magnitudes

PCB voltage (V)	PCB current (mA)	**LED voltage (V)**		
		LED-1	LED-2	LED-3
10.0	71	2.940	2.911	2.949
10.5	105	3.037	2.997	3.040
11.0	140	3.127	3.076	3.120
11.5	150	3.149	3.096	3.143
12.0	148	3.144	3.090	3.136

Table 5: Electrical powers of LEDs for various PCB voltage and current magnitudes

PCB voltage (V)	PCB current (mA)	**Electrical power (W)**		
		LED-1	LED-2	LED-3
10.0	71	0.2087	0.2067	0.2094
10.5	105	0.3189	0.3147	0.3192
11.0	140	0.4378	0.4306	0.4368
11.5	150	0.4724	0.4644	0.4715
12.0	148	0.4653	0.4573	0.4641

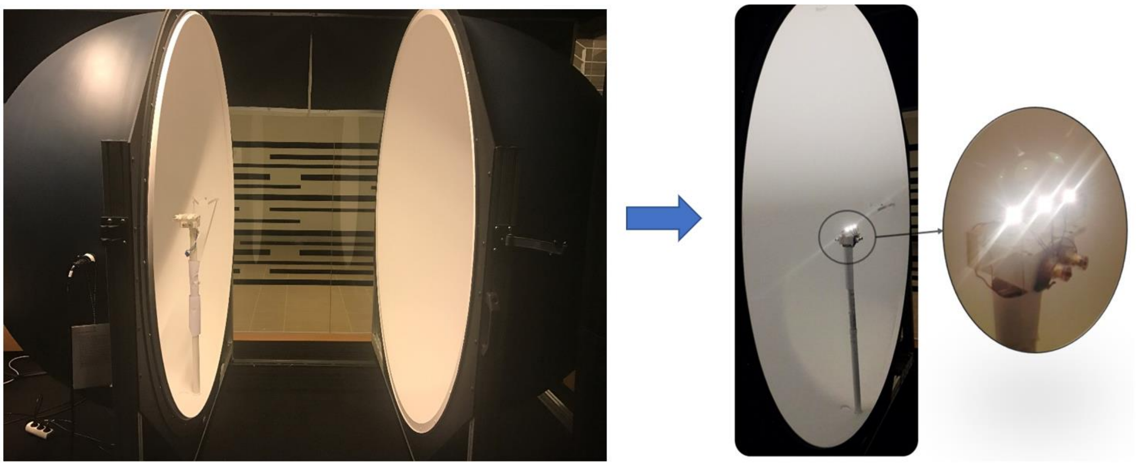

Figure 50: Optical measurements of the multi-LED system

Optical measurements were implemented in a 2-meter diameter Integrating Sphere System, which is calibrated with a standard reference light source whose specifications are certified under certain limits. The device under test (DUT) was located at the center of the Integrating Sphere and another calibration was conducted to introduce the available losses of the LED system to the measurement system. The experimental setup for optical measurements of the multi-LED system is shown in Figure 50 during operation. As it is noticed, the PCB was placed on a plexiglass block whose thermal conductivity is approximately 0.2 W/m-K since it was aimed to prevent extra cooling of the PCB in a mounting position.

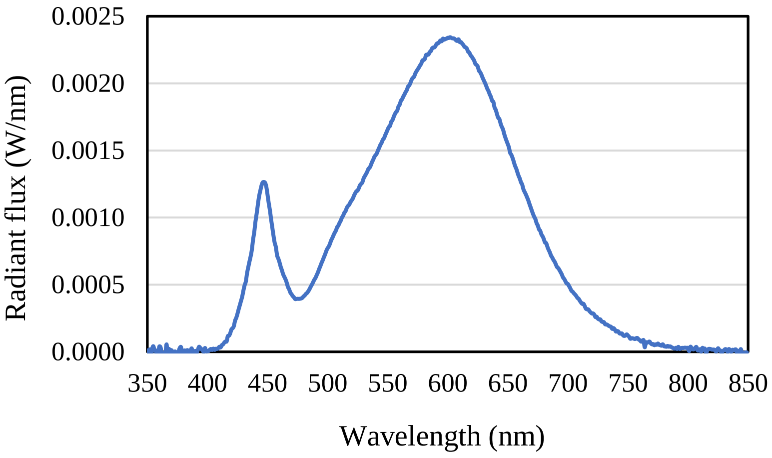

Figure 51: Radiant flux distribution of the multi-LED system operating at 12 V

Distribution of radiant flux over the electromagnetic spectrum between 350 and 850 nm is given in Figure 51 for the LED system working at 12 V. Optical results including radiant flux (E_r), luminous flux (lm) and dominant wavelength (nm) were determined using this graph. Tests were also repeated for other electrical conditions defined in Table 4 and Table 5.

In this section, thermal, optical and electrical characteristics of LED-1, LED-2 and LED-3 on a PCB were analyzed and compared to characterize the performance of a multi-chip system under various operating conditions. First, T_j versus V_f behavior of the multichip system was derived, then the junction temperatures of each LED were determined at their normal operating conditions. Optical tests were also conducted in an integrating sphere system in order to understand the effect of thermal conditions on optical performance.

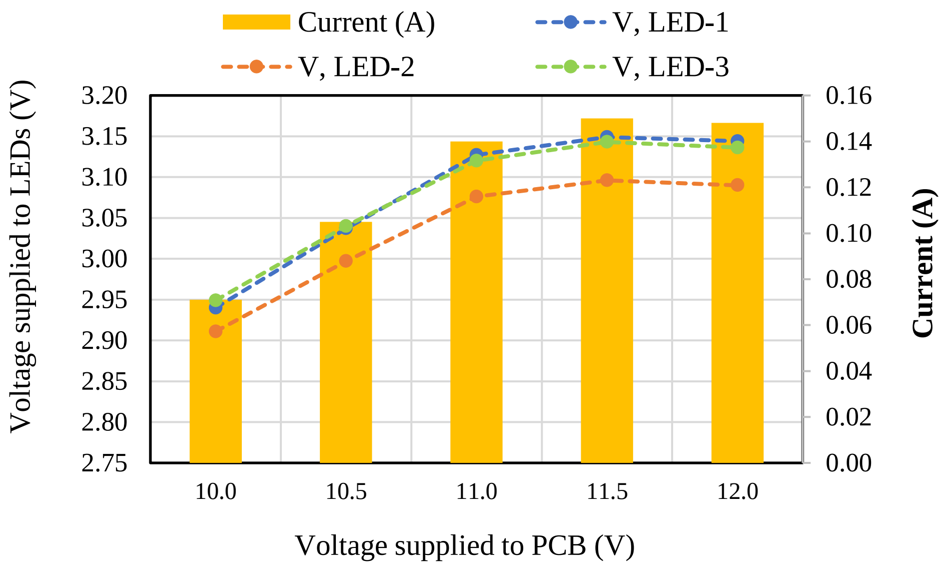

Figure 52: Characterization of electrical conditions during junction temperature and optical measurements

Figure 52 shows the results of electrical tests which were made during junction temperature and optical measurements. The Printed Circuit Board (PCB) was operated at five different voltages and the corresponding forward voltages and currents of each LED were measured during operation. Since LEDs are serially connected, they were driven by the same magnitude of current. Thus, the driving currents of LEDs for each voltage application is represented by the columns on which voltage values of individual LEDs are also given as a scatter plot. It is clearly seen that the currents and individual voltage values are following a similar trend, and both increase significantly when the board voltage is applied between 10 V and 11 V. The variation in current and voltage values is less when a potential difference higher than 11 V is applied. Experimental results also indicate that while the voltage supplied to LED-1 and LED-3 shows a very close behavior, it is noticeably less for LED-2 by around 1.5% compared to LED-1 and LED-3.

Figure 53 demonstrates the electrical power of each LED when different voltages are applied to PCB. As it is expected from the current and voltage behavior in Figure 52, LED-2 consumes the lowest electrical power at each voltage application. At 12 V, it is 1.75% lower than the one for LED-1, whose electrical power is slightly higher than LED-3.

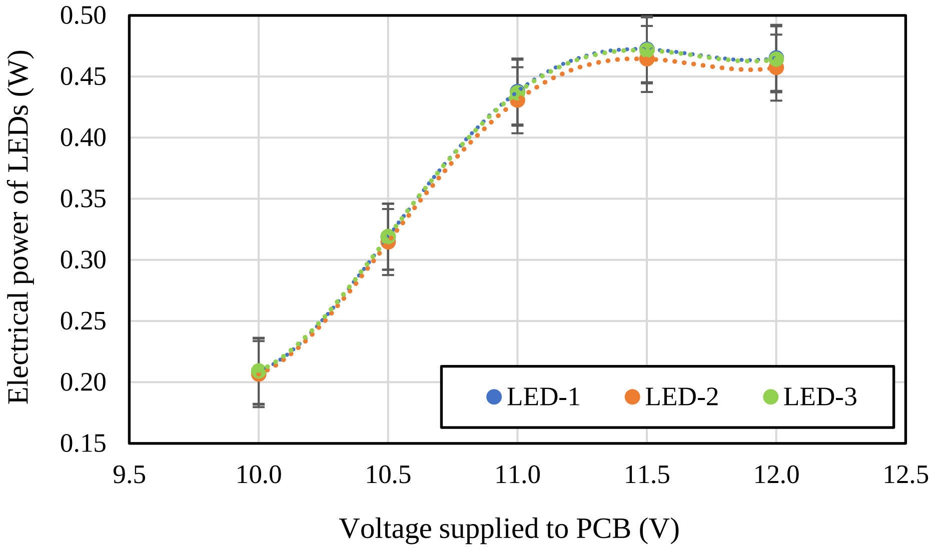

Figure 53: Variation of electrical power of LEDs with the voltage supplied to the light engine

After determining the electrical conditions at which each LED was operated, the junction temperature rise over ambient temperature was investigated in Figure 54 and Figure 55. In each experiment, it is clearly observed that the LED-3 has the highest junction temperature. This is attributed to the existence of electrical components close to LED-3 (diode, driver and resistance) which also produce a considerable amount of heat. Although the LED-2 was operated with the lowest electrical power, it was observed that the increase in its junction temperature was slightly higher than LED-1. The difference became even more noticeable as the provided electrical power to PCB is raised. This can be explained by heat conduction from heat generating electrical components to other parts of the PCB. As seen in Figure 45, the distance between LED-2 and electrical components is almost two times lower than the one between LED-1 and these units. Therefore, the junction temperature of LED-2 is more affected by the additional heat loads compared to LED-1. In addition, when the PCB was operated by higher electrical powers, the LED-3 became even hotter than other LEDs. When LED-3 and LED-1 are compared, a 1.1 W more electrical input power provided to PCB caused almost 11°C difference in a range of junction to ambient temperatures of two LEDs. The change in junction temperature over ambient temperature with respect to electrical power supplied to the PCB is also seen in Figure 55. As it is seen in the graph, while LED-1 and LED-2 shows almost the same behavior, the junction temperature of LED-3 is elevated by 37.2°C when 1.1 W more electrical power is supplied from 10 V to 12 V.

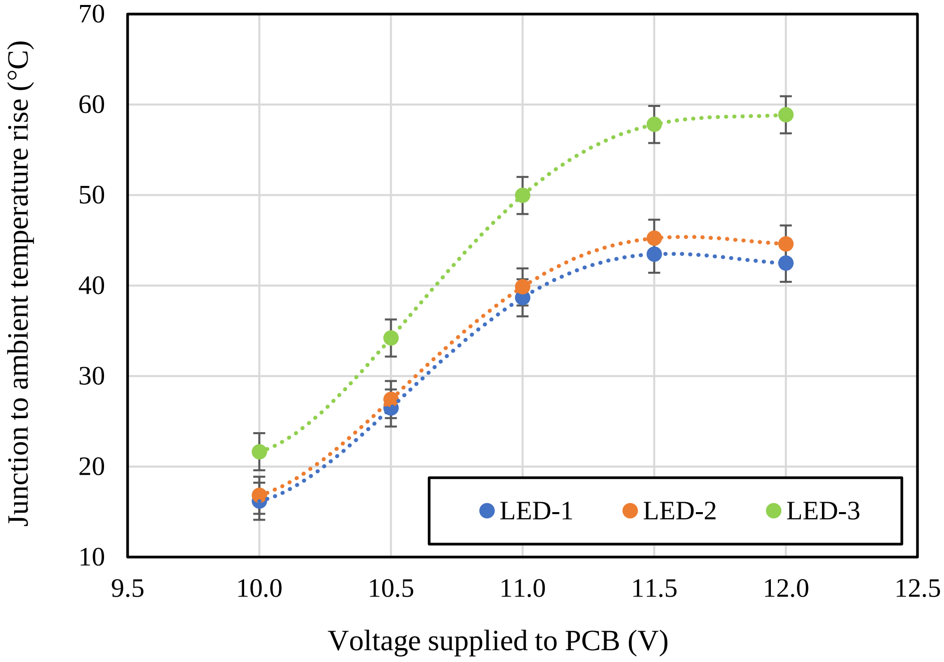

Figure 54: Variation of junction to ambient temperature rise for various voltages

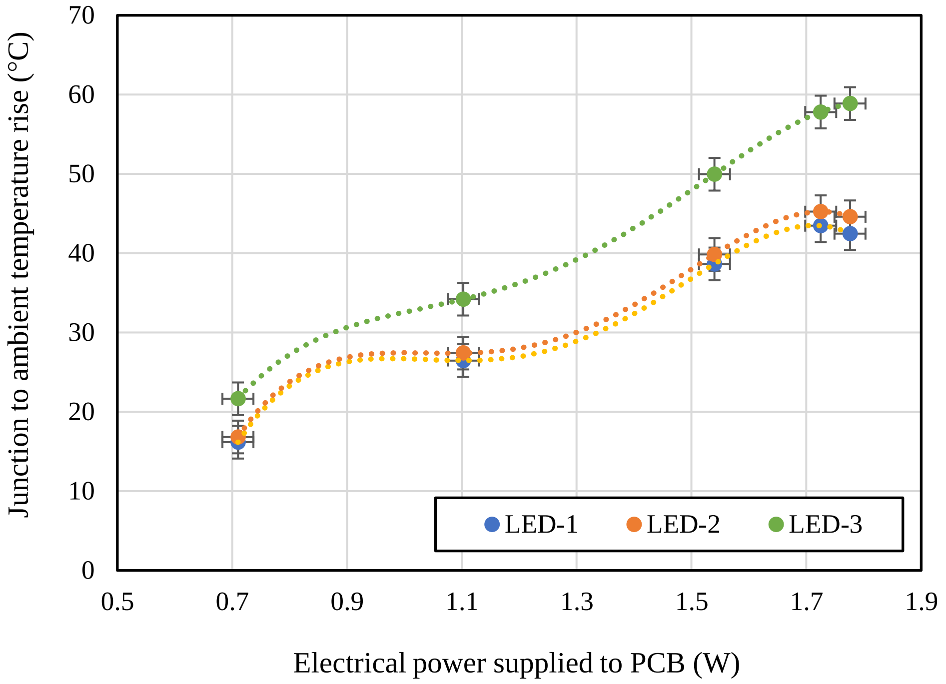

Figure 55: Variation of junction to ambient temperature rise for various power levels

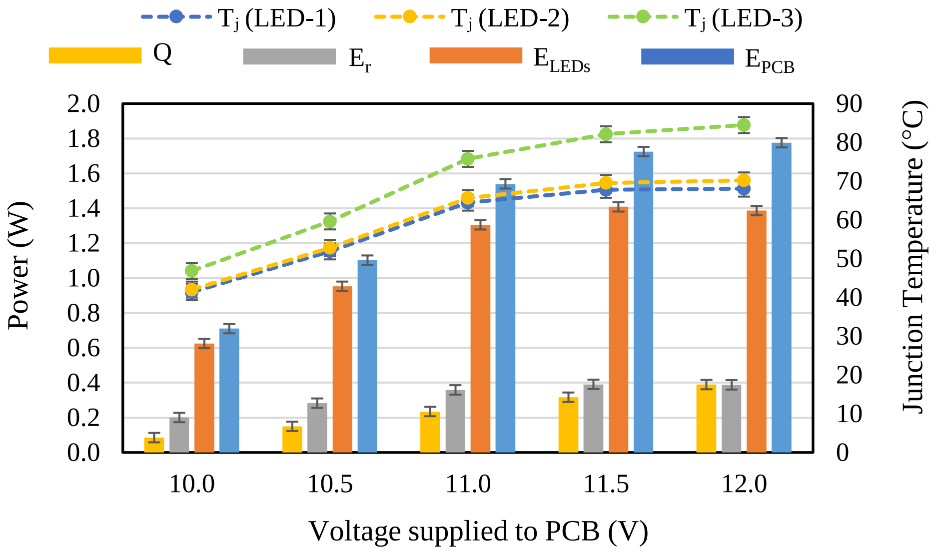

Figure 56: Thermal and optical behavior of Multi-LED system

under various electrical conditions

In order to understand the effects of thermal and electrical conditions on optical performance, electrical power of PCB and only LEDs, radiant power of LEDs, generated heat over the PCB and junction temperatures of LEDs were determined as it is seen in Figure 56.

Heat generation due to additional electrical components placed on the PCB was obtained by subtracting electrical input power of three LEDs from total electrical power supplied to the PCB. In addition, heat generated from all LEDs was determined by subtracting total radiant power from electrical input power of LEDs. Thus, the difference between orange and gray columns in Figure 56 can be regarded as the total heat generation of LEDs, which are 0.42 W, 0.67 W, 0.95 W, 1.02 W and 1.0 W respectively for different voltages supplied to the PCB from 10 V to 12 V in 0.5 V intervals. The heat generation due to extra electrical components was also demonstrated in the graph to better analyze its negative effect on the optical performance. The results indicate that the heat loss from these parts is gradually increasing as the electrical input power of the PCB is raised. Although the heat generation from additional components is about 42.5% of the total radiant power at 10 V, the generated heat approaches the same amount as the radiant power measured at 12 V as the voltage increases. This can be considered an important thermal problem and needs to be addressed with a better circuit design. In fact, heat generation from these components increases by 3.6 times as the PCB voltage rises from 10 V to 12 V. Although the radiant power of the LEDs is increased by approximately 94% in the same voltage range, higher radiant energy output potential is prevented with more heat generation and elevated junction temperatures of the LEDs. This is especially the case for LED-3, whose junction temperature increased significantly compared to LED-1 and LED-2.

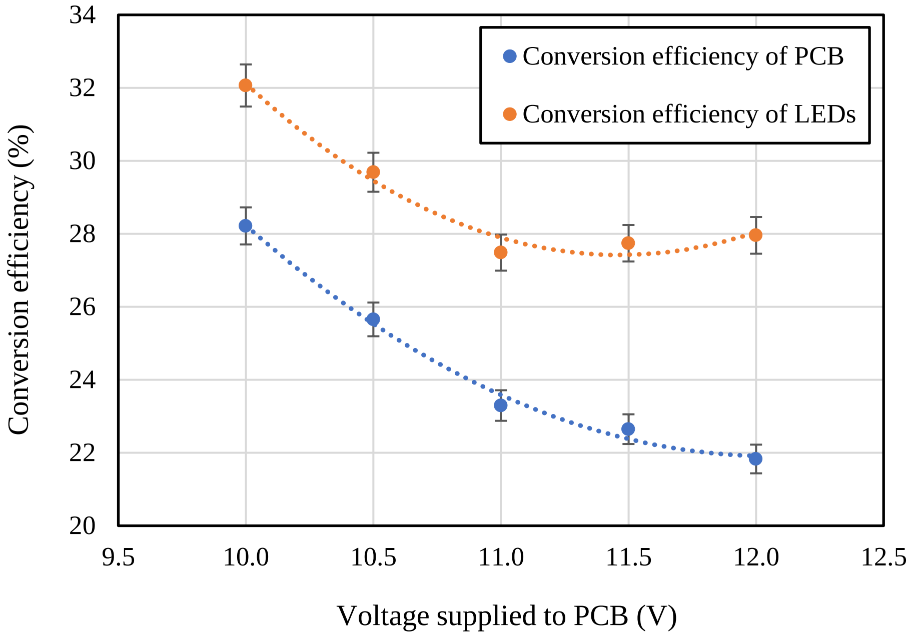

Figure 57: Variation of conversion efficiency of PCB and LEDs with voltage supplied to PCB

Radiant power of LEDs, electrical input power of the PCB and total electrical power of LEDs given in Figure 56 was utilized to determine the conversion efficiency of the PCB and LEDs separately in Figure 57. The reason why PCB and LEDs are compared is to observe the negative effect of extra heating on the board due to the electrical components. When electrical components were placed on the PCBs, the decrease in the conversion efficiency was 12%, 13.6%, 15.2%, 18.4% and 21.9%, respectively, from 10 V to 12 V. It was found that the conversion efficiency of the PCB at 12 V is 21.8% while the conversion efficiency of LEDs is 27.9%.

After characterizing the optothermal behavior of the multi-chip LED system in terms of radiant power and conversion efficiency, further research was conducted to examine the effect of junction temperature on dominant wavelength, luminous flux and luminous efficacy. These essential properties of LEDs are important to evaluate the energy emitted in a spectrum that the human eye can perceive as light. Since luminous efficacy is directly related to the cost efficiency of the LED product, it is also important to know the change of light efficiency with electrical power and junction temperature of the multi-LED system operating under normal conditions.

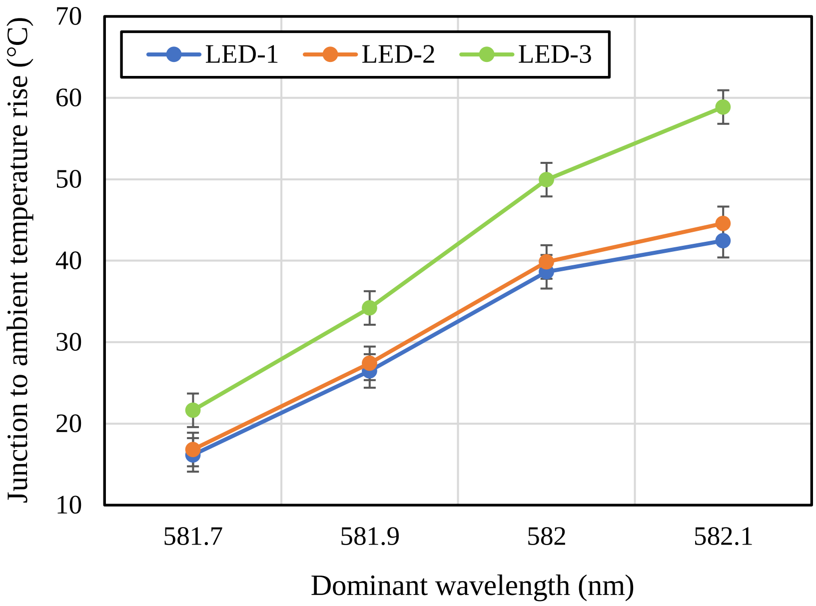

Figure 58: The effect of junction temperature over dominant wavelength of the multi-chip LED system

In Figure 58, the change of dominant wavelength with respect to junction temperature over ambient temperature is given as the PCB voltage is increased from 10 V to 12 V. As it is expected, dominant wavelength shifts to the right of the spectrum at higher junction temperatures. In the experiments, it was observed that dominant wavelength was raised by 0.4 nm from 10 V to 12 V.

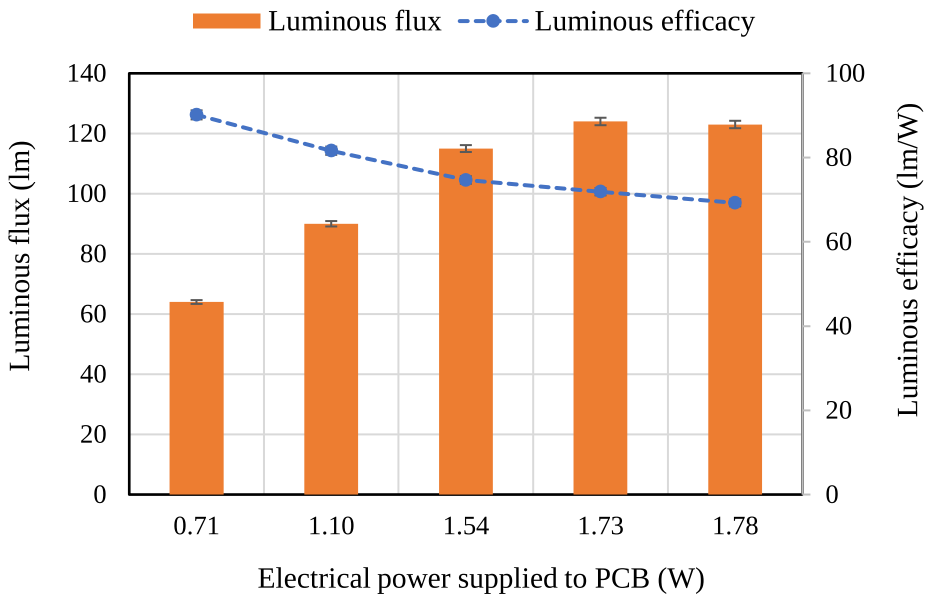

Figure 59: Variation of luminous flux and efficacy with electrical power supplied to PCB

Figure 59 shows the variation in luminous flux and luminous efficacy with respect to the electrical input power of the PCB while the application voltage varies between 10 V and 12 V. It has been found that luminous flux of the LED unit has increased significantly, especially as the voltage is increased from 10 V to 11 V. In addition, the luminous efficacy shows a decaying trend as the electrical power and junction temperature of LED board rises. In fact, approximately 1 W increase in the supplied power to the PCB resulted in 23% drop in luminous efficacy.

2.4.3 Temperature Distribution and Local Hot Spots over the LED Board

While junction temperature of an LED significantly affects the performance of the lighting systems, local hot spots that appear in different parts of an LED package or the system components also drag down the performance of the system and lead to shortened lifetime. Thus, especially in multi-chip systems, it is critical to investigate thermal distribution over the system components other than measuring only the junction temperature of LED chips. This is even more critical in phosphor coated LEDs or the LED systems which are composed of intensive electronics.

In this study, temperature profile of an LED board on which serially connected LEDs, and additional heat generating components are located has been examined. These components consist of a diode, resistor and driver. Temperature profiles in three different regions of almost equal lengths have been examined. These are the close regions to the LED-1, LED-2 and LED-3 as seen in Figure 60, Figure 61 and Figure 62.

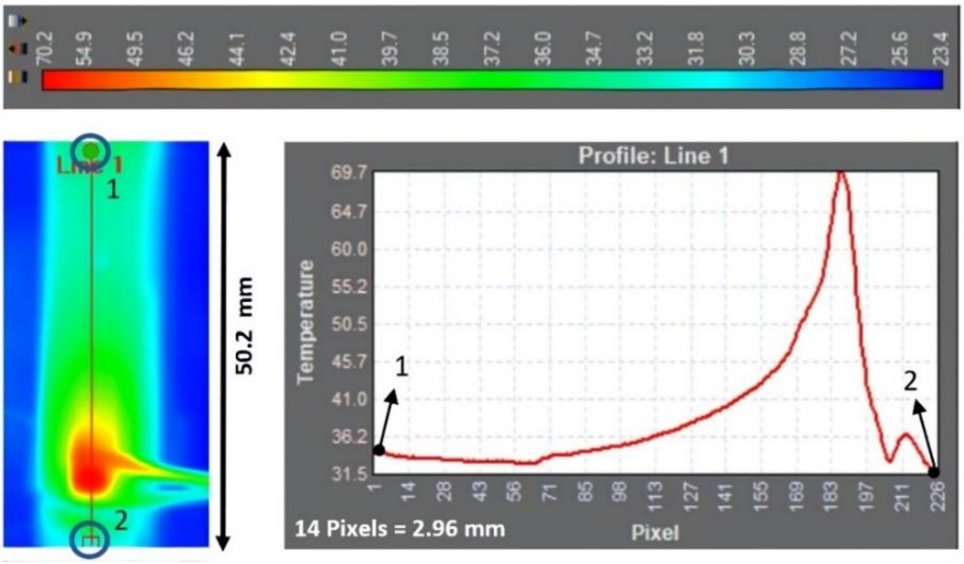

Figure 60: Thermal image of LED-1 with an IR thermal camera

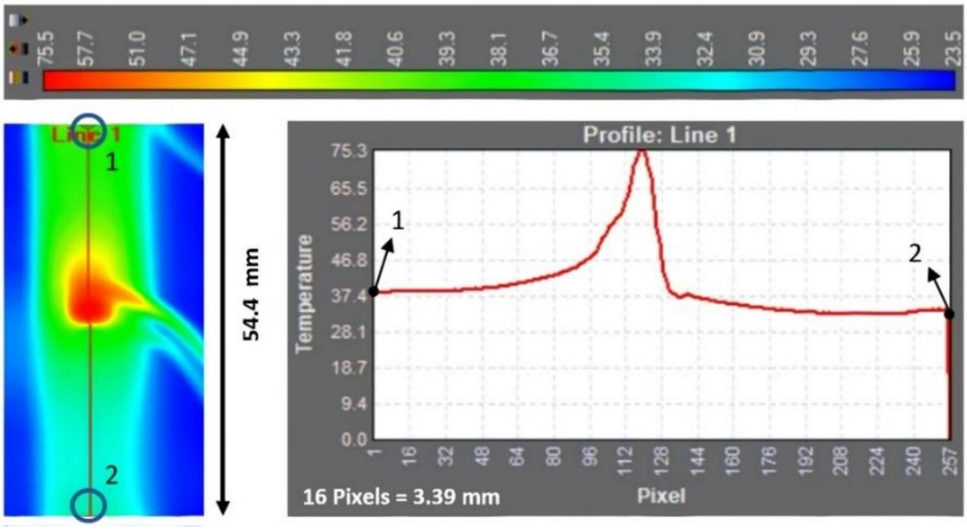

Figure 61: Thermal image of LED-2 with an IR thermal camera

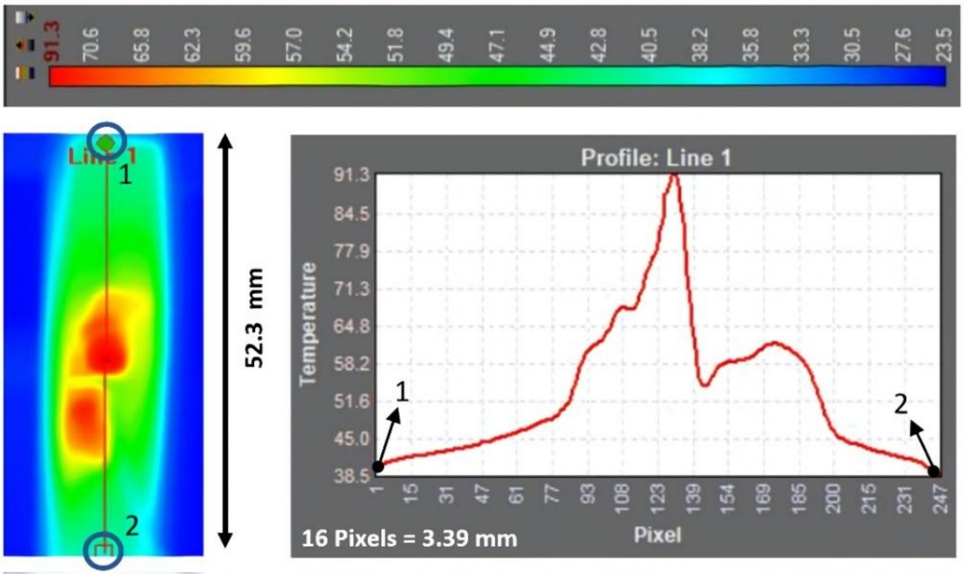

Figure 62: Thermal image of LED-3 with an IR thermal camera

In the LED-1 region where there is no additional component that produces heat, from the middle section of the board to the LED side, temperature profile is changing smoothly in the form of an exponential function and temperature plummets in the region between the LED chip and the board end. In another side of the board, from the middle section of the board to the LED side, the exponential profile trend is disrupted due to the additional components that generate heat in a proximity of the LED chip. In even another side of the chip, exponential drop of temperature is not as smooth as observed in the region close to LED-1.

The highest temperature in the board (91.3°C) is measured on LED-3 due to the heat generating components around it. Temperature gradually decreases from LED-3 to LED-1 side as expected. Furthermore, surface temperatures of phosphor layers have been found to be higher than the junction temperatures of all three LEDs as compared in Figure 63. It was observed that the difference between junction temperature and phosphor temperature was even getting larger as approaching local hot spots. Since the raised temperature of a phosphor layer negatively affects the blue-to-white light conversion, performance of the lighting system in terms of light output, color characteristics, lifetime and efficiency of the system is considerably affected. Thus, future studies need to improve the phosphor coating techniques to get the maximum performance in both thermal and optical aspects.

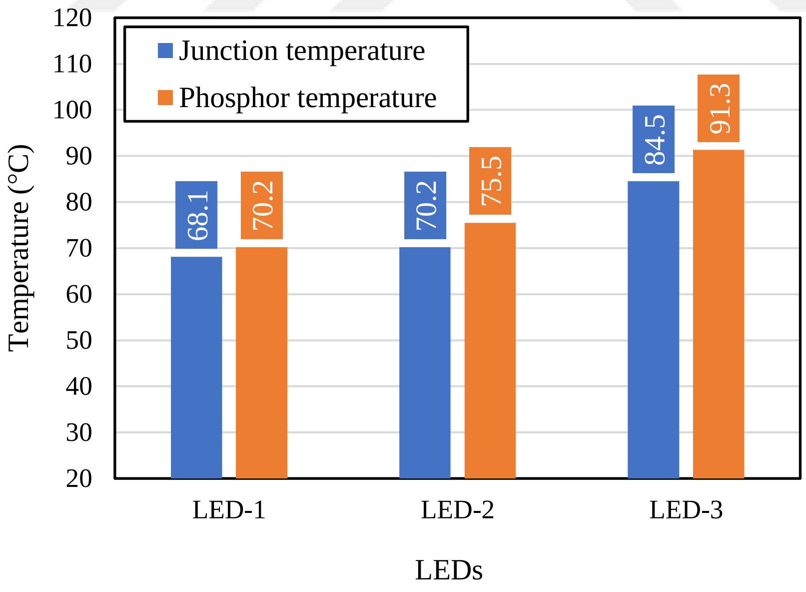

Figure 63: Comparison of junction and phosphor temperatures of three LEDs on the multi-LED system

In another study, a multi-chip LED system was operated with the application of 24 V at 23°C ambient temperature and thermal behavior of individual LEDs was determined with junction temperature measurements to characterize thermal condition of the LED system as seen in Figure 64.

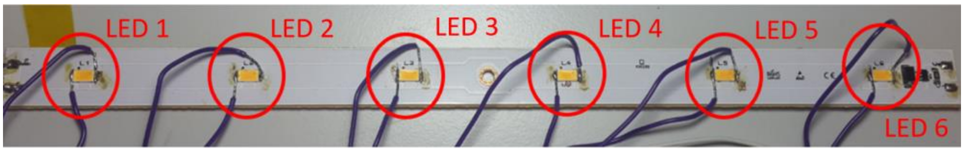

Figure 64: A white multi-chip LED system for junction temperature measurements

It was noticed that the LED 6 has the highest temperature since it is located in a very close position to electrical components in the lighting unit. As the distance from the electrical units increases, junction temperatures of LEDs are observed to be gradually decreasing; however, the junction temperature of LED 2 is measured to be the second highest (Figure 65). This is also supported by solder point measurements with T-type thermocouple and attributed to the inappropriate packaging of LED 2 on the circuit board that contributed to the increase in total thermal resistance of the LED package.

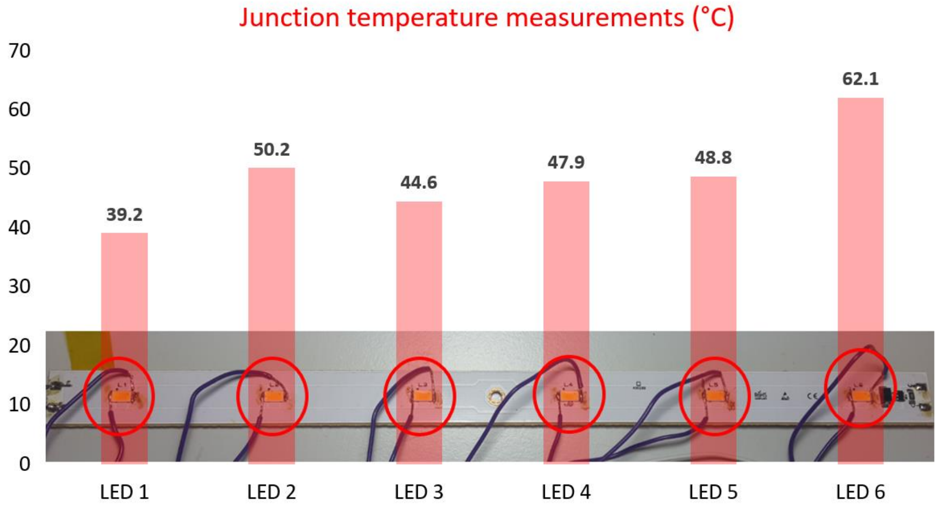

Figure 65: Junction temperature distribution of LEDs in a white multi chip LED system

In conclusion, findings in the temperature profile of the multi-LED system demonstrates that thermal symmetry is significantly altered especially in multi-LED systems with phosphor coated LEDs and heat generating elements. Thus, a reliable junction temperature measurement method without one-dimensional heat path assumption is useful in understanding the optothermal behavior of such an LED system as shown in this study.

CHAPTER III

DEVELOPMENT OF A HIGHLY FUNCTIONAL JUNCTION TEMPERATURE MEASUREMENT SYSTEM

3.1 Technology Bottleneck

As LED systems are extensively used in a great number of niche applications, demanding operational conditions induce significant thermal issues and thermal management of optothermal devices increasingly play a significant role in highly reliable systems. High heat generation rates and increased junction temperatures in LED systems not only affect the lifetime of the products but also reduce lumen output, optical efficiency and light quality. To combat with these problems, novel design approaches are continuously developed to improve thermal and optical performance of lighting products. To minimize product development cycles with the highest accuracy and rapid quality checks, reliable measurement systems are a must for professionals in any field. As a thermal characterization parameter that directly affects the optical characteristics, accurate junction temperature measurement is a critical task for thermal engineers, lighting architects and other professionals who want to get the best in their products.

Considering the measurement techniques for the junction temperature measurement, the previous studies point out different approaches including Raman Spectroscopy, Photothermal Reflectance Microscopy, Thermal Imaging and Forward Voltage Change. However, Forward Voltage Change Method is suggested as the most applicable technique in terms of yielding the highest accuracy and offering the most practicality.

3.2 *Problems with Available T_j Measurement Systems*

Current measurement devices rely on Forward Voltage Change Method with transient measurement technique which is found to be complicated, costly and time consuming for junction temperature measurements in various studies in literature and user experience notes [79]. Structure function utilized in transient technique is used with the cumulative thermal resistance versus the cumulative thermal capacity plots derived over a one-dimensional heat flow path in LED systems (see Figure 66).

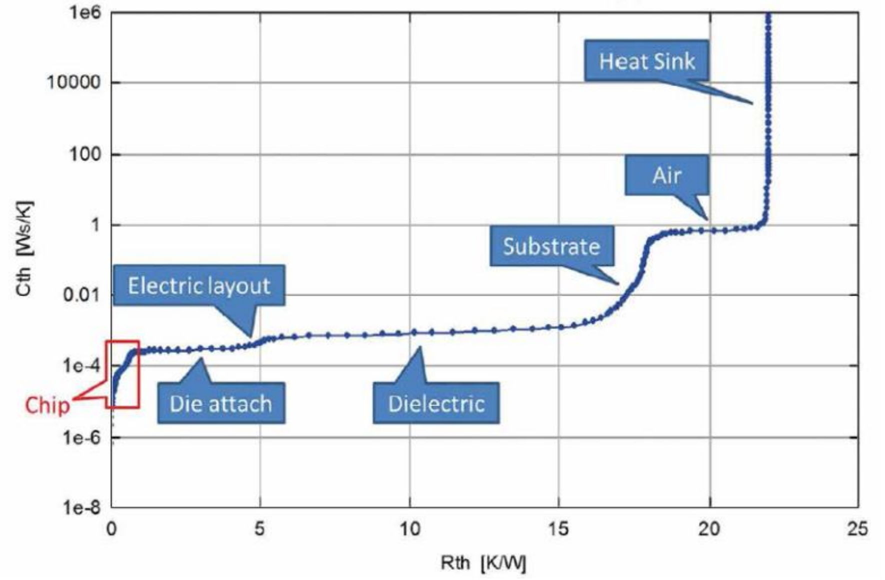

Figure 66: Thermal resistance versus thermal capacitance curve (structure function) derived in transient measurements [82]

The first step for thermal resistance measurement is to apply a step excitation and obtain the time-dependent heating curve of an LED. Then, time-dependent thermal impedance curve of the structure is obtained by dividing the change in temperature of the LED with the step excitation power. After applying Laplace transformation on thermal impedance curve, compact analytical model of the LED is obtained in terms of thermal resistance versus thermal capacitance terms. The curve is represented by Cauer network which is derived with the transformation of Foster network for the identification of a heat-flow path.

In order to obtain the heating curve of LEDs which have a small structure, the sampling and data collection speed of the device should be quite high. At the same time, structure function, which shows the relationship between thermal resistance and thermal capacity, is defined and high measurement frequency and accuracy are required since complex calculations such as convolution, inversion and Fourier transforms are required.

Available junction temperature measurement devices in the market measure junction temperature of LEDs based on thermal characterization data generated with the derived 1D thermal resistance network [83]. However, the increased cost due to required technology behind the measurement method makes this product quite expensive for users who only want to measure the junction temperature of photonic devices. For users who want to get a reliable and practical junction temperature data, sampling rate and data collection resolution of the current systems (1 μs) are found to be too high since they significantly increase the measurement costs [79]. As a result, companies who want to test their products with junction temperature measurements are not able to afford the existing measurement systems and improve their products without obtaining reliable and practical thermal data.

Several doubts have also been raised recently on the accuracy of this method in determining junction temperature due to the alteration of heat flux symmetry especially in general lighting and electronically intensive products. Certain components in an LED package such as phosphor layer and LED lens often impede the spread of heat flow symmetrically [79], [62]. Considering the majority of photonic devices are equipped with components having asymmetric thermal conditions both in the package and the circuit, junction temperature measurements based on the one-dimensional heat flow path is seriously questioned.

Furthermore, measurement devices that do not include the radiometric measurement of photonics products are suspicious in terms of determining their actual thermal resistance values. Since an actual thermal resistance measurement requires the subtraction of the radiated power from total electrical input power, the thermal resistance values which are determined without performing the radiometric measurements can be defined as reference thermal resistance, instead of real thermal resistance of the packages [84]. However, an accurate junction temperature measurement is only possible with the determination of the actual thermal resistance values. Some measurement devices even claim a junction temperature measurement accuracy of 0.01°C although the precision of their forward voltage readings is only limited to 1 mV. In fact, when repeated tests are carried out at the steady state condition, the difference in junction temperature results have been shown to vary between 0.3-0.8°C if the sensitivity of the measured forward voltage data at this condition is equal to 1 mV.

3.3 Advantages of EVAtherm System

In order to address the issues mentioned in the previous section and offer a novel, user-friendly, fast and accurate junction temperature measurement system, a measurement device named EVAtherm has been developed. The measurement method applied in EVAtherm does not include the transient measurement technique with one dimensional heat flow assumption. Instead, steady state junction temperature measurements are carried in a highly automated and efficient manner with increased flexibility for user control accounting 3D heat transfer as in real life applications. The measurement method used in the device was described in Chapter II, Section 2.1.1. In addition, the measurement steps are briefly stated in Section 3.4 in this Chapter. Precisely controlled heating and cooling subsystem of the test chamber reduces the measurement time, allowing a higher number of tests to be conducted in the unit. To provide stable thermal conditions for reliable implementation of the measurements, thermocouple probes are placed in various locations in the chamber, providing ±0.2°C steady state variation in temperature. The test chamber in a compact size of 140 mm x 130 mm x 130 mm operates in between 25°C and 100°C to offer a wide range of calibration and measurement capabilities. With user control settings, measurements can be conducted at various operating conditions without sacrifice in the accuracy. EVAtherm enables the junction temperature measurements of photonic devices to be conducted at a driving current range of 0.1-5000 mA with 1 μV precision of forward voltage reading capability. Depending on the user preference, trade-off between measurement time and accuracy can be made with user settings adjusted in a user-friendly software.

Measurement data collected during the pulse current application and forward voltage reading phases of measurements has a resolution of 1 ms instead of a sampling rate of 1 μs, as it is also suggested in the previous study [79]. The appropriateness of this timing was also shown in an earlier study conducted at the EVATEG center [85]. In fact, forward voltage data is read at a precision of 1 μV with a 1.4 mV accuracy (for the 2.5 V voltage application) to ensure that the repeatable measurements can be made at steady state condition with higher reliability.

Since junction temperature measurements are not made with any information related to thermal resistance of the heat-flow path, practices that increase the measurement uncertainty such as determining the thermal conductivity of the thermal interface material are also avoided. As a result, the junction temperature, which is the main thermal parameter of interest for LEDs, is measured and presented to the user without any costly process.

3.4 Measurement Approach in EVAtherm

3.4.1 Calibration Measurements

The calibration phase is important in terms of characterizing the junction temperature versus forward voltage behavior of LEDs accurately. This phase of measurements was studied in detail during the development process of our junction temperature measurement device. Measurement steps are described below with the example of default and user settings to explain the measurement procedure clearly:

- In accordance with the default settings; the oven temperature is brought to 40, 60 and 80˚C respectively.
- First, heating is initiated so that the target temperature is 40˚C.
- When 40˚C is reached, the maximum and minimum values of the oven temperature measurements in the last two minutes are taken and checked to see if they are equal to or less than 0.2˚C ($\Delta T \leq 0.2$˚C).
- When $\Delta T \leq 0.2$˚C becomes, the ‘steady state’ indicator is activated, and calibration measurements are started.
- The pulse application (1 mA for 1 ms) is repeated ten times with a 3 second-pause between each application.

For example:

- ❖ Apply 1 mA for 1 ms - measure forward voltage (V_f) - wait 3 s (1)
- ❖ Apply 1 mA for 1 ms - measure forward voltage (V_f) - wait 3 s (2)
- ❖ …
- ❖ Apply 1 mA for 1 ms - measure forward voltage (V_f) (10)

- The average of 10 forward voltage measurements and the oven temperatures during these measurements are determined and matched in the calibration data list if the following requirement is satisfied.
- The maximum and minimum values of all forward voltage measurements are found and the range in the data is determined. If the data range is less than or equal to 0.5 mV ($\Delta V_f \leq 0.5$ mV), the average forward voltage value and the average temperature value are recorded in the calibration data list. If not, the same steps are repeated until $V_f \leq 0.5$ mV is satisfied. This criterion indicates that the pulse application is done in the steady state condition. When the criterion is satisfied, the averaged oven temperature and forward voltage value are matched and added to the calibration list.
- The same steps are performed for 60˚C and 80˚C oven temperatures. A calibration graph is obtained such that the forward voltage (V_f) value is on the y-axis while the oven or junction temperature is on the x-axis. First order linear equation and R^2 value of this graph are also determined and shown in the software.
- R^2 value is checked if it is equal to or greater than 0.985. If this condition is not met, the data point that decreases the R^2 value is detected and the calibration measurement is repeated at that point. When this condition is met, the test measurement stage is started.

3.4.2 Actual Measurements

After the calibration equation of an LED (relationship between V_f and T_j) is established, the test stage is initiated. At this stage, the following measurement steps are followed:

- Before starting the test phase, the temperature inside the oven is brought to the ambient temperature and the chamber temperature is maintained.

- When a driving current of 150 mA is entered by the user for the test phase of the junction temperature measurements, the following steps are performed:
    - ❖ Apply 150 mA for 1 min, drop the current to 1 mA at the instant, apply for 1 ms and measure forward voltage (V_f).
    - ❖ Apply 150 mA for 1 min, drop the current to 1 mA at the instant, apply for 1 ms and measure forward voltage (V_f).
    - ❖ Apply 150 mA for 1 min, drop the current to 1 mA at the instant, apply for 1 ms and measure forward voltage (V_f).
    - ❖ …
- The range of V_f measurements (minimum and maximum) is determined and the last 3 (or more) V_f values are averaged if the last V_f measurements are in the range of 0.5 mV. This ensures that the LED reached steady state condition.
- The averaged forward voltage value is plugged into the calibration equation derived in the previous step and the junction temperature value at the 150-mA driving current is found.

3.5 Conceptual Design of EVAtherm

3.5.1 Design Objectives of a Test Chamber for T_j Measurements

A robust and reliable test chamber (oven) with precise temperature control is required in order to accurately generate calibration data (junction temperature versus forward voltage) for an LED chip. Steady state condition and thermal equilibrium must be achieved for each measurement point. Steady state condition is considered as a temperature change of no more than 0.2°C for minimum of 10 minutes in every temperature readings of the system at this state. The objective was to design a heating and cooling chamber with a high temperature change speed and uniformly distributed temperatures. Operating conditions of the design objective are given in Table 6.

Table 6: Operating conditions for measurement device

Temperature range (°C)	+25°C – 100
Temperature gradient (°C)	±0.5
Steady state condition (°C)	0.2
Min heating and cooling rate (°C/min)	1.5
Cooling liquid	Water

3.5.2 Initial Version of EVAtherm

In the first conceptual design of the device, the test chamber was designed to set certain temperatures in the chamber with an only heating mechanism. Temperature inside the oven chamber was monitored with temperature sensors placed at different regions. PT100 temperature sensors were utilized to take measurements at ten measurement points including internal volume of the chamber and chamber walls (4 sensors for ambient temperature and 6 sensors for wall temperature measurements). Thus, it was aimed to achieve temperature uniformity with temperature data taken from 10 different points in the test chamber.

150 W plate heaters were used to heat the test cabinet and they were placed on the grooves cut at the external side of each wall surface (in total six heaters). Plate heaters were located in the grooves firmly with external wall covers made of sheet metal plates. Heat insulation was also provided to reduce heat losses from the test chamber. The current or voltage to be applied to an LED was provided by a sourcemeter system, which was integrated into a separate section below the test cabinet. The electrical connection between the sourcemeter system and an LED chip was realized by means of the connection apparatus placed in the test cabinet.

For the calibration phase of the measurements, an LED chip is placed at the bottom surface of the oven wall and a uniform temperature distribution is provided around the LED at each calibration step defined by a user in the beginning of the measurements. Heating process is initiated from the internal oven walls with the use of Programmable Logical Controller (PLC) modules that enable the communication between the temperature sensors and the heaters during the process. With temperature data received from temperature sensors, PLC module controls the heaters to set the objective temperature inside the chamber.

The first conceptual design of the oven system was designed to provide enough space for large lighting sources in the internal dimensions of 200 mm x 200 mm x 210 mm. In addition, the material of the oven chamber was selected to be aluminum-6065 material and system electronics were included in a separate compartment behind the test cabinet. Details of the first conceptual design are given in Figure 67.

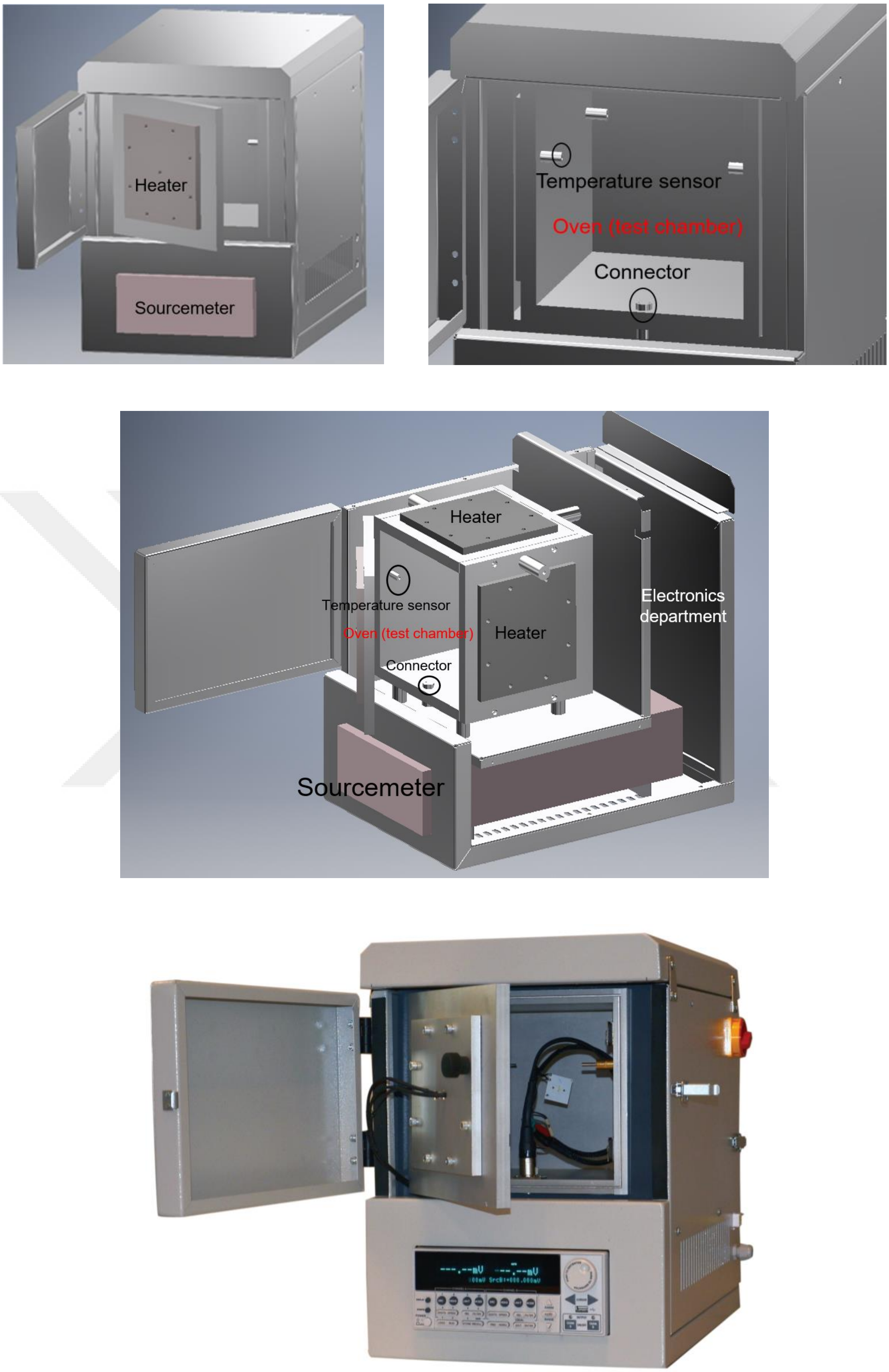

Figure 67: Initial conceptual design and prototype of EVAtherm

3.5.3 Second Version of EVAtherm with Integration of Cooling System

Initial conceptual design and the manufactured prototype of the system was successful in terms of providing constant oven temperatures at the set temperatures. However, measurement time was elongated in transition from the calibration phase to test phase of the measurements due to the lack of an effective cooling system. For this reason, the oven design was improved by including both heating and cooling subsystems in a compact form.

In order to assess the heating and cooling rate of a designed test chamber and the related heat transfer coefficients, an ANSYS Icepak model was created by representing the actual design (see Figure 68).

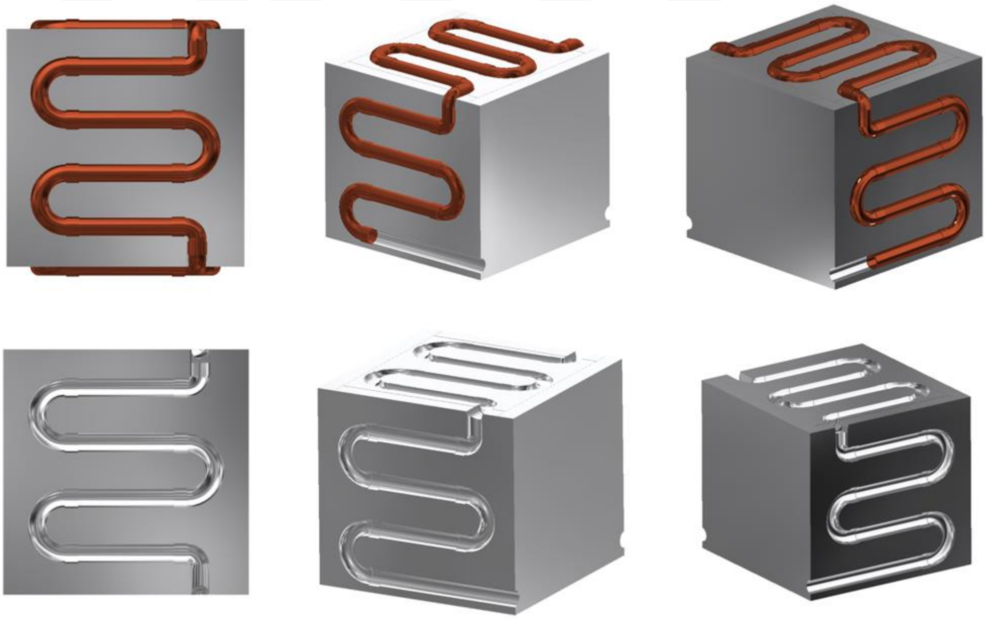

Figure 68: Improved oven design with the inclusion of a cooling subsystem

Aluminum walls, insulation, copper cooling tubes, water and air inside the test chamber were all modeled in ANSYS. In the design, copper tubes were placed in the grooves over three external surfaces to provide necessary cooling from coolant water in the tubes to the hot aluminum walls. While half of the surface areas of the pipes touched on the wall, the other half was covered by the insulation as seen in Figure 69.

Since the intended goal of the simulation was heat transfer analysis instead of analysis of pressure drops in copper tubes, the curved corners of the copper tubes were represented as straight tubes to simplify the model and increase the overall mesh quality.

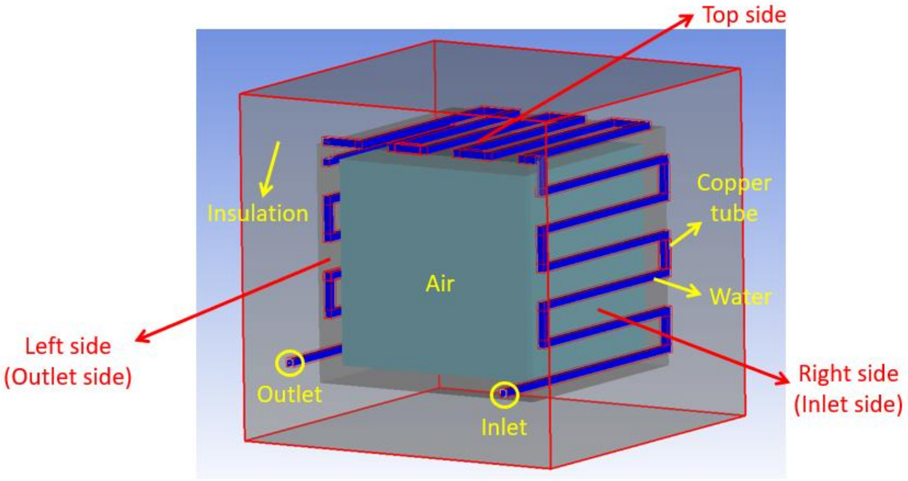

Figure 69: ANSYS Icepak model for the oven system

Transient analysis was made for 5 min with inlet temperature of water at 5^{o}C and inlet velocity of water at 0.3 m/s. The corresponding mass flow rate was determined as 0.0108 kg/s. The flow regime is laminar since the Reynolds number was calculated as 1184. In the model, 15-mm thick oven walls have a material of aluminum 6061 with 154 W/m-K thermal conductivity. Oven walls are insulated with an insulation material that has a thermal conductivity of 0.21 W/m-K and a thickness of 5 cm.

Before running the simulation, the model was meshed as seen in Figure 71. The cooling tubes were meshed finer to increase the accuracy of the results. The number of elements was optimized to get the highest efficiency with a mesh independency analysis of temperature of air after going through a cooling process in the test chamber (see Figure 70). The overall model consisted of 205,080 hex-dominant mesh elements.

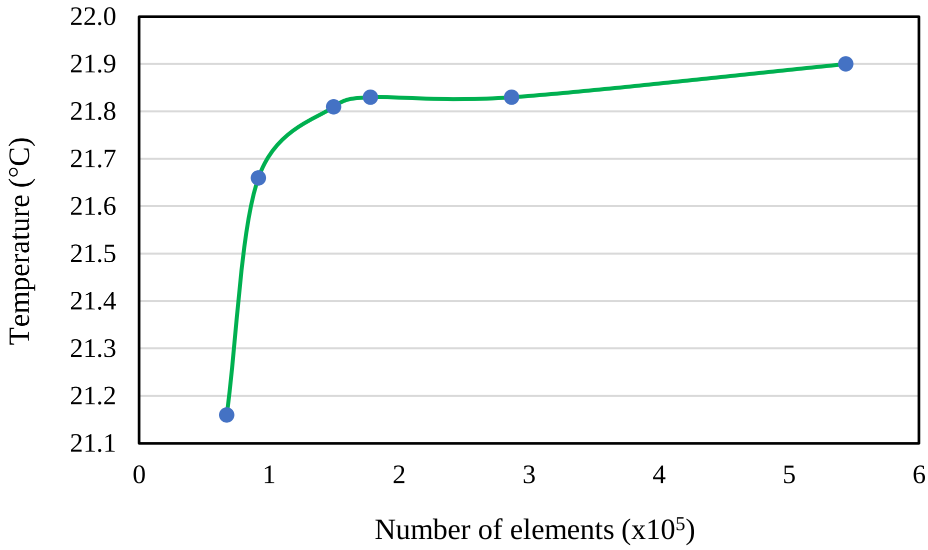

Figure 70: Mesh independency analysis

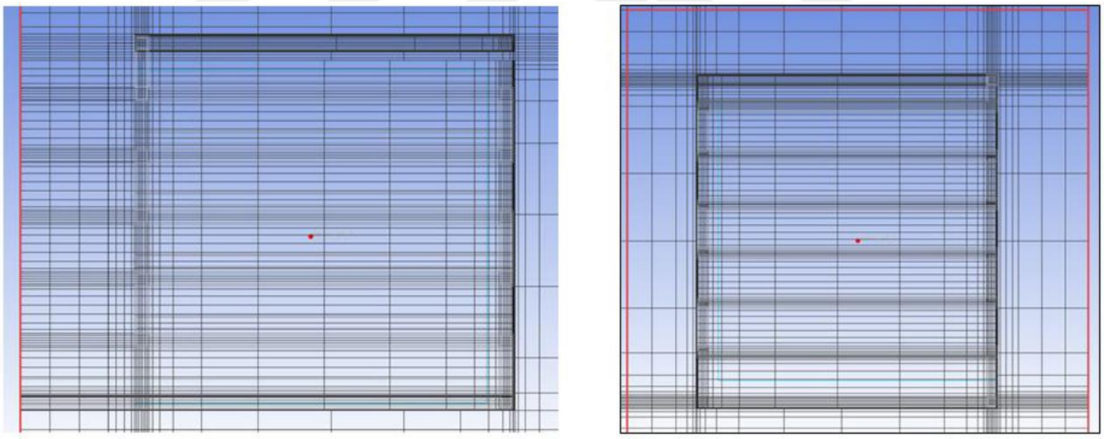

Figure 71: Mesh distribution over the top and side walls of the model

After conducting transient simulations, temperature distribution over the chamber and cooling tubes as well as local heat transfer coefficients along the cooling tubes were obtained. Temperature distribution over the inlet, top side and outlet side of the test chamber after 5 minutes can be seen in Figure 72.

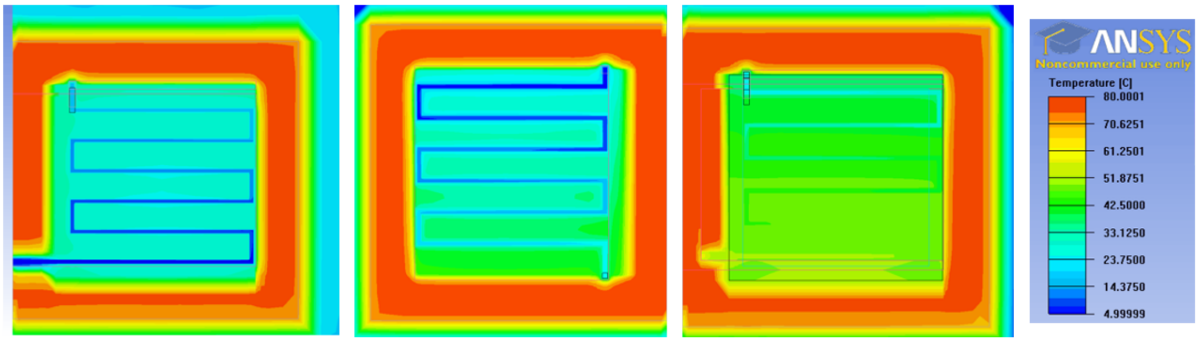

Inlet side Top side Outlet side

Figure 72: Temperature distribution over the inlet, top and outlet side of the chamber after 5 minutes

The local heat transfer coefficient distributions along the tubes of inlet and outlet walls were also obtained to assess the heat transfer at different regions of the oven walls as seen in Figure 73. While the maximum heat transfer coefficient at the inlet wall was 3300 W/K-m^2, it was 450 W/K-m^2 at the outlet wall. Temperature distribution of air in the middle of the chamber was monitored in the simulation and the change in the temperature was found to be by 33.4ºC in 5 minutes from 80ºC to 46.6ºC. Thus, the cooling rate was determined to be 6.7ºC/min. However, the variation of the cooling rate is significant in different regions of the test chamber in 5 minutes simulation conducted with 0.3 m/s inlet velocity. As it is observed, heat transfer coefficients are considerably lower at the outlet side since water at the outlet side gets hotter significantly compared to the inlet side. This can be explained by the low mass flow rate of water and the long heat transfer path over the aluminum walls. Thus, it was understood in this simulation that mass flow rate and the length of the cooling channels need to be adjusted in a proper way that temperature uniformity of air is more easily adjusted in the chamber with a fast cooling rate.

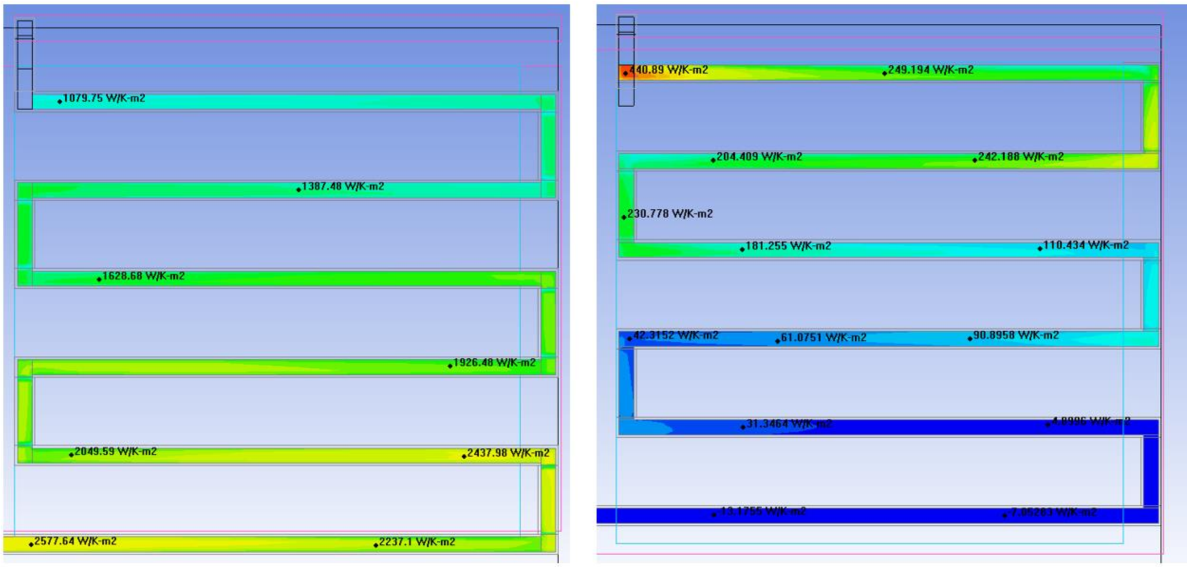

Figure 73: Local heat transfer coefficient distribution over the cooling channels

3.6 Manufacturing of the Second Version of EVAtherm

After conducting transient cooling simulations of the conceptual design of the second version, it was manufactured with the same dimensions of the initial manufactured system that only consists of a heating subsystem. However, certain modifications were made to the oven walls to include the heating and cooling elements together. As it was described previously, copper tubes, 18 mm in diameter, were half-embedded over the external surfaces of three walls of the oven. On the other hand, the grooves in which heaters are inserted at these three walls were cut over the inner surfaces. Thus, heaters at the cooling walls were placed to the inner sides while cooling tubes were located at the external sides of the walls. After point welding of the copper tubes, leakage tests were made, and the cooling tubes were inserted over three external walls of the oven system. Then, the system was insulated to minimize the heat losses. Establishment of the second version of the oven system can be seen in Figure 74.

Figure 74: Manufacturing process of the oven system

After manufacturing of the second design, some heating and cooling experiments were conducted. In heating tests, steady state condition was reached approximately in 40 minutes from 25ºC to 82ºC. In Figure 75, change of ambient temperature is seen with respect to time. Temperatures of all 6 walls during the heating process were also monitored as given in Figure 76.

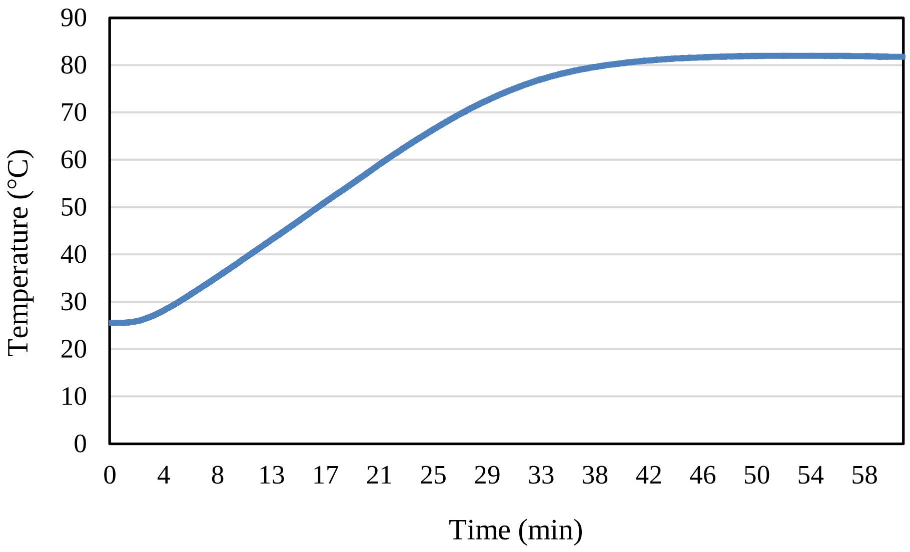

Figure 75: Change in temperature of air in the chamber during the heating process (measured at the middle of the oven chamber)

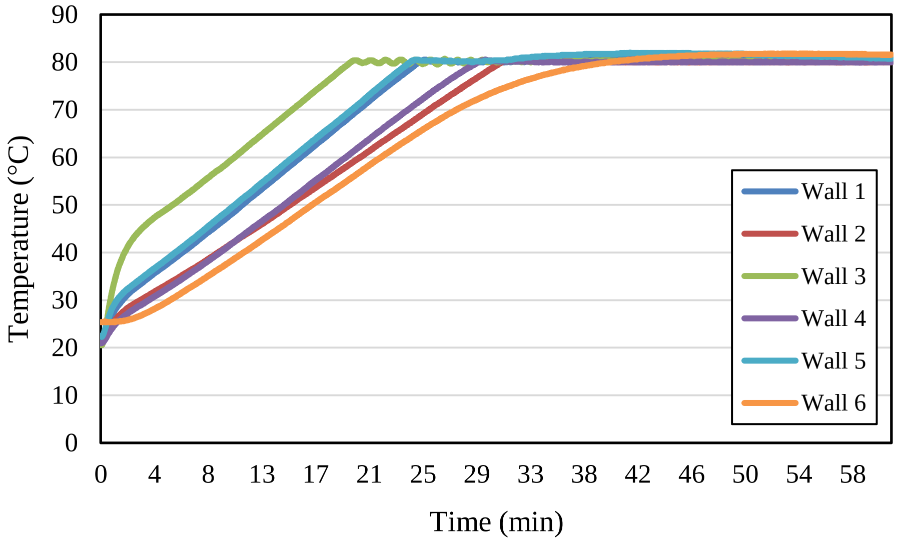

Figure 76: Heating curve of the oven walls

Heating rate of air in the chamber was also monitored with respect to time and the maximum heating rate was achieved as 2 K/min. However, it decreased as the time passes and set temperature is approached.

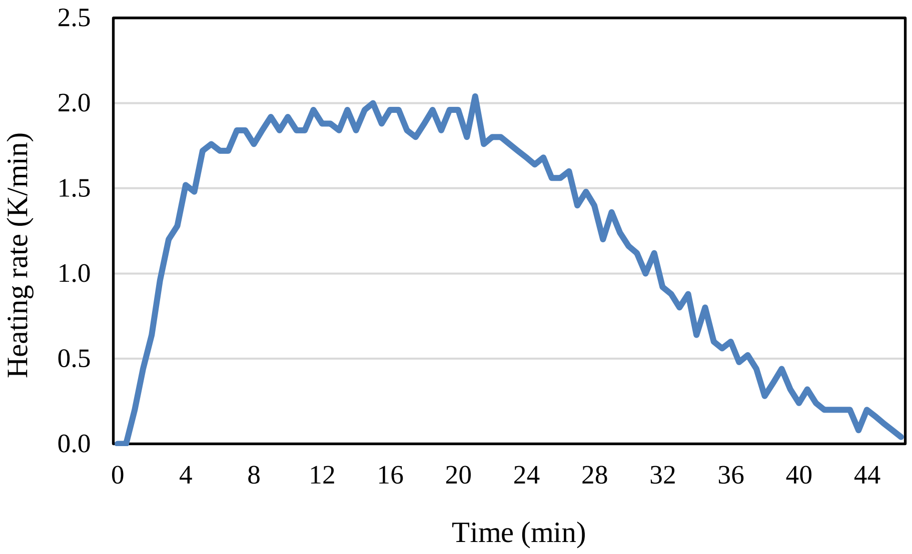

Figure 77: Change in the heating rate of the system with time

Cooling experiments were also done with 72 W thermoelectric (Peltier) modules attached to a 1 L water tank in Figure 78. As it is seen in the figure, water tank, Peltier module, circulation pump and system electronics were all placed at the back side of the oven system to supply cooling water to the oven system. In cooling experiments, it was aimed to analyze the cooling performance of the system with known cooling parameters. The water tank was very well insulated except for the interface region where the Peltier + Heat sink + Fan system touches on the bottom surface of the water tank. Heat sink and fan integration to the Peltier component was needed to dissipate the generated heat at the hot side of the Peltier module and keep the temperature of the cold side low enough.

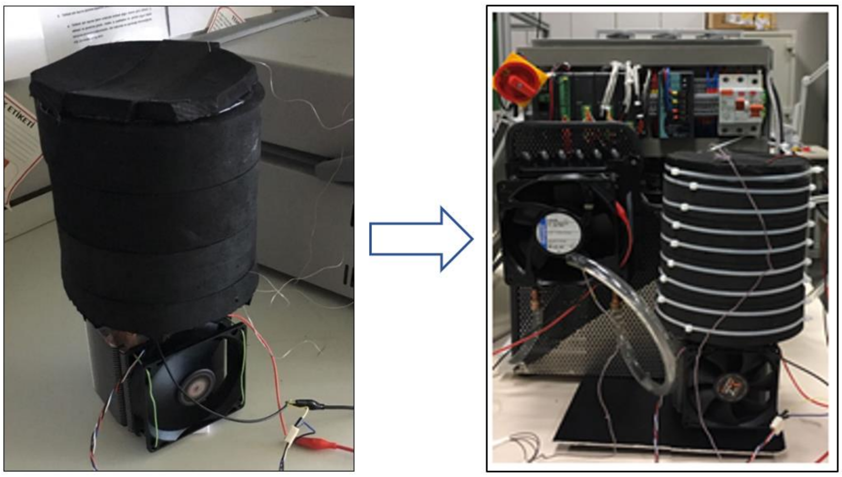

Figure 78: A cooling module with a thermoelectric module and heat sink and fan integration

Temperature of water in the water tank was lowered to 15°C with the use of a Peltier module as seen in Figure 78. Temperature of water provided to the oven system was monitored with a thermocouple attached at the exit of the pump while the pump was located inside at the bottom of the water tank. Water at 15°C was supplied to the oven at 80°C and the cooling of the air in the test chamber was monitored. As seen in Figure 79, after circulating the oven pipes and filling up the water tank again, water could not maintain its initial temperature due to the cooling power provided by the Peltier modules was not enough to keep it at 15°C. In fact, temperature of water was immediately raised to the level around 35°C and kept rising to nearly 40°C. Later, the Peltier power achieved to cool the provided water down to ambient temperature levels; however, it took more than one hour. Although it was understood that the Peltier module was not successful in terms of providing water at a constant desired temperature, the experimental study was useful in terms of keeping track of the cooling rate of the manufactured system with known inlet temperatures of water.

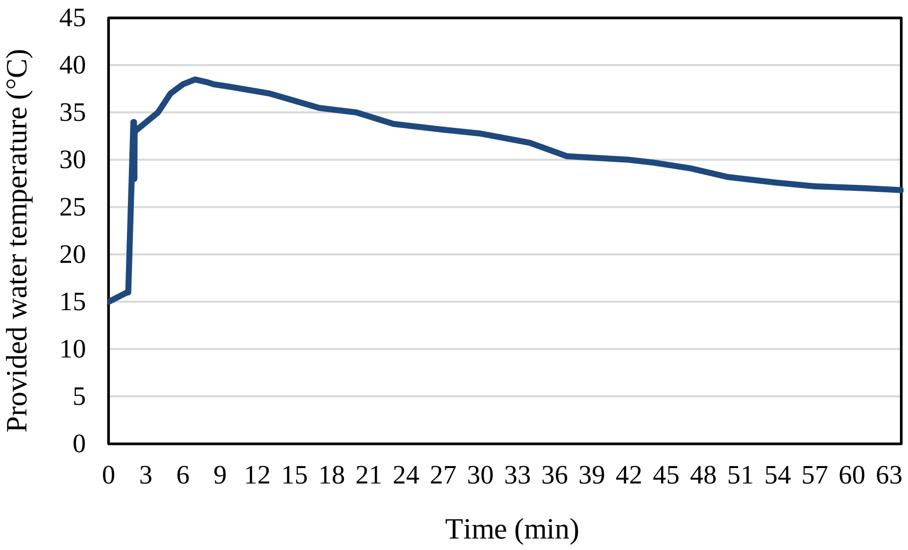

Figure 79: Change in inlet temperature of cooling liquid (water) with time

The cooling test was conducted from the air temperature of 82ºC to 34ºC in approximately 70 minutes as seen in Figure 80. The cooling rate was also monitored at 0.5-min intervals in Figure 81. Due to the instability in the temperature of the provided water and decreasing difference between ambient and water temperatures, the cooling rate became lower as time passes. However, the maximum cooling rate was determined to be almost 2.5 K/min when 15°C water was provided to the system. 1 K/min, the project's minimum acceptable cooling rate, was obtained with inlet temperature of water around 37°C when the air temperature was 60°C. As a result, 65 °C difference between air and water temperatures provided 2.5 K/min cooling rate, while temperature difference of 23°C resulted in 1 K/min cooling rate.

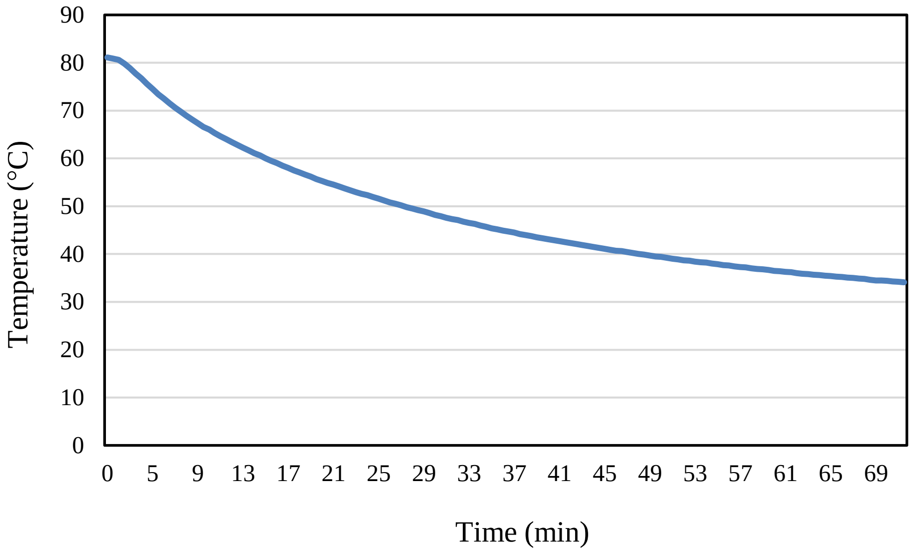

Figure 80: Change in temperature of air in the chamber with time during the cooling process (measured at the middle of the oven chamber)

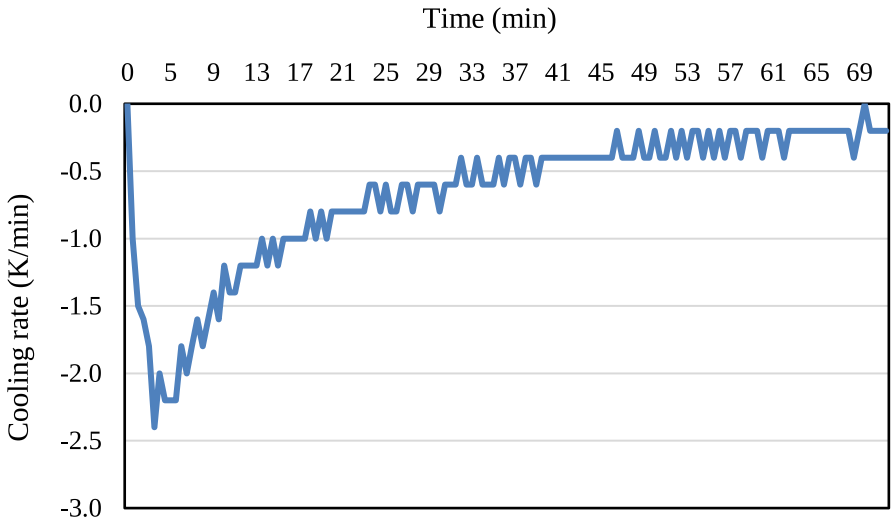

Figure 81: Change in the cooling rate of the system with time

3.6.1 Design and Analysis of Cooling System Units

With the initial ANSYS Icepak analysis, heat transfer performance of an oven system was examined with certain design parameters and it was understood that a cooling rate as much as 6.7ºC/min could be obtained with the provision of 5°C water temperature. Then, the conceptual design was manufactured as a second version including the heating and cooling subsystems. Cooling experiments were conducted with different inlet water temperatures (minimum 15°C) and the highest cooling rate of air in the chamber was nearly 2.5 K/min.

During the experiments, thermoelectric modules were found to be insufficient to maintain water temperature well below ambient conditions. Use of a chiller system as a cooling unit was evaluated; however, it was not utilized since a more compact and closed cycle system was aimed as a measurement system. Therefore, air cooled heat exchanger was preferred as a cooler unit that can be integrated into a closed cycle. However, in this cooling system, the coldest water temperature was limited to the initial water temperature at room conditions. In fact, the air-cooled heat exchanger removes the excess heat, reducing the temperature of the heated water to the initial temperature value.

After determining the cooler of the system, other required components of the system such as water pump, valves, pipes etc. were also identified. Design of the system with necessary connections are described in Figure 82.

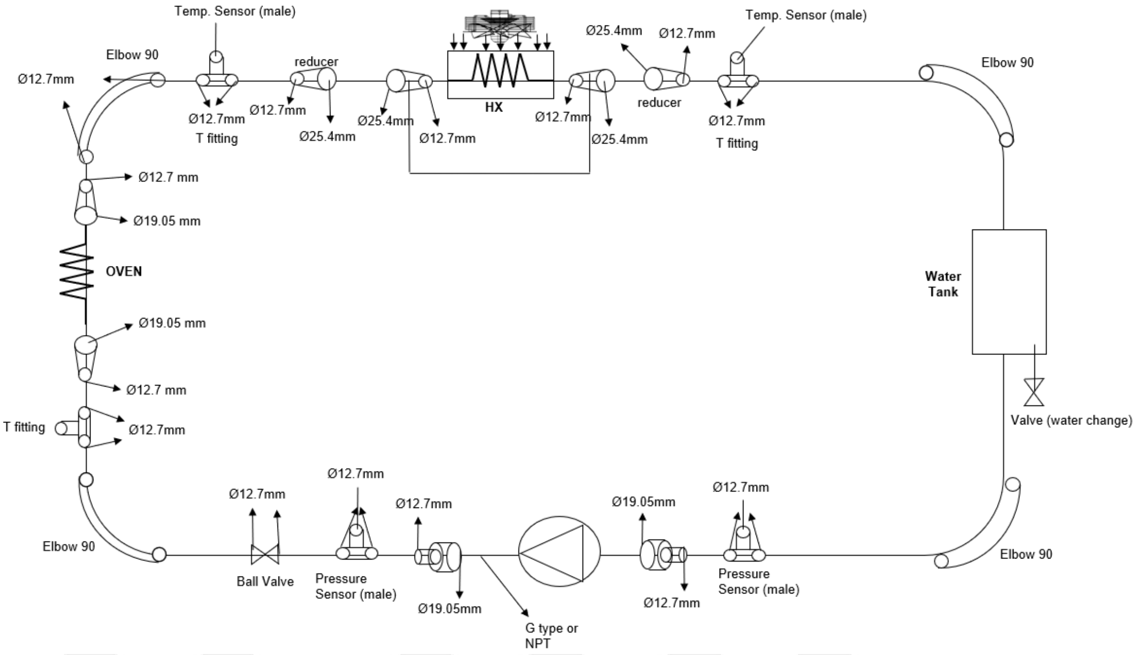

Figure 82: System connections of the measurement unit

The main components of the overall system include an oven system (test chamber), an air-cooled heat exchanger, a water tank and a pump. It is a closed system with necessary cooling, piping and sensor elements to maintain the ambient temperature of the test chamber at desired levels. If it is required to cool the test chamber down to a set temperature, coolant (water) stored in the water tank is pumped to the oven system with a pumping system; then, the heated water in the oven system enters the heat exchanger system. Cooled water is obtained at the outlet of the heat exchanger and transferred to the water tank. If heating is required to set the temperature of the test chamber to a certain level, heaters embedded at the walls of the chamber start running to set the desired temperature.

To determine the cooling capacity and the required heat transfer area of the air-cooled heat exchanger system, analytical study was conducted with an Engineering Equation Solver (EES) program. System dimensions, operating conditions and cooling targets are defined in the EES program as shown in Appendix B.

For the analytical calculation of the required cooling performance, a cooling rate objective has been set as 5 K/min. Accordingly, total dissipated thermal energy was calculated considering the temperature of air in the test chamber is reduced from 80°C to 25°C. As a division of total dissipated thermal energy with the cooling rate objective, cooling time was found. Then, the total dissipated thermal energy was divided to the cooling time and the required cooling performance was determined.

In order to find the required heat exchanger surface area, logarithmic mean temperature difference was calculated with certain assumptions on total heat transfer coefficient, temperature of water at inlet and outlet of the heat exchanger and temperature of air at inlet and outlet of the fan. Reasonable assumptions were made based on experimental observations given in Section 3.6 to have an initial idea before manufacturing the heat exchanger system and other components.

As a result of the analysis, a cooling requirement of 1.1 kW and 5.741 m^2 heat transfer surface area has been identified for the design of heat exchanger as it is seen in Appendix B. A 2.3 kW air cooled heat exchanger with 5.9 m^2 heat transfer surface area and a circulation pump capable of providing 13.2 L/min flow rate were selected to ensure that the sufficient cooling is provided considering the uncertainties and deviations in results due to the assumptions utilized in the analysis.

3.7 Design, Analysis and Manufacturing of the Third Version

After prototype manufacturing and performance tests of the conceptual and initial designs, a significant understanding has been gained with heating and cooling tests of the test chamber. Considering the objective of the project as a single chip junction temperature measurement, further study continued with improving the latest design based on minimizing the size of system components and measurement time of the system. With the previous analyses and lessons learned, some modifications have been made in the system design and the performance of the system was increased.

In the previous designs of the test chamber, dimensions of the system were larger than needed and this was increasing the heating and cooling performance requirements as well as the size of heating and cooling components. In addition, cooling pipes were adding extra thermal resistance to the heat removal path especially if the pipe to wall contact is not smooth enough. On the other hand, providing smooth and leakage-free contact was bringing difficulties and increasing manufacturing costs. While liquid seal was successful in attaching the pipes each other, it led to leakage at some points over heating and cooling cycles. Although point welding of the pipes prevented leakage at all points, it added additional thickness at the connection points leading to contact resistances or manufacturing difficulties in cutting grooves over the wall surfaces. Moreover, embedding only the half surface area of pipes in the oven walls was not maximizing heat transfer and plate resistances embedded in the oven walls were taking a large place but providing limited heating power. These were one of the major problems behind designing a compact test chamber including heating and cooling subsystems.

To tackle all these issues, the test chamber has been re-designed with major improvements. First of all, plate resistances were replaced with cartridge resistances at 6 mm in diameter and 100 mm in length. All heaters were located in the bottom wall of the oven to benefit from the effect of natural convection currents from bottom to upper positions and provide faster and more uniform temperature distribution in the chamber. The number of heaters required to heat the test chamber at the desired heating rates was decided based on the experiments conducted on a test chamber with minimized internal volume of 14 cm x 13 cm x 13 cm. Internal volume of the test chamber was reduced in dimensions to the smallest possible volume that could be suitable for junction temperature measurements of a single LED chip. In addition, copper tubes were removed from the design and cooling channels at 6 mm in diameter were created with drilled holes extending from one end to another end of the cooling walls. Cooling channels were connected each other from the external surface of the walls with leakage free and thermally durable connectors. This approach greatly simplified the design of the cooling channels by reducing the manufacturing costs. At the same time, liquid coolant (water) was able to remove the excessive heat from the hot walls directly without any additional thermal resistance. The previous approach that requires the placement of copper tubes over the wall grooves was limiting the overall heat transfer surface area between water, copper tubes and aluminum wall due to the large bending radius of tubes even at the smallest diameter of the tube. New design approach gave much more flexibility to adjust the distance between cooling channels and increase the total heat transfer surface area at the water-wall interface. Drilled cooling channels and connection elements can be seen in Figure 83.

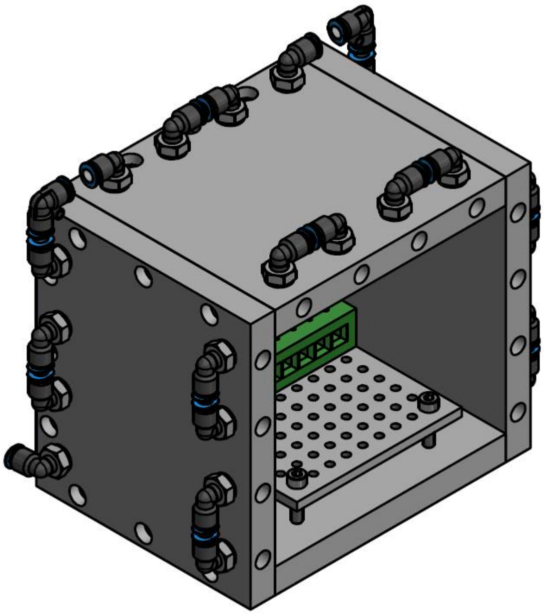

Figure 83: Drilled cooling channels and connection elements

Steady state condition in the test chamber is set with the use of a PLC module that runs the heaters based on temperature data received by temperature sensors located on various places in the oven. While three K-type temperature sensors were placed in the bottom wall, another three were located on the ceiling wall of the chamber. In addition, two T type thermocouples were utilized to measure temperature in the test chamber. Thus, thermal condition of the oven system was monitored to provide uniformly distributed temperature profile at steady state condition during the junction temperature tests. For the proper placement of LEDs in the oven, an LED mounting table was formed with multiple electrical connectors and the extension cables were properly removed from the back wall of the oven system. The oven system is also insulated with a 20 mm thick insulating material (stone wool) that is durable in a temperature range between -50°C and 600°C. The new system concept is shown in Figure 84.

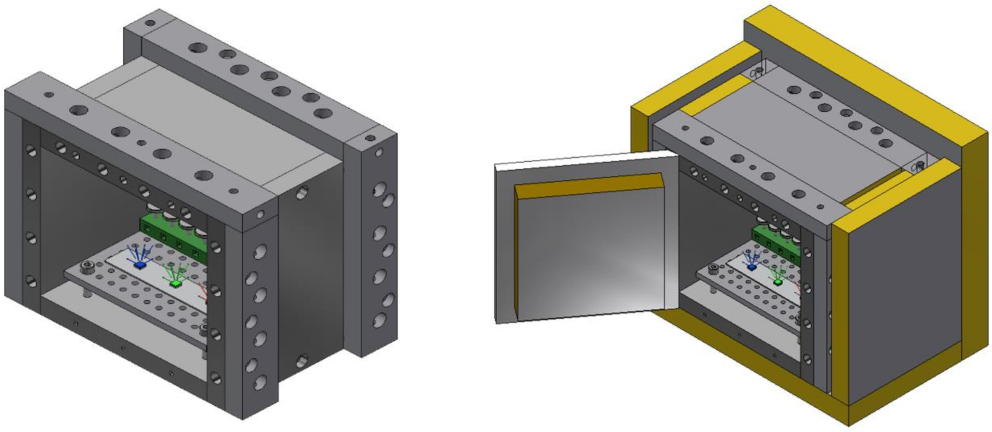

Figure 84: The improved design concept of a compact oven system

An Engineering Equation Solver (EES) program (see Appendix C) was created for the new design approach and the impact of diameter of coolant channels, total channel length and volumetric flow rate on pressure drop and required pumping power was investigated. An initial analytical calculation with EES was done considering the real operating conditions with some reasonable assumptions. One of those assumptions include a temperature difference of 5°C between inlet and outlet water (coolant) temperatures and it is decided based on computational simulations conducted for the last version of the design.

In order to investigate the impact of temperature difference on pressure drop and pumping power, a parametric table has been created and interpreted with a graph as seen in Figure 85. The analysis shows that when the assumption of temperature difference is shifted from 5°C to 50°C, the change in pressure drop becomes 0.0135 Bar while the variation in pumping power becomes 0.095 W. This shows that the assumption of temperature difference of inlet and outlet water does not significantly affect pressure drop and pumping power calculations.

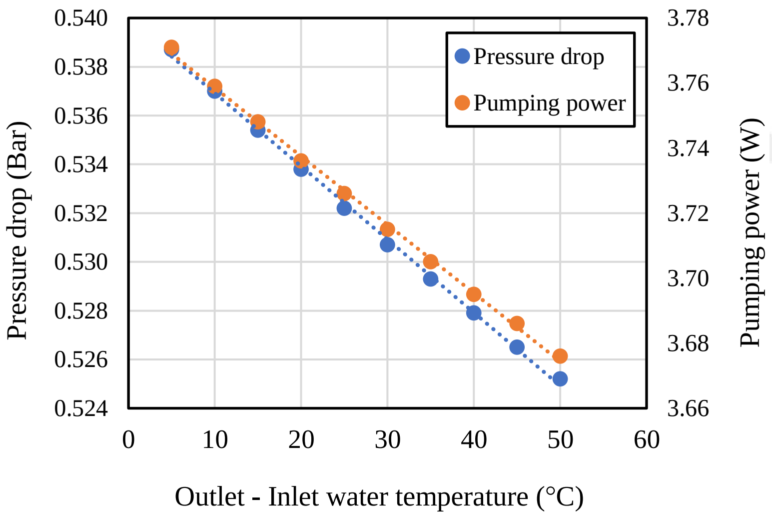

Figure 85: The impact of temperature difference (between outlet and inlet water) on pressure drop and pumping power

The initial calculation was made with a coolant channel diameter of 6 mm, total coolant path length of 1.32 m and volumetric flow rate of 4.2 L/min. The volumetric flow rate utilized in analytical calculations was selected based on experimental measurements during the initial tests of the test chamber in manufacturing phase. In addition, surface roughness of the drilled coolant channels was assumed to be 3 x 10^{-5}, which is the typical surface roughness value of an aluminum drawn/pressed tube. Furthermore, mean velocity of water was calculated and utilized in pressure drop calculations in every region of the oven system. However, the velocity profile may significantly change along the coolant path. Thus, although reasonable assumptions were made, they may cause to significant variations between analytical and experimental results. However, the analysis was useful to understand how various variables of the cooling system affect pressure drop and pumping power requirements.

According to the initial calculation of the designed test chamber, pressure drop of 0.54 Bar and pumping requirement of 3.8 W were determined for the maintenance of water flow along the coolant channels. Analysis demonstrated that diameter of coolant channels, total coolant channel length and volumetric flow rate critically affect the results. Thus, pressure drop and power requirements were also examined for other cases of these variables in Figure 86, Figure 87 and Figure 88. (Detailed results of the analytical calculations are given in Tables in the Appendix C.)

First, the effect of diameter of coolant channels on pressure drop and pumping power was significant especially if channel diameters are designed smaller than 6 mm. In the analysis, total cooling channel length and volumetric flow rate of coolant water were kept constant as 1.32 m and 4.2 L/min respectively. As seen in Figure 86, pressure drops at higher diameters show much lower and closer results compared to the results of diameters below 6 mm. In transition from 6.1 mm to 5 mm, pressure drop increases by more than two times and 5.1 W more pumping power is needed in comparison with the 3.5 W pumping power requirement at 6 mm.

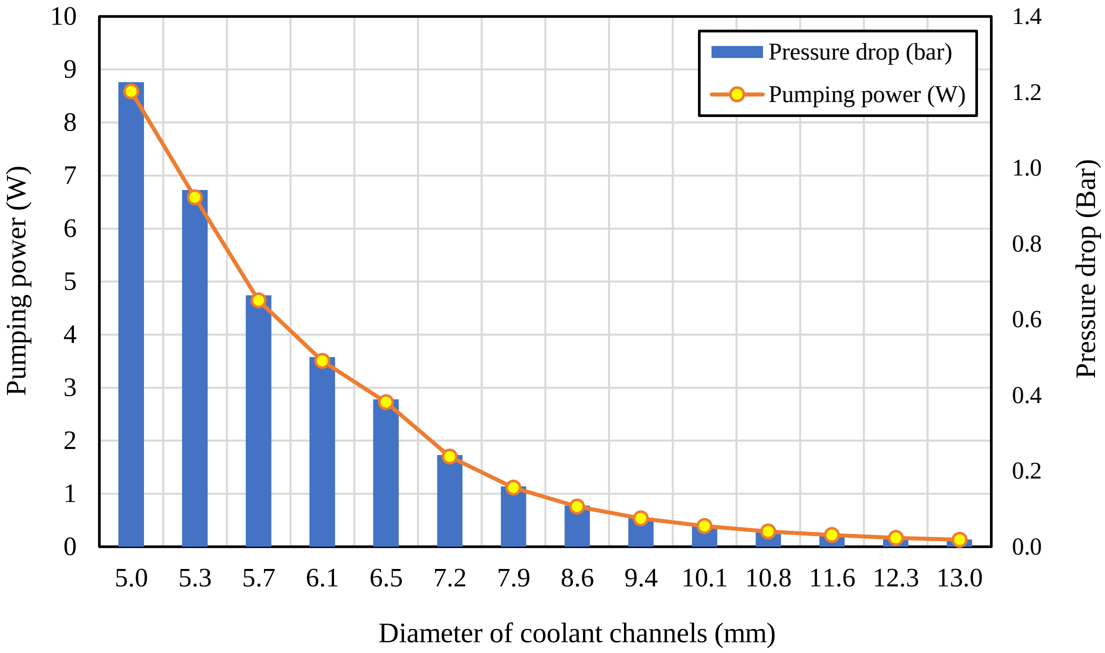

Figure 86: The impact of coolant channel diameter on pressure drop and pumping power

In Figure 87, the relationship between channel length and pressure drop as well as pumping power shows a linear trend. 0.18 Bar pressure drop is observed at each 1 m channel length, while 1.2 W more pumping power is needed over the same length interval.

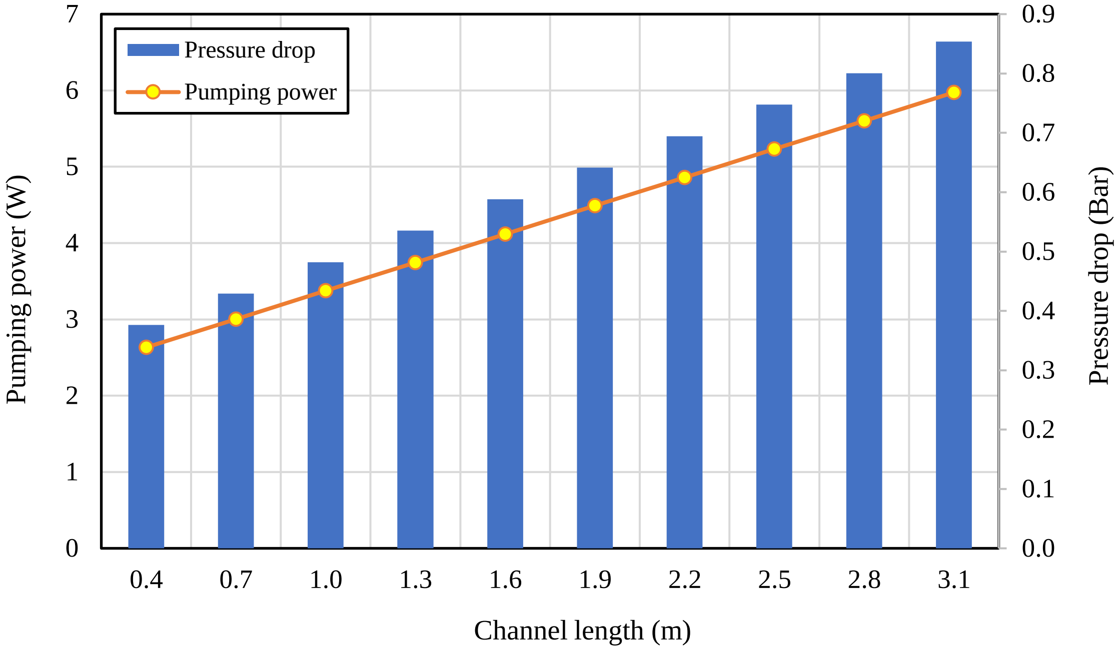

Figure 87: The impact of total channel length on pressure drop and pumping power

Another significant finding is obtained when the impact of volumetric flow rate of the coolant on pressure drop and pumping power requirement is examined at a cooling channel diameter of 6 mm and total cooling channel length of 1.32 m. As seen in Figure **88**, pressure drop and the needed pumping power are increasing exponentially in a range of 0.5 to 9.5 liter per minute (L/min) volumetric flow rates. Thus, it is critical to assess the heat transfer performance and pumping power requirement together in order to avoid too large pumping costs.

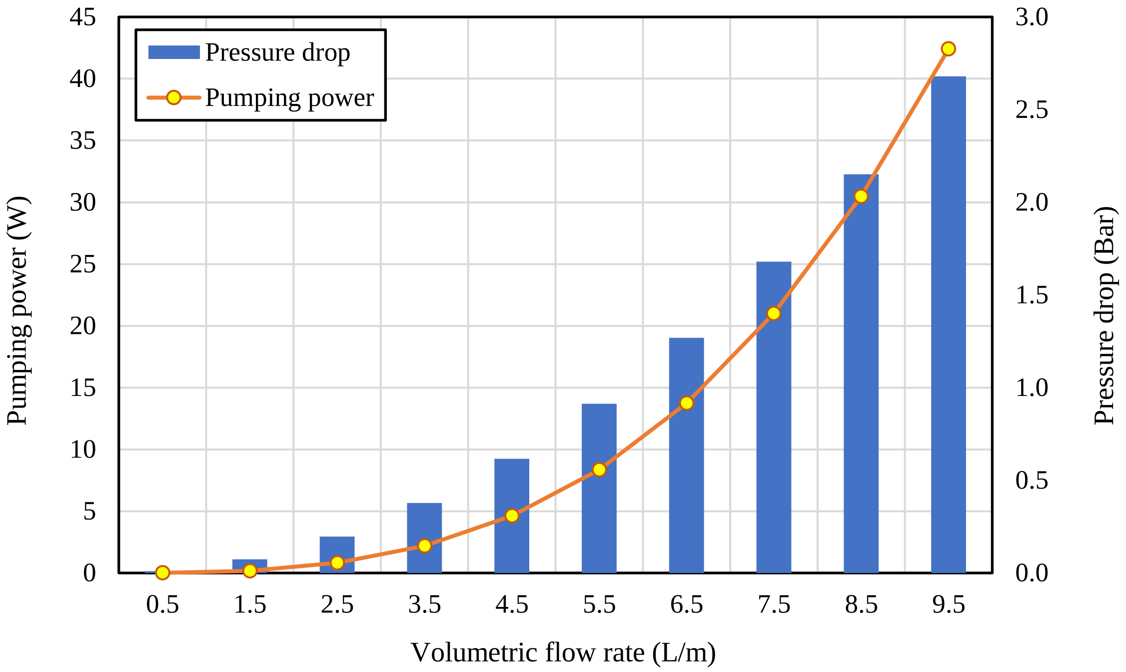

Figure 88: The impact of volumetric flow rate on pressure drop and pumping power

Transient thermal analysis was made to determine design parameters that result in a desired heating and cooling rate of the test chamber. Thus, the oven model was created in ANSYS Icepak [77] (see Figure 89) including heating and cooling subsystems and the changes of air temperature in the oven and water in the drilled holes were observed. It was aimed to achieve over 1.5°C/min heating and cooling rate of the air. After the analysis, it was decided that cooling channel diameter of 6 mm, three 200 W capacity heaters, the provision of 17°C inlet water, 14x13x13 cm^3 internal volume chamber and 15 mm thickness insulation layer satisfy the heating and cooling rates over 1.5°C/min.

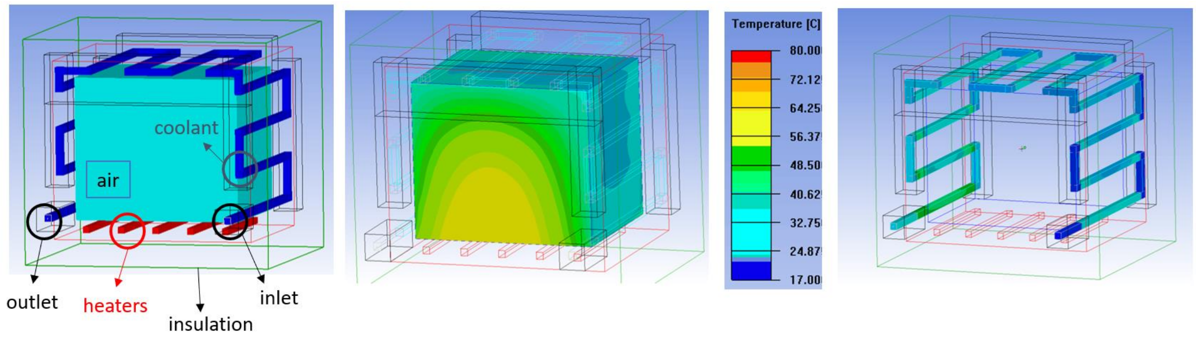

(a) (b) (c)

Figure 89: ANSYS Icepak model of the oven system (a), Temperature distribution of air inside the oven system during transient simulations (b), Temperature distribution of cooling liquid inside the drilled holes in the oven walls (c)

Considering the analytical and numerical analysis as well as manufacturing ease, system specifications, assembly components and connections have been determined to yield the desired heating and cooling rates. A closed system cycle similar to the previous design version has been created with the main components of an oven system, heat exchanger, water tank, and circulation pump. As seen in Figure 90, temperature sensors are located at the inlet and outlet section of the oven while the pressure sensors are placed at the inlet and outlet section of the circulation pump. Different components of the system are connected with thermoset hoses.

After manufacturing the system, temperature and pressure measurements have been made to evaluate the performance of the system. The oven system was manufactured to be durable at the maximum temperature of 100°C and steady state tests have shown ±0.2°C temperature sensitivity at different regions of the oven system at steady state condition. In addition, pressure measurements have been performed from inlet and outlet section of the oven wall to measure the pressure drop in the system and 2 Bar (3 Bar inlet pressure to 1 Bar outlet pressure) was measured in the system.

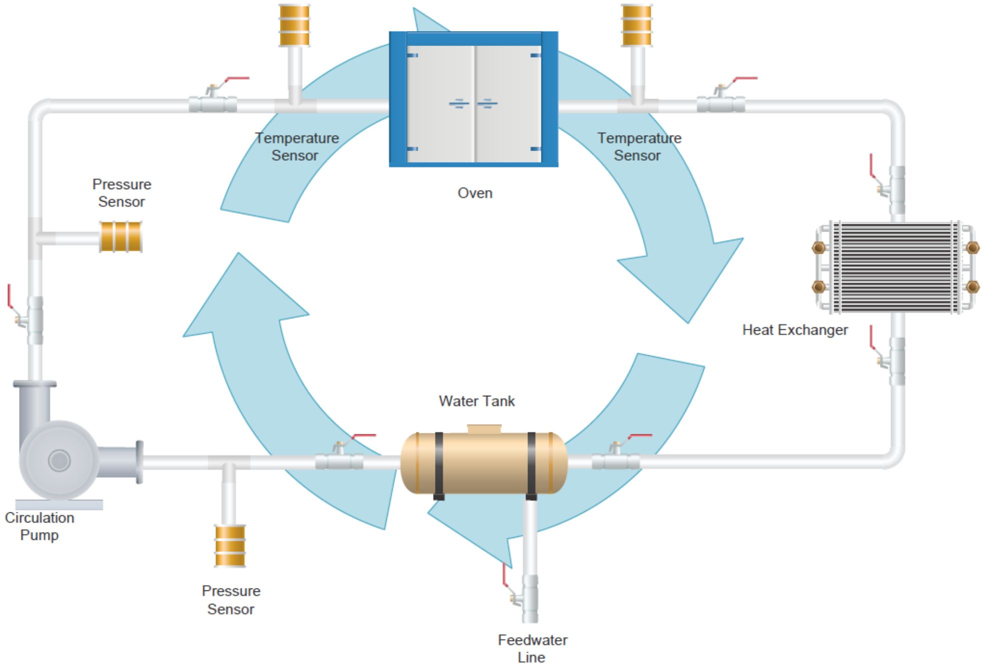

Figure 90: System connections and the cooling subsystem of the measurement device

Temperature at the middle of the internal air volume of the system was monitored with respect to time for both heating and cooling processes in a range of 24.4 to 100°C. While 4.5°C/min heating rate is achieved in this range, a larger rate of cooling (7.2°C/min) was obtained in the same range.

Cooling behavior of the system was also predicted with the CFD study and the results were compared with the experimental values. In the manufactured design, the coolant channels were connected outside of the oven walls with proper connectors while those connectors, in the CFD model, were represented at the same plane with the coolant channels in order to simplify the numerical analysis. On the other hand, other geometrical details including the total length of channels, diameter of channels and the volume of the oven etc. were modeled with the same dimensions to have a representative heat transfer analysis. Due to the difference in the cooling path model, velocity profiles in the experiment and CFD model was expected to be different especially at the connector sides. Accordingly, a number of inlet water velocity values were set in numerical simulations and the case that gives approximate results with experimental data was investigated. The simulation case with inlet water velocity of 0.7 m/s was successful in terms of predicting the changes in air temperature with respect to time as seen in Figure 91. While the results showed a closer behavior in a range from 70°C to 40°C, variations were more significant towards ambient temperature level.

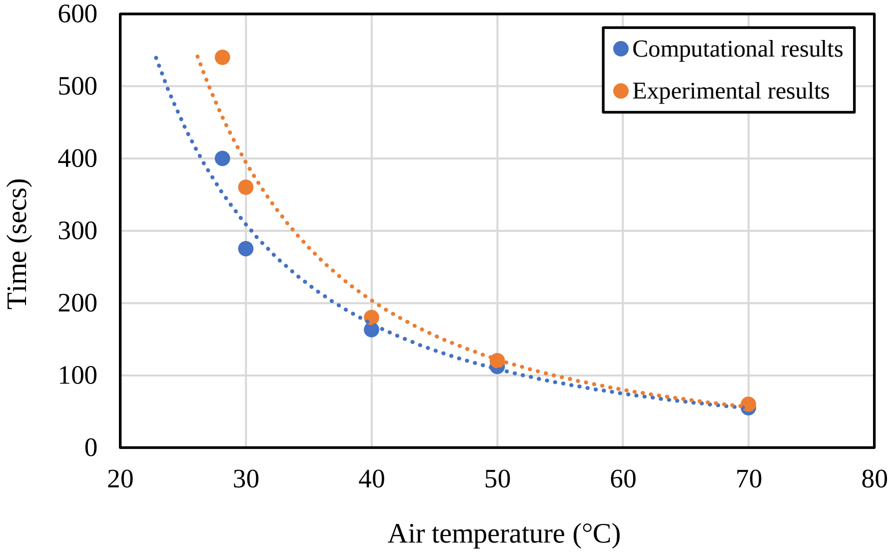

Figure 91: Comparison of computational and experimental results during transient test

After conducting computational and experimental studies, it was understood that a volumetric flow rate of 4 L/min provides fast cooling rate of air in the system and a circulation pump that maintains the flow against a pressure drop of 2 Bar at the specified flow rate can be selected. Then, according to the operating pressure-flow rate, the nominal flow rate of the circulation pump was determined. A circulation pump capable of providing a flow rate of 10 L/min was selected.

Cooling is done with the help of a fan driven plate type heat exchanger, of which the plate distance and dimensions are determined from the required cooling capacity of the chamber to operate with a rate of 5°C/min. As a result, the cooling capacity and heat transfer area of the heat exchanger were chosen to be 1.5 kW and 6 m^2 respectively.

With the specifications given above, the oven system and the associated cooling elements of the system have been manufactured and assembled as seen in Figure 92. In the figure, inlet and outlet connections of the oven system, temperature sensor placements over the ceiling wall, a 20 L water tank-heat exchanger connection as well as cartridge heaters used to heat the oven system can be seen clearly.

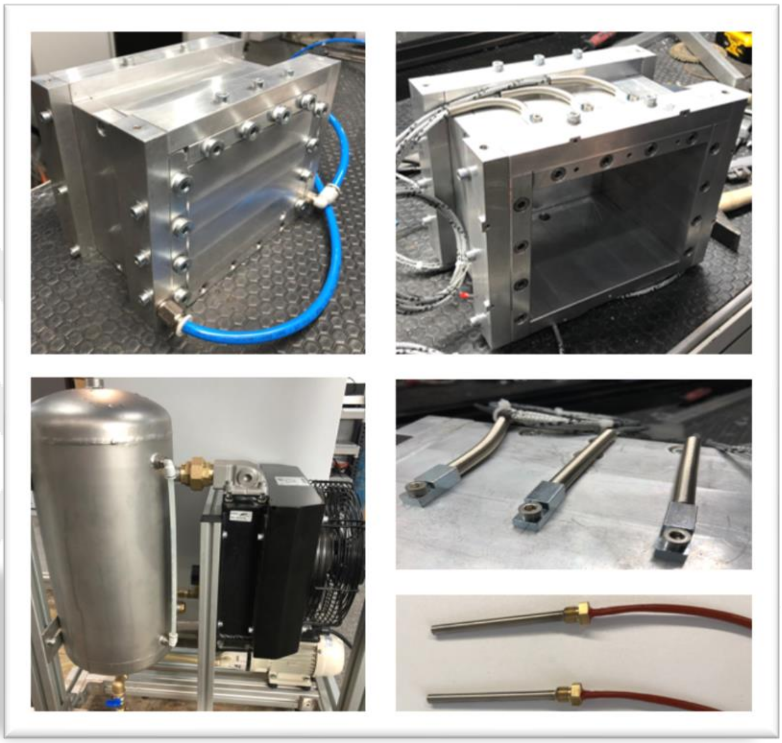

Figure 92: Oven system, water tank, heat exchanger, temperature sensors and heaters of the third version of EVAtherm

After manufacturing, assemblying and testing of the measurement system, sourcemeter integration have also been made and a measurement software was created based on the measurement methodology defined in Section 3.4. Depending on the user settings, the measurement system has been operated and junction temperatures of various LEDs have been measured and validated at different driving currents. The complete system can be seen in Figure 93.

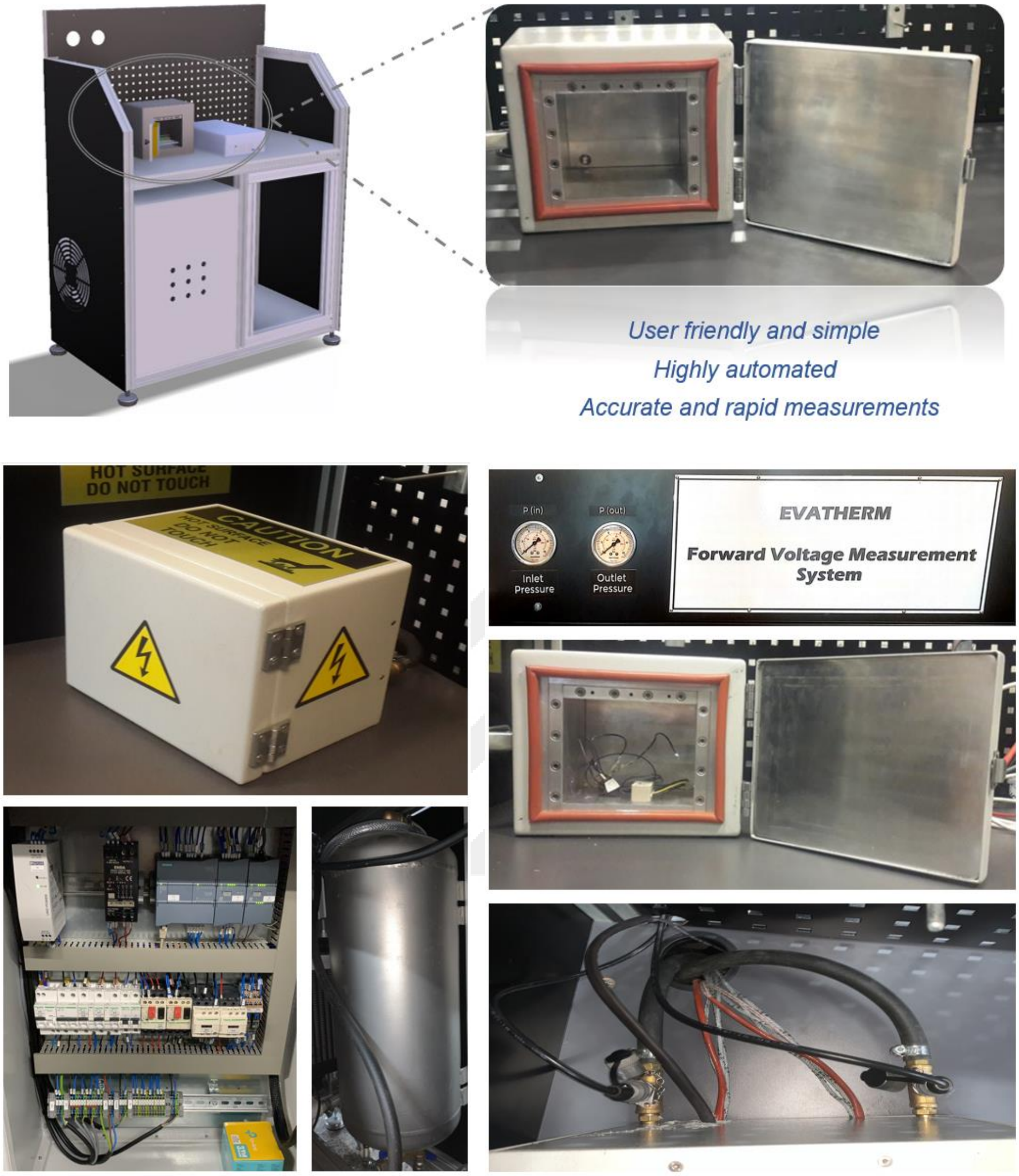

Figure 93: Components and assembled version of the junction temperature measurement system (EVAtherm)

3.8 Junction Temperature Measurements in EVAtherm

Junction temperature measurements of single high-power LEDs were conducted in the second and final version of EVAtherm with repeatability and comparison tests to increase the reliability of the results.

3.8.1 Repeatability Tests in the Second Version of EVAtherm

Junction temperature measurements of a single blue LED were conducted two times at different ambient conditions from 30°C to 80°C with 10°C increments and driving currents (300, 400 and 500 mA) to observe the repeatability of tests. The LED system was operated at a steady state condition, which is defined as the change in board temperature by 0.1°C for a 15 minutes time period in this study. Results are tabulated in the Table 7 and plotted in Figure 94 with various ambient temperature and application current conditions. As a result, the results have shown a good agreement with a maximum variation of 1.6°C between two measurements.

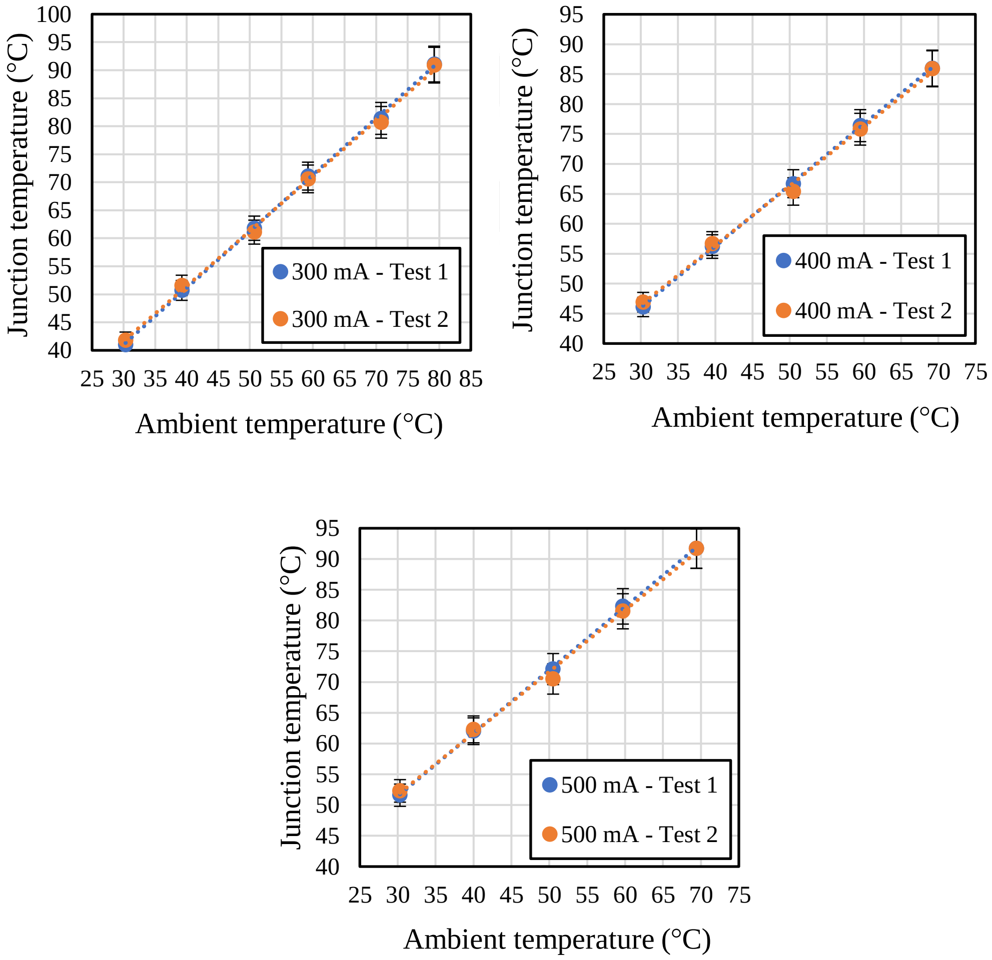

Figure 94: Evaluation of repeatability of results with a single blue LED driven with 300, 400 and 500 mA operating currents at different ambient temperatures

Table 7: Repeatability tests of a single blue LED in the second version of EVAtherm

Driving current (mA)	T_{amb} (°C)	Test 1	Test 2
		T_j (°C)	T_j (°C)
300	30.3	41.0	41.8
400	30.3	46.1	46.9
500	30.3	51.6	52.3
300	39.2	50.7	51.6
400	39.6	56.2	56.7
500	40.0	62.0	62.3
300	50.7	61.8	61.1
400	50.5	66.7	65.4
500	50.5	72.1	70.5
300	59.2	71.1	70.6
400	59.5	76.4	75.8
500	59.7	82.3	81.5
300	70.8	81.4	80.7
400	69.2	86.0	85.9
500	69.4	91.7	91.7
300	79.2	91.1	90.9

3.8.2 Measurements in the Final Version of EVAtherm

3.8.2.1 Repeatability Tests

In the final measurement system, the tests of high-power blue and white LEDs were carried out for two different tests at the same ambient conditions (25.5°C ambient temperature and 130x130x20 mm aluminum block), and the differences between the results were examined. As shown in Table 8 and Figure 95, the maximum difference was determined to be 0.7°C as a result of the tests performed at 3 different currents.

Table 8: Repeatability tests of the high-power blue LED in the final measurement system

Current (mA)	Blue LED – Junction temperatures (°C)	
	Test 1	Test 2
200	35.1	35.8
350	41.1	41.1
500	47.7	48.2

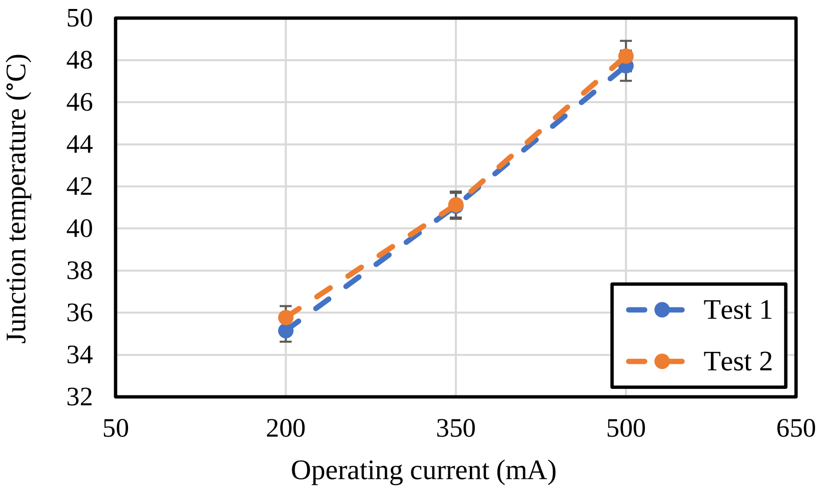

Figure 95: Repeatability tests of the high-power blue LED in the final measurement system

Repeatability tests were also performed for high power white LEDs in the same ambient conditions (on an aluminum block of 130x130x20 mm at 25.5°C ambient temperature). The maximum difference in the results was 0.6°C (Table 9 and Figure 96).

Table 9: Repeatability tests of the high-power white LED

in the final measurement system

Current (mA)	White LED – Junction temperatures (°C)	
	Test 1	Test 2
200	27.4	28.0
350	33.5	34.0
500	40.5	40.6

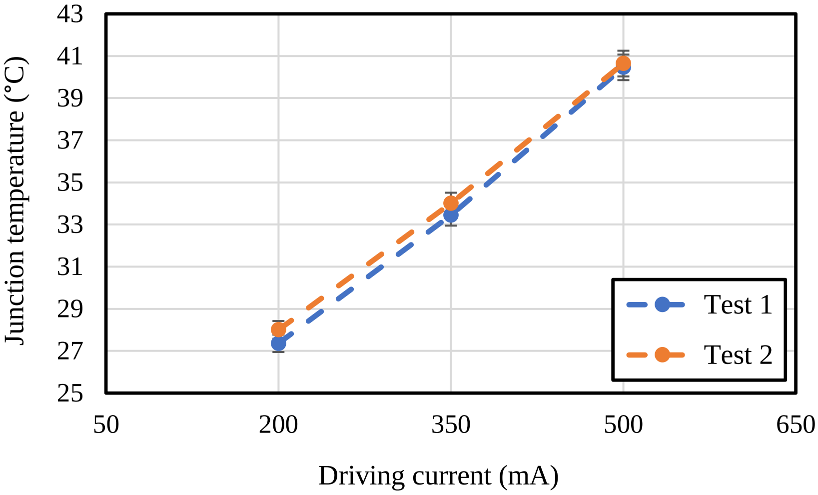

Figure 96: Repeatability tests of the high-power white LED

in the final measurement system

3.8.2.2 Comparison Tests

In order to evaluate the accuracy of the measurements performed with the integrated final measurement system, the final measurement data were compared with the previous experimental data for the blue and white LEDs. Measurement results for the blue LED are shown in Table 10 and Figure 97 while the results for the white LED are given in Table 11 and Figure 98.

The maximum difference between initial experimental data and measurement device data for the blue LED was 3.1°C while it was 2.6°C for the white LED. The difference in measurement results (maximum 7.4%, minimum 2.8%) is related to the variations in experimental conditions and in-device conditions as expected (such as differences in test environment temperatures and LED positioning).

Table 10: Comparison of the results between the previous experiments and final measurement device for the high-power blue LED

Blue LED – Junction temperatures (°C)

Current (mA)	Previous experimental data	Final EVAtherm measurement	Variation (%)
200	36.1	35.1	2.8
350	43.0	41.1	4.4
500	50.8	47.7	6.1

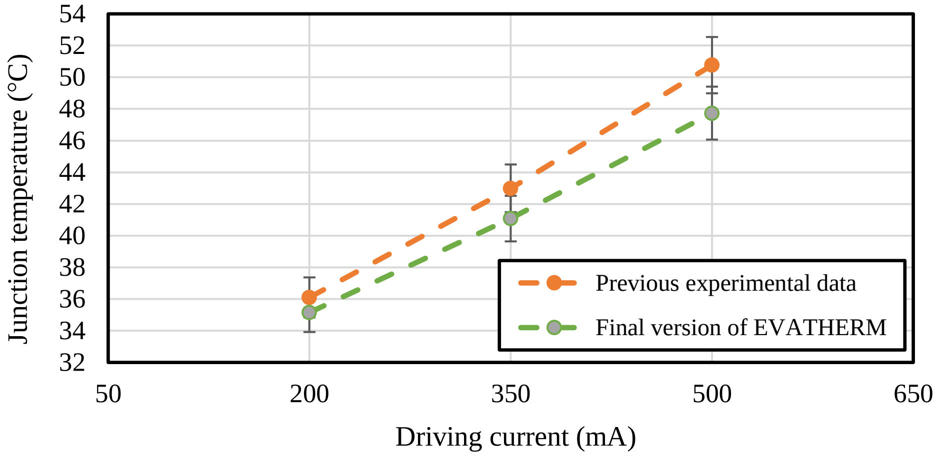

Figure 97: Graphical comparison of the final EVAtherm data of the high-power blue LED with the previous experimental data

Table 11: Comparison of the results between the previous experiments and final measurement device for the high-power white LED

White LED – Junction temperatures (°C)

Current (mA)	Previous experimental data	Final EVAtherm measurement	Variation (%)
200	29.6	27.4	7.4
350	35.9	33.5	6.7
500	43.1	40.5	6.0

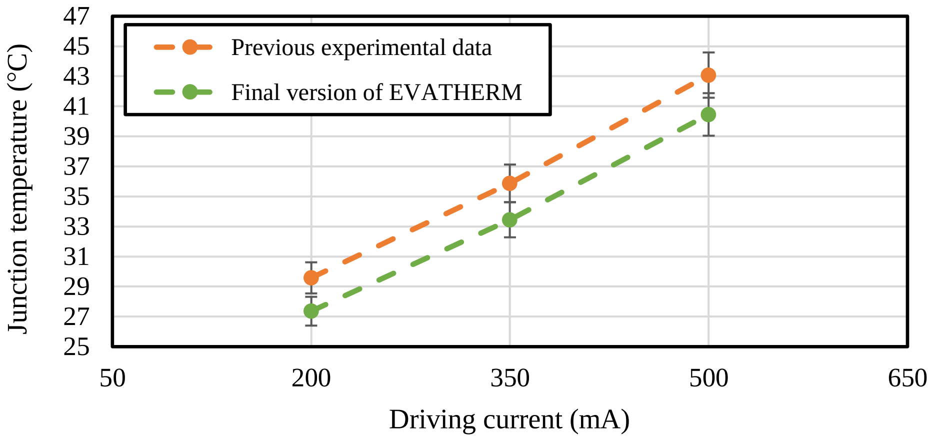

Figure 98: Graphical comparison of the final EVAtherm data of the high-power white LED with the previous experimental data

CHAPTER IV

SUMMARY AND CONCLUSIONS

While LEDs offer unique advantages, their rapid penetration into our lives posed new challenges especially in thermal management. LED junction temperature affecting both lumen output and lifetime is a critical parameter that needs to be identified carefully along with the analysis of its impact on optical performance of lighting systems.

The thesis aims to fill an important gap in the literature by investigating:

- Accurate measurement techniques of junction temperature in single RGB and white multi-LED systems and comparison of various measurement methods.
- Optothermal interactions in high power single red LEDs with a clear understanding of the impact of an LED dome and generated heat on the performance of an LED package.
- Variation in forward voltage drop and optothermal characteristics of high power RGB LEDs due to various materials used in the light-emitting layer.
- A new junction temperature measurement technique for multi-LED systems and investigate the impact of electronics and local hot spots on optical performance.
- Effective design and manufacturing techniques for the development of a junction temperature device that is competitive enough to provide fast and reliable measurements compared to other products in the market.

Analysis technique and the conclusions drawn are described below with greater details:

In the thesis, the impact of operating current/junction temperature/heat generation on forward voltage, electrical power, radiant power and conversion efficiency was investigated for a high-power red light-emitting diode. As a part of the study, the effect of an LED dome, a significant component in the package, was also studied to further characterize a red LED package and understand thermal, optical and electrical interactions in the package. The comparison of the LED with and without dome cases gives future studies or applications a good reference and insightful analysis of the dome's thermal and optical role to further improve the high-power red LED packages. In fact, well-understanding of the behavior of these systems is needed for designing future applications. As more IoT sensors and related electrical components are included in lighting systems, thermal challenges become more significant to address due to additional heat loads in the circuits. Therefore, as the development of monochromatic lighting sources and the lighting control systems accelerate, thorough understanding of monochromatic high-power LED systems helps scientists, engineers and developers design more effective lighting systems considering optical performance at various thermal conditions. In addition, the comparison of high-power red LEDs with high power blue LEDs also paves the way for the future research and development studies to consider red LEDs as an alternative in a number of applications where they can replace the blue LEDs.

The study also proves that thermal imaging method gives approximate results for the junction temperature when the LED dome is removed. Thus, it can be used to verify the results obtained from forward voltage method. However, in the case of the LED with dome, temperature of the chip surface cannot be directly measured by the IR thermal camera and the junction measurement results may not be reliable. In fact, the IR camera measures the dome temperature when the dome is kept, and it is quite different from the junction temperature.

In addition, the effect of the LED dome on thermal, electrical and optical characteristics was investigated with respect to various operating currents. One of the most remarkable findings was to observe an increase in the junction temperature even though less heat was generated when the dome was removed from the LED. This was mainly attributed to the effect of an LED dome on thermal characteristics of the chip. When the LED dome is removed, one of the conductive paths is lost and the heat generated over the junction region is conducted less effectively. As a result, junction temperature is increased and leads to a further voltage drop and less radiant energy.

It was also observed that the ratio of radiant energy to electrical energy decreases as the operating current is increased and the difference between two configurations (with a dome and without a dome) decreases at higher operation currents. Furthermore, a red LED was compared with a blue LED in terms of their junction temperatures, radiant powers and conversion efficiencies. It was found that the blue LED has a higher junction temperature and the difference between two LEDs gets larger by 13.7˚C from 200 to 500 mA. However, the blue LED has a higher light output and conversion efficiency than the red LED at each application current.

The junction temperatures of a red LED were compared with three different measurement techniques including FVCM, TIM and computational methods. Junction temperature results of red LEDs operating at three different currents and configurations are seen in Table 12. The LED configurations are represented by the numbers in the table: the LED with dome (1), the unpainted LED without dome (2) and the painted LED without dome (3). Relative errors of thermal imaging and CFD methods are also given with respect to FVCM.

Table 12: Comparison of three different methods

Currents (mA)	LED configuration	Junction temperature results of three methods (°C)				
		FVCM	TIM	Relative error (%)	CFD	Relative error (%)
200	1	31.8	-	-	31.7	0.5
	2	33.5	35.8	6.9	33.1	1.2
	3	39.3	39.5	0.6	38.7	1.5
350	1	41.4	-	-	41.1	0.7
	2	44.8	45.9	2.5	43.6	2.7
	3	54.7	54.8	0.1	52.5	4.0
500	1	52.0	-	-	52.0	0.0
	2	57.9	57.7	0.4	54.8	5.4
	3	71.1	70.9	0.2	66.7	6.2

A close examination of findings shows that the greatest relative errors obtained with thermal imaging and numerical methods were respectively 6.9% and 6.2% compared to the results from forward voltage method. In general, the measurement errors were found in an acceptable range for the junction temperatures of the red LED.

In another study, experiments have been performed to understand the relationship between forward voltage, junction temperature, heat generation and optical behaviors of RGB LEDs. Junction temperatures of RGB LEDs were measured with forward voltage method and the change in optothermal characteristics were analyzed between two driving currents of 100 mA and 200 mA. A 1 mV change in forward voltage readings of a calibration data has shown a variation of 0.3 to 0.8˚C in junction temperatures of LEDs. Therefore, obtaining accurate forward voltage results especially in calibration phase is very critical in order to have reliable junction temperature results.

Based on the calibration equations, the largest slope was observed in the green LED, while the smallest slope was found for the blue LED chip. Therefore, it was understood that green LEDs were electrically more sensitive to the junction temperature changes since larger forward voltage drops were measured for the unit change in junction temperature.

In the thesis, a new approach was introduced to measure junction temperature of a serially connected multi-LED systems using Forward Voltage Change Method. Frequently, average junction temperatures are reported to describe thermal behavior of LEDs in multi-chip systems. However, thermal conditions of one LED may differ than the others significantly and the performance, and lifetime predictions of the lighting system could be underestimated especially in serially connected systems. In addition, frequently used transient measurement method is not applicable for junction temperature measurements of serially connected multi-chip systems [55]. The proposed novel approach in this study is related with the practical determination of junction temperature of each LED in a multi-chip system. While controlling each serially connected LED, individual LED junction temperatures are measured. In the study, thermal, electrical and optical measurements were also performed to show how certain performance parameters interact with each other.

According to the findings, it was understood that junction temperature measurement of individual LEDs in a multi-chip system is possible and useful to evaluate the selection of electrical components and their relative positions on the PCB. In fact, determination of an average junction temperature of LEDs may not be useful for these systems. As it is observed in the case of LED-3 in the Section 2.4.2, additional electrical components placed on the PCB may increase the junction temperature of a certain LED much higher than other components. Thus, enough care should be given to thermal issues since optical performance is considerably affected by thermal loads in multi-chip systems. In fact, it was shown that 0.39 W heat generation due to additional electrical components in the circuit was approximately equal to total amount of radiant flux during 12 V application and it decreased the conversion efficiency of the system by 6.1% compared to the conversion efficiency of the LEDs. Drop in the performance of the lighting unit was also observed in luminous efficacy of the multi-LED system. It was shown that 30.9°C increase in average junction temperature of LEDs led to 23% drop in luminous efficacy (lm/W). Furthermore, phosphor temperature was found to be even higher than junction temperature. Local hot spots were identified with an IR thermal camera and the surface temperature of phosphor layers were measured for each LED. As a result, the temperatures of the phosphor layers were clearly higher than junction temperatures for each LED with the biggest difference in LED-3 which is close to the additional electronic components. Temperature distribution over the LED system showed the contribution of heat generating components to the additional increase of junction and phosphor temperatures of LED-3.

With the experimental tests and experiences in junction temperature measurements, it was aimed to develop a junction temperature device that is user friendly and simple, highly automated, accurate and fast. The measurement method applied with the introduced device does not include the transient measurement technique with one dimensional heat flow assumption. Instead, steady state junction temperature measurements are carried out with the pulse current application in a novel rapid measurement chamber. The measurement system could play a significant role in reliable measurements of junction temperature that directly affects the optical performance and lifetime of LEDs and offer a practical solution to the determination of junction temperature of individual LEDs in multi-chip systems. These measurements are believed to be even more significant in future applications when Internet of Things (IoT) sensors and associated electrical components are more frequently included in LED lightings units. Thus, the measurement system can characterize the thermal condition of an LED unit and allow researchers, engineers and experts to optimize the design of their LED products considering various heat generators in their modules.

CHAPTER V

RECOMMENDATIONS FOR FUTURE WORK

In future studies, optimization of electrical components in these systems can be made by using the improved junction temperature measurement method introduced in this study. Furthermore, junction temperature measurements can be made more sensitively if supply and measure probes are developed and used instead of the soldered electrical connections in the current study. It is believed that the current technique introduced in the study can pave a way for experimental optimization techniques of multi-chip systems and contribute to the reduction in energy costs of LED lighting systems. In addition to the measurement technique for serially connected multi-LED systems, highly accurate and fast measurement method can be developed for parallelly connected multi-LED systems as well.

Last but not least, junction temperature test chamber could be improved even more with humidity control mechanisms in order to examine the performance of newly developed LED packages at forced conditions. This requires even more compact design to reduce the need for higher cooling requirements of the chamber. In addition, machine learning models can be developed and adapted to the measurement software based on the electrical and thermal data collected at the early stage of the measurements to predict the junction temperature at steady state. This could significantly reduce total measurement time of the measurement device.

Another version of junction temperature measurement device can also be developed with the inclusion of robotic arms in the test chamber to touch and measure the junction temperatures of the specific LEDs over an LED board. With this improvement, the measurement device can be automatized for the multi-LED systems and create a significant advantage over traditional measurement methods.

BIBLIOGRAPHY

[1] Online source, available: historyoflighting.net.

[2] Online source, available: archlighting.com.

[3] Online source, available: parkscandles.com.

[4] Online source, available: stouchlighting.com.

[5] Online source, available: exportersindia.com.

[6] Online source, available: tenaquip.com.

[7] Online source, available: deliciousrecipemix.com.

[8] Online source, available: osa-opn.org.

[9] Online source, available: electronics-notes.com.

[10] Online source, available: lightvu.com.

[11] Online source, available: circuitstoday.com.

[12] Online source, available: light.fi.

[13] Online source, available: needhamelectric.com.

[14] Online source, available: seenew.net.

[15] Online source, available: wired.com.

[16] Online source, available: shineretrofits.com.

[17] Online source, available: sciencenews.org.

[18] Online source, available: latimes.com.

[19] G. Harbers, C. G. A. Hoelen, 2001, “High Performance LCD Backlighting using High Intensity Red, Green and Blue Light Emitting Diodes,” SID Intl Symp Dig. Tech Pap., pp. 702–706.

[20] T. Komine, M. Nakagawa, 2004, “Fundamental analysis for visible-light communication system using LED lights”, IEEE Transactions on Consumer Electronics, 50(1), 100-107.

[21] T. Taguchi, Y. Uchida, K. Kobashi, 2004, "Efficient white LED lighting and its application to medical fields", Phys. Stat. Sol. (a), 201(12), 2730–2735.

[22] Y. Lai, N. Cordero, F. Barthel, F. Tebbe, J. Kuhn, R. Apfelbeck, D. Würtenberger, 2009, “Liquid cooling of bright LEDs for automotive applications”, Applied Thermal Engineering, Volume 29, Issues 5-6, Pages 1239-1244.

[23] Online source, available: Images.google.com.

[24] Online source, available: Images.freepik.com.

[25] Online source, available: Images.unsplash.com.

[26] Online source, available: energystar.gov.

[27] F. G. Montoya, A. Pena-Garcia, A. Juaidi, F. Manzano-Agugliaro, 2017, “Indoor lighting techniques: An overview of evolution and new trends for energy saving”, Energy and Buildings, Volume 140, Pages 50-60.

[28] Online source, available: energy.gov.

[29] G. Harbers, C. Hoelen, 2012, “LP-2: High Performance LCD Backlighting using High Intensity Red, Green and Blue Light Emitting Diodes”, Society for Information Display (SID), Volume 32, Issue 1, Pages 702-705.

[30] B. Yang, X. Chen, 2010, “Full-color skin imaging using RGB LED and floating lens in optical coherence tomography”, Biomedical Optics Express, Vol. 1, Issue 5, Pages 1341-1346.

[31] Online source, available: statista.com.

[32] Photon Start Technology, 2016, “How LEDs produce white light,” pp. 13–16.

[33] H. Ye, H. Tang, S. Leung, C. Qian, X. Fan, G. Zhang, 2015, “Junction temperature measurement to optimize thermal design of LED arrays,” 2015 12th China Int. Forum Solid State Light. SSLCHINA 2015, pp. 47–51.

[34] M. Arik, C. A. Becker, S. E. Weaver, and J. Petroski, 2004, “Thermal management of LEDs: package to system,” no. January 2004, p. 64.

[35] M. N. Inan, M. Arik, 2014, “A multi-functional-design approach and of figure of merits for LED lighting systems”, Journal of Solid State Lighting.

[36] U. Z. Uras, M. Arik, E. Tamdogan, 2017, “Thermal Performance of a Light Emitting Diode Light Engine for a Multipurpose Automotive Exterior Lighting System With Competing Board Technologies”, Journal of Electronic Packaging, 139(2), 020907.

[37] Online source, available: electronicsdesk.com.

[38] Online source, available: studentsheart.com.

[39] Online source, available: circuitbread.com.

[40] Online source, available: physics-and-radio-electronics.com.

[41] X. Luo, R. Hu, S. Liu, K. Wang, “Heat and fluid flow in high-power LED packaging and applications,” Prog. Energy Combust. Sci., vol. 56, pp. 1–32, 2016.

[42] Online source, available: ee.co.za.

[43] S. Leng, 2017, “Identifying and evaluating aging signatures in light emitting diode lighting systems"', Thesis study.

[44] Steven Keeping, 2011, “Whiter, Brighter LEDs”, Online source, available: digikey.com.

[45] Y. Gu, N. Narendran, 2004, “A noncontact method for determining junction temperature of phosphor-converted white LEDs,” no. January 2004, p. 107.

[46] V. N. Popok, S. Buhrkal-Donau, B. Czerny, G. Khatibi, H. Luo, F. Iannuzzo, K. B. Pedersen, 2019, “Comparative study of wire bond degradation under power and mechanical accelerated tests”, Journal of Materials Science: Materials in Electronics.

[47] Greg Caswell, 2015, "The Transition to High Brightness LEDs", White Paper, DfR Solutions.

[48] Online source, available: ledrise.eu.

[49] Online source, available: ecse.rpi.edu.

[50] H. I. Kahvecioglu, E. Tamdogan, M. Arik, 2018, “Investigation of combined optical and thermal effects on phosphor converted light-emitting diodes with liquid immersion cooling,” Opt. Eng. 57(5), 055101.

[51] E. Tamdogan, M. Arik, 2015, "Natural Convection Immersion Cooling With Enhanced Optical Performance of Light-Emitting Diode Systems", Journal of Electronic Packaging, 137(4), 041006.

[52] A. Jayawardena, Y. Liu, N. Narendran, 2013, "Analysis of three different junction temperature estimation methods for AC LEDs", Solid-State Electronics, 86, 11–16.

[53] J. Senawiratne, Y. Li, M. Zhu, Y. Xia, W. Zhao, T. Detchprohm, A. Chatterjee, J.L.Plawsky, C.Wetzel, 2008, “Junction Temperature Measurements and Thermal Modeling of GaInN/GaN Quantum Well Light-Emitting Diodes”, Journal of Electronic Materials, vol. 37, issue 5, pp. 607–610.

[54] S. Chhajed, Y. Xi, T. Gessmann, J.-Q. Xi, J. M. Shah, J. K. Kim, E. F. Schubert, 2005, "Junction temperature in light-emitting diodes assessed by different methods". Light-Emitting Diodes: Research, Manufacturing, and Applications.

[55] D. Lee, H. Choi, S. Jeong, C. H. Jeon, D. Lee, J. Lim, C. Byon, J. Choi, 2018, "A study on the measurement and prediction of LED junction temperature", International Journal of Heat and Mass Transfer, 127, 1243–1252.

[56] H.-L. Ke, Q. Sun, J. Zhao, H.-X. Zhang, L. Jing, Y. Wang, J. Hao, 2016, "Junction temperature estimation for LED lamp with forward voltage method", 17th International Conference on Thermal, Mechanical and Multi-Physics Simulation and Experiments in Microelectronics and Microsystems (EuroSimE).

[57] OSRAM, 2010, “LED Basics”.

[58] Online source, available: education.mrsec.wisc.edu.

[59] R. Horng, P. Han, D. Wuu, 2008, “Phosphor-Free White Light from InGaN Blue and Green Light-Emitting Diode Chips Covered with Semiconductor-Conversion AlGaInP Epilayer”, IEEE Photonics Technology Letters, Vol. 20, No. 13.

[60] Online source, available: lrc.rpi.edu.

[61] Y. Luo, 2012, “Use Isothermal Surface to Help Understanding the Spatial Representation of Structure Function,” pp. 63–68.

[62] E. Juntunen, O. Tapaninen, A. Sitomaniemi, and V. Heikkinen, 2013, “Effect of Phosphor Encapsulant on the Thermal Resistance of a High-Power COB LED Module,” vol. 3, no. 7, pp. 1148–1154.

[63] L. Yang, B. Wei, and J. Zhang, 2012, “Transient thermal characterization of organic light-emitting diodes”, Semiconductor Science and Technology, Volume 27, Number 10.

[64] C. Weng, 2009, “Advanced thermal management and management of LED packages”, ELSEVIER, International Communications in Heat and Mass Transfer, Volume 36, Issue 3, Pages 245-248.

[65] H. Wu, K. Lin, S. Lin, 2012, “A study on the heat dissipation of high power multi-chip COB LEDs”, ELSEVIER, Microelectronics Journal, Volume 43, Issue 4, Pages 280-287.

[66] L.Yuan, S. Liu, M. Chen, X. Luo, 2006, “Thermal Analysis of High Power LED

Array Packaging with Microchannel Cooler”, IEEE, International Conference on Electronics Packaging Technology.

[67] K. Chen, N. Narendran, 2013, “Microelectronics Reliability Estimating the average junction temperature of AlGaInP LED arrays by spectral analysis,” Microelectron. Reliab., vol. 53, no. 5, pp. 701–705.

[68] D. Shi, S. Feng, Y. Zhang, Y. Qiao, B. Deng, 2015, “Thermal investigation of LED array with multiple packages based on the superposition method,” Microelectronics J., vol. 46, no. 7, pp. 632–636.

[69] M. Ha, S. Graham, 2012, “Development of a thermal resistance model for chip-on-board packaging of high power LED arrays”, ELSEVIER Microelectronics Reliability, Volume: 52, Issue: 5, Page: 836.

[70] Y. Xi, J.-Q. Xi, T. Gessmann, J.M. Shah, J.K. Kim, E.F. Schubert, 2005, “Junction and carrier temperature measurements in deep-ultraviolet light-emitting diodes using three different methods”, Applied Physics Letters, Volume 86, Issue 3.

[71] E. Hong, N. Narendran, 2004, “A method for protecting useful life of LED lighting systems”, Proc. SPIE 5187, Third International Conference on Solid State Lighting.

[72] Technical Guide, 2017, “Integrating Sphere Theory and Applications”, Labsphere.

[73] Total Spectral Flux Calibration Certificate, 2017, Labsphere, SCL-1400-K120.

[74] M. Tarin, 2016, "Choosing a camera for infrared imaging", online source, available: vision-systems.com.

[75] J. Garg, M. Arik, S. Weaver, 2005, “Impingement Air Cooling With Synthetic Jets

Over Small and Large Heated Surface”, ASME Thermal Management of Electronic and Photonic Systems, IPACK2005-73211, pp. 277-285.

[76] Y. Ma, W. Lan, B. Xie, R. Hu, X. Luo, 2018, “An optical-thermal model for laser-excited remote phosphor with thermal quenching”, International Journal of Heat and Mass Transfer, 116, 694–702.

[77] ANSYS Icepak, 2013, ANSYS Icepak Tutorials, Release 15.0, ANSYS, Inc.

[78] B. Ozluk, A. M. Muslu, M. Arik, 2019, "A Comparative Study for the Junction Temperature of Green Light Emitting Diodes (LED)s", IEEE Transactions on Components, Packaging and Manufacturing Technology.

[79] A. Hanß, M. Schmid, E. Liu, G. Elger, 2015, “Transient thermal analysis as measurement method for IC package structural integrity”, Chin. Phys. B, Vol. 24, No. 6 (2015) 068105.

[80] E. Ozuturk, 2013, “Formulation of the LED’s radiant power current characteristic at pulsed high currents”, International Journal for Light and Electron Optics, Volume 124, Issue 18, Pages 3549-3553.

[81] C.-C. Sun, T.-X. Lee, Y.-C. Lo, C.-C. Chen, S.-Y. Tsai, 2011, “Light extraction enhancement of GaN-based LEDs through passive/active photon recycling”, Optics Communications, 284(20), 4862–4868.

[82] H. Zhang, M. Wagner, T. Q. Khanh, 2017, "Comparing New Dielectric Materials for Chip-on-Board LED Packages", LpR Article.

[83] C.-P. Ching, M. Devarajan, W.-C. Liew, 2011, "Thermal characterization of a high power infrared emitter as a function of input current" IEEE 2nd International

Conference on Photonics (ICP), IEEE, pp. 1–5.

[84] Online source, available: mentor.com.

[85] E. Tamdogan, G. Pavlidis, S. Graham, M. Arik, 2018, “A Comparative Study on the Junction Temperature Measurements of LEDs With Raman Spectroscopy, Forward Voltage Methods,” IEEE Trans. Components, Packag. Manuf. Technol., vol. 8, no. 11, pp. 1914–1922.

[86] R. J. Moffat, “Describing the uncertainties in experimental results,” Exp. Therm. Fluid Sci., vol. 1, no. 1, pp. 3–17, 1988.

[87] S. Kline and F. McClintock, “Describing uncertainties in single - sample experiments,” Mech. Eng., vol. 75, no. 1, pp. 3–8, 1953.

[88] J. H. Kim and T. W. Simon, “Journal Of Heat Transfer Polıcy On Reportıng Uncertaıntıes In Experımental Measurements And Results,” J. Heat Transf., vol. 115, no. 1, pp. 5–6, 1993.

[89] R. J. Moffat, “Using Uncertainty Analysis in the Planning of an Experiment,” J. Fluids Eng., vol. 107, no. 2, pp. 173–178, 1985.

[90] J. P. Holman, Heat Transfer, Tenth Edit. McGraw-Hill Series in Mechanical Engineering, 2012.

[91] R. S. Figliola and D. E. Beasley, Theory and Design for Mechanical Measurements, Fifth Edit. John Wiley & Sons, Inc., 2011.

[92] H. W. Coleman and W. G. J. Steele, “Experimentation, errors, and uncertainty,” in Experimentation, Validation, and Uncertainty Third Edition, Third Edit., John

Wiley & Sons, Inc. ISBN: 978-0-470-16888-2, 2009, pp. 1–27.

[93] “Kalibrasyon Ölçüm Belirsizliği”, 2015, Turkish Standards Institution.

APPENDIX A

A.1 Uncertainty Analysis of Junction Temperature Measurements

A number of factors including the conditions of a measurement equipment and an experimental test affect the uncertainty of experimental results. Deviations in experimental results may stem from the fluctuations in test conditions, calibration of an experimental equipment, or knowledge and experience of an experimenter. In an uncertainty analysis, all possible factors that may affect the experimental results need to be evaluated as an uncertainty contributor. Systematic and random errors are the main categories of sources of errors observed in an experiment. Systematic errors affect the experimental results in a systematic way and may include the improper use of an experimental method or an experimental device with no calibration. On the other hand, random errors are considered as the unpredictable variations in the course of experiments. A combination of these errors constitutes the total error of an experiment. While the calculation of random errors in an experiment determines the precision of an experiment, systematic (bias) errors are typically included in uncertainty calculations with a calibration and manufacturer data including the accuracy and resolution of an experimental equipment.

Following procedure is followed to include the impact of experimental variables or uncertainty contributors on uncertainty of experimental results ([86] - [92]):

First of all, precision errors of repeated measurements are calculated by using student t-distribution at 95% confidence interval with the (n-1) degrees of freedom:

Table 13: Calculation procedure of precision errors

$$\bar{x} = \frac{1}{n} \sum_{k=1}^{n} x_k \quad \textbf{(1)}$$

$$\sigma_x = \left[\frac{1}{n-1} \sum_{k=1}^{n} (x_k - \bar{x})^2\right]^{0.5} \quad \textbf{(2)}$$

$$\sigma_{\bar{x}} = \frac{\sigma_x}{\sqrt{n}} \quad \textbf{(3)}$$

$$P_x = t_{(n-1),95\%}\, \sigma_{\bar{\bar{x}}} \quad \textbf{(4)}$$

where

$\bar{x}$ = Average of measurement data

x_k = Measurement data of an independent variable

n = Total number of measurements

σ_x = Standard deviation of measurement data

$\sigma_{\bar{x}}$ = Mean standard deviation

$t_{(n-1),95\%}$ = student t-distribution at 95% confidence interval with the (n-1) degrees of freedom

P_x = Precision limit

After the calculation of precision errors for each independent variable, bias errors are also calculated with data provided by manufacturer including resolution and accuracy of a measurement equipment. The formula used to calculate the bias error is given as follows:

$$B = \mp[(0.5\,R)^2 + (A)^2]^{0.5} \quad \textbf{(5)}$$

B = Bias error

R = Resolution

A = Accuracy

While certain contributors directly affect junction temperature measurements and are included in precision error calculations, other contributors are not included in the equations but affect sourcing of pulse and driving currents. Only bias error calculations are made for those contributors. Repeated measurement data is used in the calculation of precision errors for the contributors that are directly involved in equations. Uncertainty contributors or variables and their associated error types and the sources of errors are given in Table 14.

Table 14: Experimental variables and the sources of errors

Variable	Error type	Source of systematic error	Source of random error
V_{f_c}	Bias + precision error	Sourcemeter	Repeatability tests
V_{f_t}	Bias + precision error	Sourcemeter	Repeatability tests
T_{j_c}	Bias + precision error	DAQ + Thermocouple + Computer + Oven system	Repeatability tests
I_{p_c}	Only bias error	Sourcemeter	-
I_{p_t}	Only bias error	Sourcemeter	-
t_{p_c}	Only bias error	Sourcemeter	-
t_{p_t}	Only bias error	Sourcemeter	-
I_t	Only bias error	Sourcemeter	-

where

V_{f_c} = Forward voltage data at the calibration phase of measurements

$\mathrm{V}_{\mathrm{f}_\mathrm{t}}$ = Forward voltage data at the actual test phase of measurements

$\mathrm{T}_{\mathrm{j}_\mathrm{c}}$ = Junction temperature data at calibration phase of measurements

$\mathrm{I}_{\mathrm{p}_\mathrm{c}}$ = Pulse current magnitude at the calibration phase of measurements

$\mathrm{I}_{\mathrm{p}_\mathrm{t}}$ = Pulse current magnitude at the actual test phase of measurements

$\mathrm{t}_{\mathrm{p}_\mathrm{c}}$ = Pulse current duration at the calibration phase of measurements

$\mathrm{t}_{\mathrm{p}_\mathrm{t}}$ = Pulse current duration at the actual test phase of measurements

I_t = Driving current magnitude at the actual test phase of measurements

In the calculation of bias errors, resolution and accuracy of a measurement equipment are taken from the manufacturer data sheets and presented in Table 15.

Table 15: Resolution and accuracy of measurement equipment

Variable	Resolution	Accuracy
$\mathrm{V}_{\mathrm{f}_\mathrm{c}}$ (Sourcemeter) (V)	0.00001	0.001375
$\mathrm{V}_{\mathrm{f}_\mathrm{t}}$ (Sourcemeter) (V)	0.00001	0.001375
$\mathrm{T}_{\mathrm{j}_\mathrm{c}}$ (DAQ) (°C)	0.1	0.014
$\mathrm{T}_{\mathrm{j}_\mathrm{c}}$ (Thermocouple) (°C)	0.1	1
$\mathrm{T}_{\mathrm{j}_\mathrm{c}}$ (Computer) (°C)	0.1	0.015
$\mathrm{T}_{\mathrm{j}_\mathrm{c}}$ (Oven system) (°C)	-	0.5
$\mathrm{I}_{\mathrm{p}_\mathrm{c}}$(Sourcemeter) (mA)	0.00002	0.0006
$\mathrm{I}_{\mathrm{p}_\mathrm{t}}$(Sourcemeter) (mA)	0.00002	0.0006
$\mathrm{t}_{\mathrm{p}_\mathrm{c}}$ (Sourcemeter) (ms)	0.001	0.005
$\mathrm{t}_{\mathrm{p}_\mathrm{t}}$(Sourcemeter) (ms)	0.001	0.005
I_t (Sourcemeter) (mA)	0.02	1.9

If an experimental variable is involved in the calculations with a group of measurement data, then precision errors are calculated for each group of data and then the final precision error is calculated with the given formula:

$$\mathrm{P} = [\mathrm{P}_1^2 + \mathrm{P}_2^2 + \cdots + \mathrm{P}_n^2]^{0.5} \qquad \textbf{(6)}$$

where

P = Final precision error

P_n = Precision error of a group of data

Likewise, the final bias error is calculated with the formula below:

$$\mathrm{B} = [\mathrm{B}_1^2 + \mathrm{B}_2^2 + \cdots + \mathrm{B}_n^2]^{0.5} \qquad \textbf{(7)}$$

where

B = Final bias error

B_n = Bias error of a group of data

After the calculation of final precision and bias errors for each variable, absolute uncertainty is calculated as follows:

$$\mathrm{U}_x = \pm\left[{\mathrm{B}_x}^2 + \mathrm{P}_x^2\right]^{0.5} \qquad \textbf{(8)}$$

where

U_x = Absolute uncertainty

B_x = Bias error

P_x = Precision limit

The relative uncertainty can also be calculated with the absolute uncertainty and measurement data as a percentage value:

$$U_{R_x}\% = \frac{U_x}{x}\% = \pm\left(\frac{U_x}{x}\right)\times 100 \qquad \textbf{(9)}$$

where

U_{R_x} = Relative uncertainty

U_x = Absolute uncertainty

x = Measurement data of an independent variable

If one variable is dependent on a multiple of independent variables, then the following formulas are used to describe the absolute and relative error expression [86]:

$$U_{OP} = \left[\left(\frac{\partial U}{\partial x_1}U_1\right)^2 + \left(\frac{\partial U}{\partial x_2}U_2\right)^2 + \cdots + \left(\frac{\partial U}{\partial x_n}U_n\right)^2\right]^{0.5} \qquad \textbf{(10)}$$

$$\frac{U_{OP}}{OP} = \pm\left[\left(\frac{U_{x_1}}{x_1}\right)^2 + \left(\frac{U_{x_2}}{x_2}\right)^2 + \cdots + \left(\frac{U_{x_n}}{x_n}\right)^2\right]^{0.5} \qquad \textbf{(11)}$$

where

OP = Objective parameter to be measured

U_{OP} = Uncertainty of objective parameter to be measured

$U_n = U_{x_n}$ = Absolute uncertainty of the nth independent variable

x_n = Measurement data of the nth independent variable

In junction temperature measurements, uncertainty contributors are forward voltage at calibration and test phase, junction temperature at calibration phase, pulse current at calibration and test phase, pulse duration at calibration and test phase and driving current at test phase. Thus, uncertainty of the measured junction temperature with actual tests is dependent on the individual uncertainties of these variables as represented in the formula below:

$$\frac{U_{T_j}}{T_j} = \frac{U_{V_{f_c}}}{V_{f_c}} + \frac{U_{V_{f_t}}}{V_{f_t}} + \frac{U_{T_{j_c}}}{T_{j_c}} + \frac{U_{I_{p_c}}}{I_{p_c}} + \frac{U_{I_{p_t}}}{I_{p_t}} + \frac{U_{t_{p_c}}}{t_{p_c}} + \frac{U_{t_{p_t}}}{t_{p_t}} + \frac{U_{I_t}}{I_t} \qquad \mathbf{(12)}$$

where

U_{T_j} = Absolute uncertainty of junction temperature at the actual test phase: objective parameter

$U_{V_{f_c}}$= Absolute uncertainty of forward voltage data at the calibration phase

$U_{V_{f_t}}$= Absolute uncertainty of forward voltage data at the actual test phase

$U_{T_{j_c}}$= Absolute uncertainty of junction temperature data at calibration phase

$U_{I_{p_c}}$= Absolute uncertainty of pulse current magnitude at the calibration phase

$U_{I_{p_t}}$= Absolute uncertainty of pulse current magnitude at the actual test phase

$U_{t_{p_c}}$= Absolute uncertainty of pulse current duration at the calibration phase

$U_{t_{p_t}}$= Absolute uncertainty of pulse current duration at the actual test phase

U_{I_t}= Absolute uncertainty of driving current magnitude at the actual test phase

A.2 Uncertainty Analysis of Optical Measurements

In the uncertainty calculations of optical measurements, an appropriate statistical distribution method is determined for each measurement uncertainty component. The uncertainty values from the reference documents are used for each measurement uncertainty component and the calculations of standard measurement uncertainty follow with the referenced uncertainties as described below. Then, compound uncertainty and extended uncertainty calculations are performed [93].

First of all, the relationship between input and output sizes is determined as shown:

$$y = F(x_1, x_2, x_3, \dots, x_n) \quad \textbf{(13)}$$

where

y = output value

x_n = nth input value

A rectangular or normal distribution is assumed for each component of uncertainty. These distribution variations give information about the intervals at which measurement results are likely to be more and/or less frequent. In the estimation of measurement uncertainty, distribution coefficients specific to these statistical distributions are also considered.

For rectangular distribution,

$$u(x_i) = \frac{a_i}{\sqrt{3}} \quad (\mathbf{14})$$

For normal distribution,

$$u(x_i) = \frac{a_i}{k} \quad (\mathbf{15})$$

formulas are used;

where

$u(x_i)$ = Standard measurement uncertainty,

a_i = Reference uncertainty value from referenced documents

k = Coverage (expansion) factor (typically 2 for 95% confidence level).

A.2.1 Uncertainty Calculations of Repeatability Tests

Arithmetic mean, experimental standard deviation and standard measurement uncertainty calculations are made to determine the uncertainties in repeated measurements. These calculations are carried out with the following formulas:

Experimental standard deviation value:

$$\mathrm{S} = \sqrt{\frac{\sum_{\mathrm{i}=1}^{\mathrm{n}}(\mathrm{X_i} - \overline{\mathrm{X}})^2}{\mathrm{n} - 1}} \qquad (\mathbf{16})$$

where

S = Experimental standard deviation value,

X_i = Input value that affects the measurement result,

$\overline{X}$ = Average of input values,

n = Total number of measurements.

Deviation of the average value:

$$\mathrm{S}_{\overline{\mathrm{q}}} = \frac{\mathrm{S_q}}{\sqrt{\mathrm{n}}} \qquad (\mathbf{17})$$

where

$S_{\overline{q}}$ = u (x_i) = Standard measurement uncertainty,

S_q = Experimental standard deviation,

n = Total number of measurements.

A.2.2 Determination of Uncertainty Contributors and Their Variance Values

For all specified uncertainty components, uncertainty values given or estimated from sources such as calibration certificate, reference documents, measurement activities are taken. The statistical distribution type is determined for each uncertainty component. Standard uncertainty of measurement is obtained using uncertainty values and distribution types for each uncertainty component. The sensitivity coefficient is calculated by taking the derivative of the output parameter with respect to the input variable for each uncertainty component. The uncertainty contribution is obtained by multiplying the standard measurement uncertainty and the sensitivity coefficient. Variance is also obtained by squaring the uncertainty contribution obtained for each uncertainty component. The sum of the variance values gives the compound (total) measurement uncertainty, and the compound measurement uncertainty multiplied by the expansion factor yields the expanded measurement uncertainty.

<u>Compound uncertainty value:</u>

$$u_c(y) = \sqrt{\sum_{i=1}^{n} \left[\frac{\partial f}{\partial x_i}\right]^2 u^2(x_i)} \qquad \mathbf{(18)}$$

where

$u_c(y)$ = Compound uncertainty,

$u^2(x_i)$ = Uncertainty magnitude,

n = Total number of measurements.

$$c_i = \frac{\partial f}{\partial x_i} \qquad \mathbf{(19)}$$

c_i = Sensitivity coefficient

<u>Expanded uncertainty value:</u>

$$U = k \times u_c(y) \qquad (\mathbf{20})$$

where

U = Extended measurement uncertainty

k = Coverage factor

$u_c(y)$ = Compound uncertainty

In line with the calculation procedure described above, measurement uncertainty of luminous flux is calculated and presented as an example of optical measurements in Table **16**.

Table 16: Measurement uncertainty of luminous flux (lm)

	Given or Expected Data	**Distrib. Type**	**Standard Measure. Uncertainty**	**Sensitivity Constant**	**Uncertainty Constant**	**Variant**
Reference Device or Related Uncertainty Components						
Spectrometer (Wavelength Calibration)	0.7	Normal	0.35	1	0.35	0.123
SCL 1400 Lamp	1	Normal	0.5	1	0.5	0.25
LPS 150 Power Supply (Direct Voltage)	0.005	Normal	0.0025	1	0.0025	0.000006
LPS 150 Power Supply (Direct Current)	0.005	Normal	0.0025	1	0.0025	0.000006

LPS 100 Power Supply (Direct Voltage)	0.005	Normal	0.0025	1	0.0025	0.000006
LPS 100 Power Supply (Direct Current)	0.005	Normal	0.0025	1	0.0025	0.000006
Agilent Power Supply (AC Voltage)	0.06	Normal	0.03	1	0.03	0.0009
Agilent Power Supply (Frequency)	0.01	Normal	0.005	1	0.005	0.00003
SCL 1400 Lamp Lifetime Uncertainty Constant	$3.2*10^{-5}$	Rectangle	$1.9*10^{-5}$	1	$1.8667*10^{-5}$	$3.5*10^{-10}$
Spectrometer Non-linearity Uncertainty Constant	0.06	Normal	0.03	1	0.03	0.0009
Spectrometer Light Leakage Uncertainty Constant	0.05	Rectangle	0.029	1	0.03	0.0008
Spectrometer Drift Related Uncertainty	0.05	Normal	0.025	1	0.025	0.0006
Sphere Space Absorptivity Uncertainty Constant	0.5	Normal	0.25	1	0.25	0.063
Sphere Non-uniformity Uncertainty Constant	0.2	Normal	0.1	1	0.1	0.01
Method Based Uncertainty						
Temperature Related Uncertainty	0.78	Rectangle	0.448	1	0.448	0.2
Air Velocity Related Uncertainty	0	Rectangle	0	1	0	0

Experiment Repeatability Related Uncertainty	2.51	Normal	1.256	1	1.256	1.578
						2.6
Overall Measurement Uncertainty	1.6					
Expanded Measurement Uncertainty	3.2					

APPENDIX B

B.1 Dimensions of the Initial Design of the Oven System

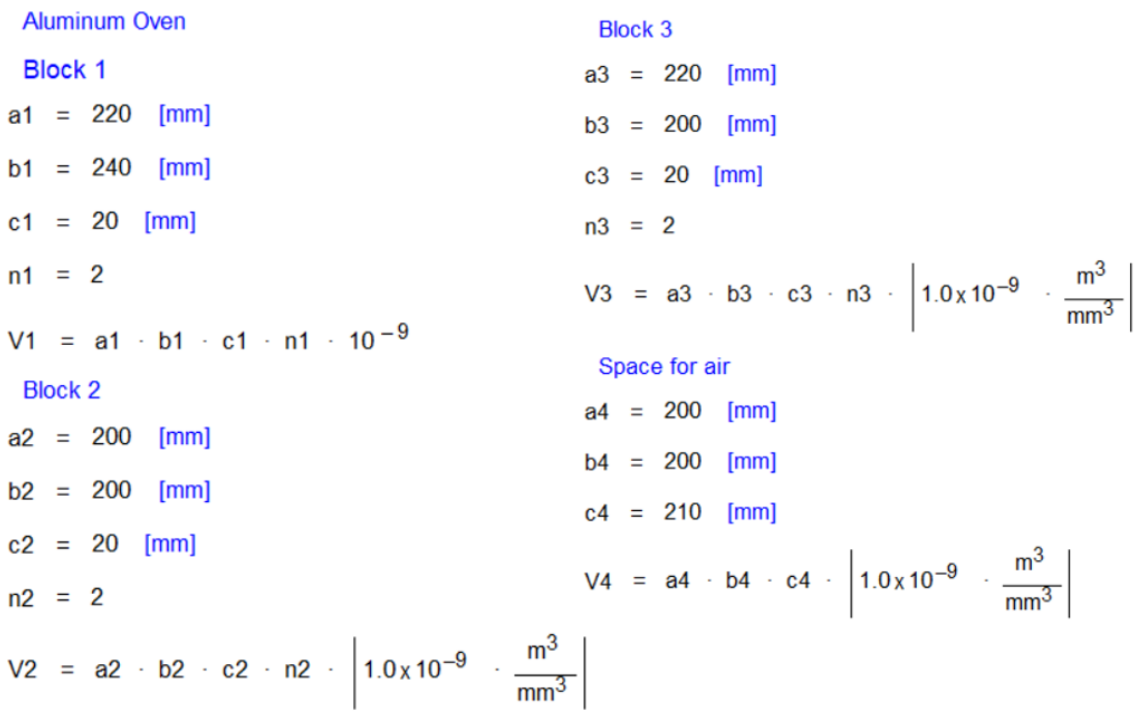

Aluminum Oven

Block 1

$a1 = 220$ [mm]

$b1 = 240$ [mm]

$c1 = 20$ [mm]

$n1 = 2$

$V1 = a1 \cdot b1 \cdot c1 \cdot n1 \cdot 10^{-9}$

Block 2

$a2 = 200$ [mm]

$b2 = 200$ [mm]

$c2 = 20$ [mm]

$n2 = 2$

$V2 = a2 \cdot b2 \cdot c2 \cdot n2 \cdot \left| 1.0 \times 10^{-9} \cdot \frac{m^3}{mm^3} \right|$

Block 3

$a3 = 220$ [mm]

$b3 = 200$ [mm]

$c3 = 20$ [mm]

$n3 = 2$

$V3 = a3 \cdot b3 \cdot c3 \cdot n3 \cdot \left| 1.0 \times 10^{-9} \cdot \frac{m^3}{mm^3} \right|$

Space for air

$a4 = 200$ [mm]

$b4 = 200$ [mm]

$c4 = 210$ [mm]

$V4 = a4 \cdot b4 \cdot c4 \cdot \left| 1.0 \times 10^{-9} \cdot \frac{m^3}{mm^3} \right|$

B.2 Formulation of the Required Cooling Performance and Heat Transfer Area of the Cooling System

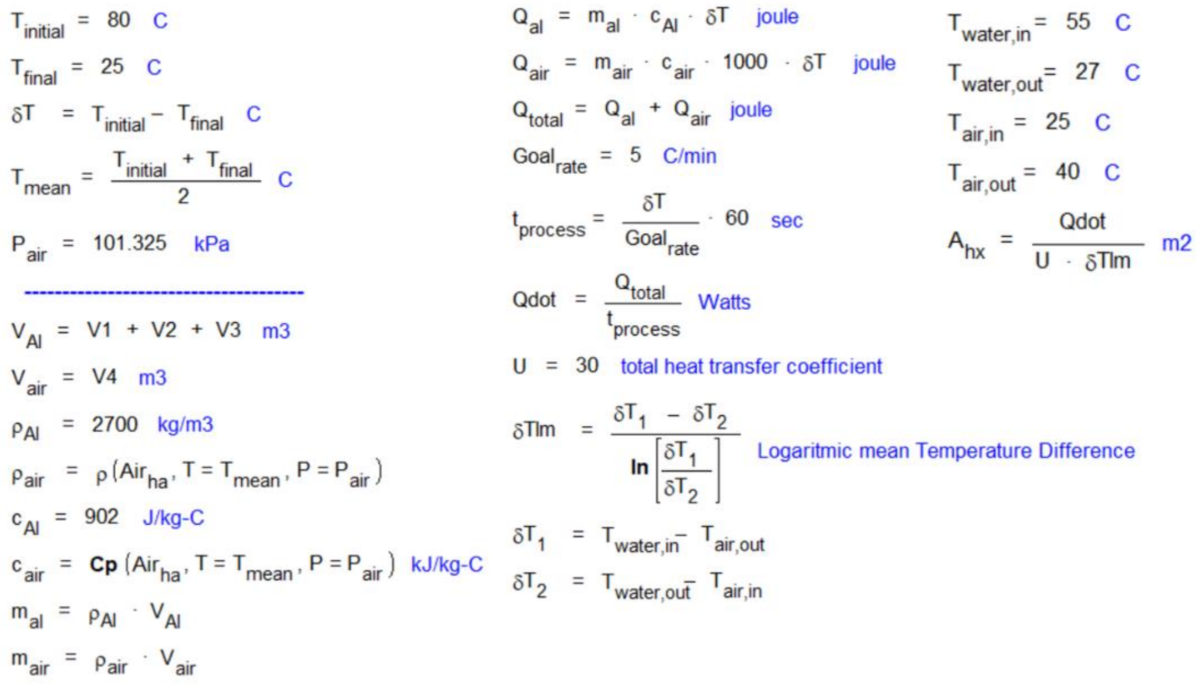

$T_{initial} = 80$ C

$T_{final} = 25$ C

$\delta T = T_{initial} - T_{final}$ C

$T_{mean} = \frac{T_{initial} + T_{final}}{2}$ C

$P_{air} = 101.325$ kPa

$V_{Al} = V1 + V2 + V3$ m3

$V_{air} = V4$ m3

$\rho_{Al} = 2700$ kg/m3

$\rho_{air} = \rho\left(Air_{ha}, T = T_{mean}, P = P_{air}\right)$

$c_{Al} = 902$ J/kg-C

$c_{air} = \mathbf{Cp}\left(Air_{ha}, T = T_{mean}, P = P_{air}\right)$ kJ/kg-C

$m_{al} = \rho_{Al} \cdot V_{Al}$

$m_{air} = \rho_{air} \cdot V_{air}$

$Q_{al} = m_{al} \cdot c_{Al} \cdot \delta T$ joule

$Q_{air} = m_{air} \cdot c_{air} \cdot 1000 \cdot \delta T$ joule

$Q_{total} = Q_{al} + Q_{air}$ joule

$Goal_{rate} = 5$ C/min

$t_{process} = \frac{\delta T}{Goal_{rate}} \cdot 60$ sec

$Qdot = \frac{Q_{total}}{t_{process}}$ Watts

$U = 30$ total heat transfer coefficient

$\delta Tlm = \frac{\delta T_1 - \delta T_2}{\ln\left[\frac{\delta T_1}{\delta T_2}\right]}$ Logaritmic mean Temperature Difference

$\delta T_1 = T_{water,in} - T_{air,out}$

$\delta T_2 = T_{water,out} - T_{air,in}$

$T_{water,in} = 55$ C

$T_{water,out} = 27$ C

$T_{air,in} = 25$ C

$T_{air,out} = 40$ C

$A_{hx} = \frac{Qdot}{U \cdot \delta Tlm}$ m2

B.3 Determination of Heat Transfer Area and Cooling Performance of the Cooling System

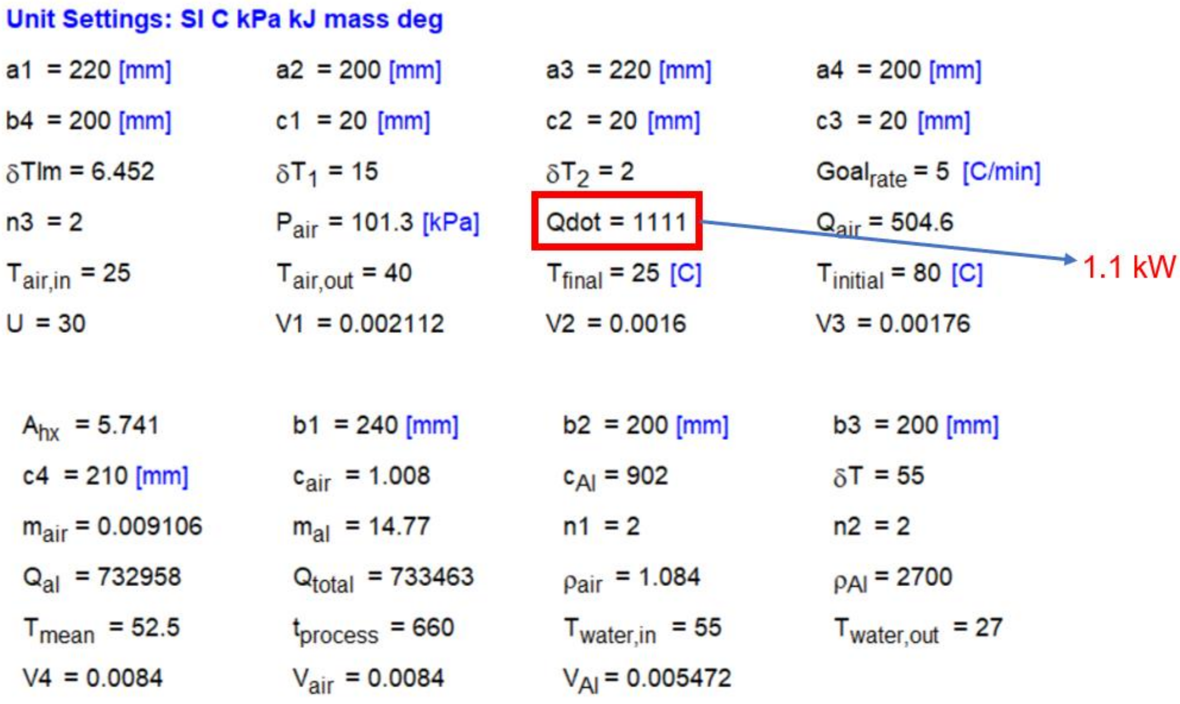

Unit Settings: SI C kPa kJ mass deg

a1 = 220 [mm]
a2 = 200 [mm]
a3 = 220 [mm]
a4 = 200 [mm]
b4 = 200 [mm]
c1 = 20 [mm]
c2 = 20 [mm]
c3 = 20 [mm]
$\delta Tlm = 6.452$
$\delta T_1 = 15$
$\delta T_2 = 2$
$Goal_{rate} = 5$ [C/min]
n3 = 2
$P_{air} = 101.3$ [kPa]
Qdot = 1111
$Q_{air} = 504.6$
$T_{air,in} = 25$
$T_{air,out} = 40$
$T_{final} = 25$ [C]
$T_{initial} = 80$ [C]
U = 30
V1 = 0.002112
V2 = 0.0016
V3 = 0.00176

1.1 kW

$A_{hx} = 5.741$
b1 = 240 [mm]
b2 = 200 [mm]
b3 = 200 [mm]
c4 = 210 [mm]
$c_{air} = 1.008$
$c_{Al} = 902$
$\delta T = 55$
$m_{air} = 0.009106$
$m_{al} = 14.77$
n1 = 2
n2 = 2
$Q_{al} = 732958$
$Q_{total} = 733463$
$\rho_{air} = 1.084$
$\rho_{Al} = 2700$
$T_{mean} = 52.5$
$t_{process} = 660$
$T_{water,in} = 55$
$T_{water,out} = 27$
V4 = 0.0084
$V_{air} = 0.0084$
$V_{Al} = 0.005472$

APPENDIX C

C.1 Equations of the Problem

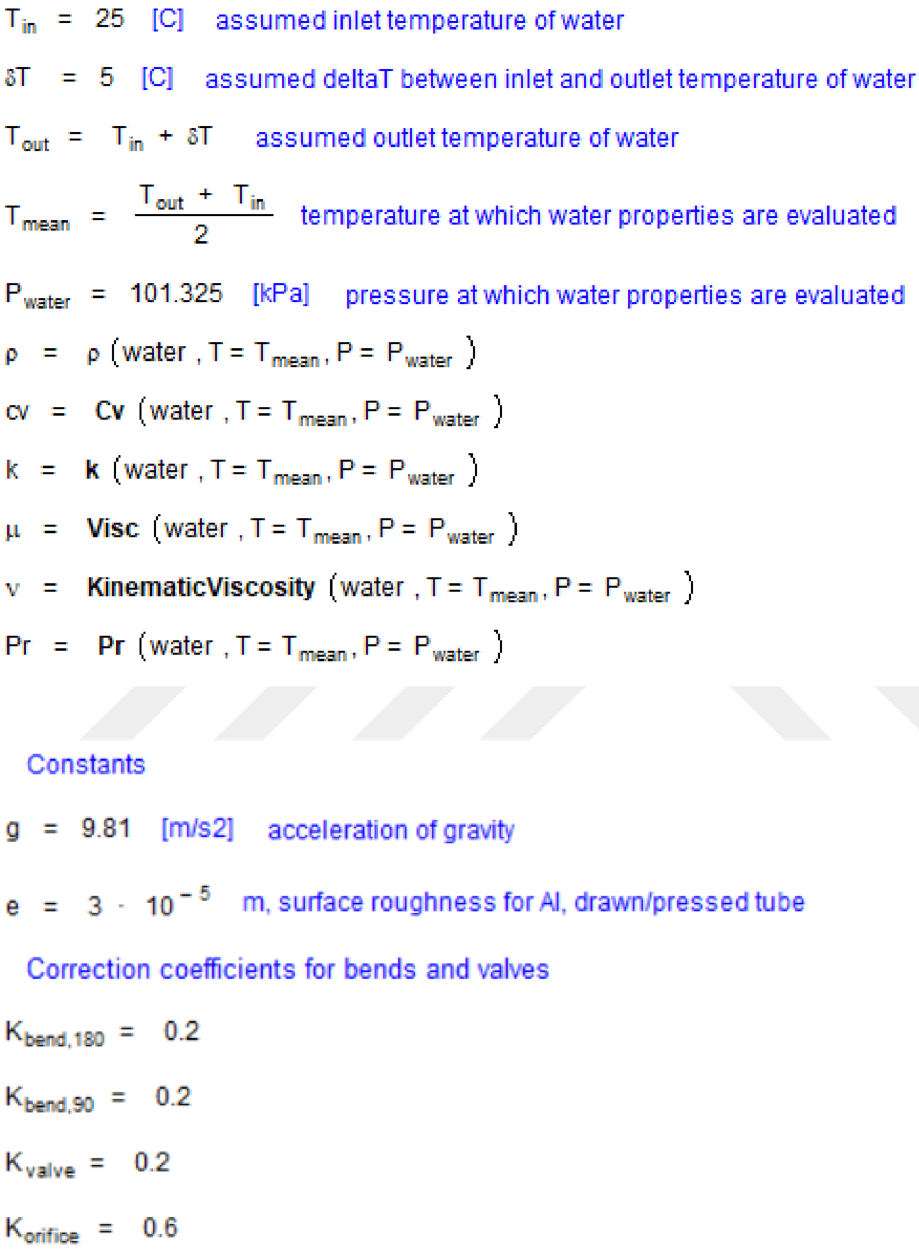

$T_{in} = 25$ [C] assumed inlet temperature of water

$\delta T = 5$ [C] assumed deltaT between inlet and outlet temperature of water

$T_{out} = T_{in} + \delta T$ assumed outlet temperature of water

$T_{mean} = \dfrac{T_{out} + T_{in}}{2}$ temperature at which water properties are evaluated

$P_{water} = 101.325$ [kPa] pressure at which water properties are evaluated

$\rho = \rho\,(water, T = T_{mean}, P = P_{water})$

$cv = \mathbf{Cv}\,(water, T = T_{mean}, P = P_{water})$

$k = \mathbf{k}\,(water, T = T_{mean}, P = P_{water})$

$\mu = \mathbf{Visc}\,(water, T = T_{mean}, P = P_{water})$

$\nu = \mathbf{KinematicViscosity}\,(water, T = T_{mean}, P = P_{water})$

$Pr = \mathbf{Pr}\,(water, T = T_{mean}, P = P_{water})$

Constants

$g = 9.81$ [m/s2] acceleration of gravity

$e = 3 \cdot 10^{-5}$ m, surface roughness for Al, drawn/pressed tube

Correction coefficients for bends and valves

$K_{bend,180} = 0.2$

$K_{bend,90} = 0.2$

$K_{valve} = 0.2$

$K_{orifice} = 0.6$

Oven system calculations

Tube specifications

$D_{holes} = 0.006$ [m] hydraulic diameter

$L_{channel} = 1.32$ [m] length of tube

$A_{channel} = \pi \cdot \frac{D_{holes}^{2}}{4}$ cross sectional area

$n_{bend,180,oven} = 0$ number of 180 degree return bends

$n_{bend,90,oven} = 50$ number of 90 degree bends

$n_{valve,oven} = 0$ number of valves

$$eoverD = \frac{e}{D_{holes}}$$

Turbulent flow assumption when Re >= 10000

$\dot{V}_{2,oven} = 4.2$ user input, volumetric flow rate in lpm

$\dot{V}_{m3s,oven} = \frac{\dot{V}_{2,oven}}{60000}$ volumetric flow rate in m3/s

$\dot{V}_{1,oven} = 3600 \cdot \dot{V}_{m3s,oven}$ volumetric flow rate in m3/h

$\dot{V}_{3,oven} = 0.22 \cdot \dot{V}_{2,oven}$ volumetric flow rate in gpm

$V_{mean,oven} = \frac{\dot{V}_{m3s,oven}}{A_{channel}}$ mean velocity of water

$$Re = \frac{V_{mean,oven} \cdot D_{holes}}{\nu}$$

$\frac{1}{\sqrt{f_{oven}}} = -1.8 \cdot \log \left[\frac{6.9}{Re} + \left[\frac{eoverD}{3.7} \right]^{1.11} \right]$ Turbulent flow, rough surface

S. E. Haaland, 1983 - Yunus Cengel Heat and Mass Transfer Textbook

$h_{major,oven} = f_{oven} \cdot \frac{L_{channel}}{D_{holes}} \cdot \frac{V_{mean,oven}^{2}}{2 \cdot g}$ major head loss

$h_{minor,oven} = n_{bend,180,oven} \cdot K_{bend,180} \cdot \frac{V_{mean,oven}^{2}}{2 \cdot g} + n_{bend,90,oven} \cdot K_{bend,90} \cdot \frac{V_{mean,oven}^{2}}{2 \cdot g}$

$+ \, n_{valve,oven} \cdot K_{valve} \cdot \frac{V_{mean,oven}^{2}}{2 \cdot g}$ minor head loss

$h_{total,oven} = h_{major,oven} + h_{minor,oven}$ total head loss

$\delta P_{total,pascal,oven} = \rho \cdot g \cdot h_{total,oven}$ pressure drop in pascal

$\delta P_{total_{oven}} = \delta P_{total,pascal,oven} \cdot 10^{-5}$ pressure drop in bar

$W_{pump,oven} = \dot{V}_{m3s,oven} \cdot \delta P_{total,pascal,oven}$ required pump power

C.2 Solution of the Problem

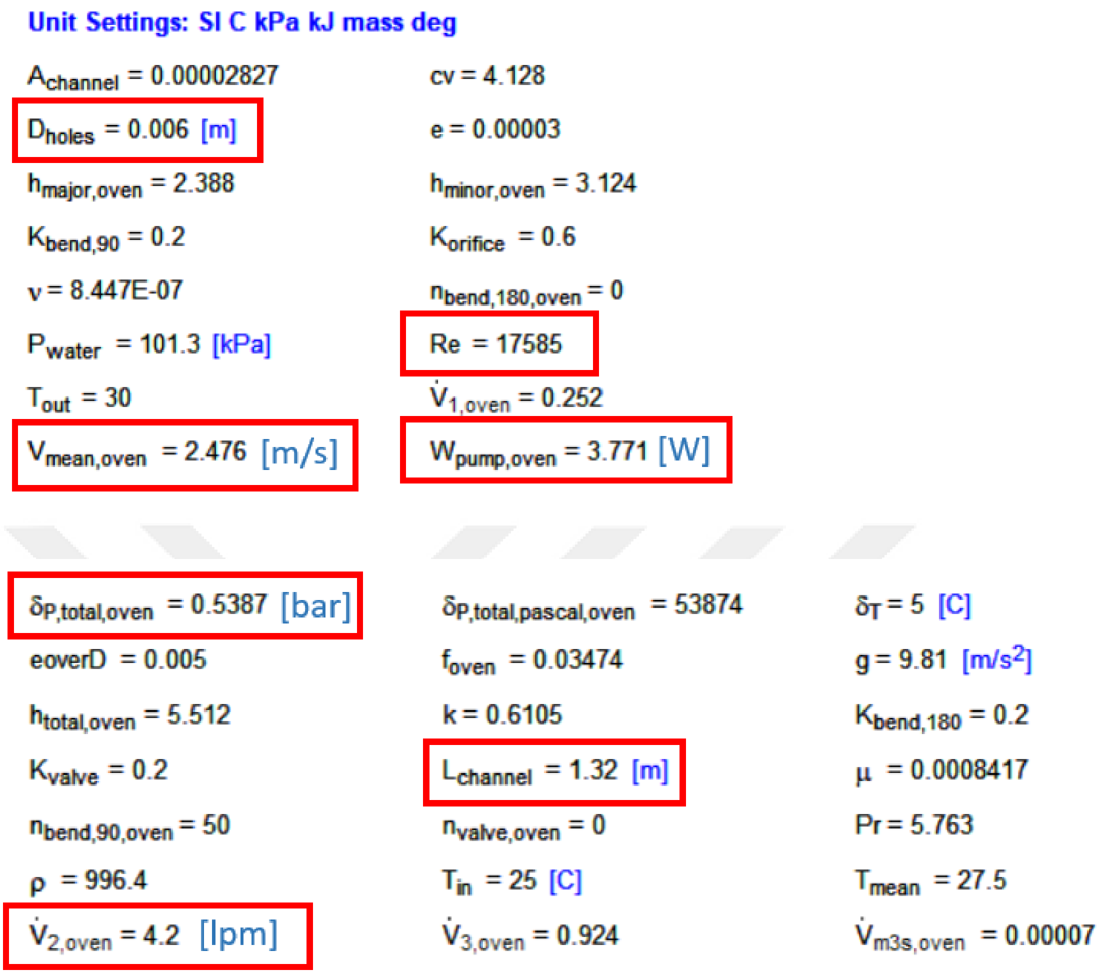

Unit Settings: SI C kPa kJ mass deg

$A_{channel}$ = 0.00002827

D_{holes} = 0.006 [m]

$h_{major,oven}$ = 2.388

$K_{bend,90}$ = 0.2

ν = 8.447E-07

P_{water} = 101.3 [kPa]

T_{out} = 30

$V_{mean,oven}$ = 2.476 [m/s]

cv = 4.128

e = 0.00003

$h_{minor,oven}$ = 3.124

$K_{orifice}$ = 0.6

$n_{bend,180,oven}$ = 0

Re = 17585

$\dot{V}_{1,oven}$ = 0.252

$W_{pump,oven}$ = 3.771 [W]

$\delta_{P,total,oven}$ = 0.5387 [bar]

eoverD = 0.005

$h_{total,oven}$ = 5.512

K_{valve} = 0.2

$n_{bend,90,oven}$ = 50

ρ = 996.4

$\dot{V}_{2,oven}$ = 4.2 [lpm]

$\delta_{P,total,pascal,oven}$ = 53874

f_{oven} = 0.03474

k = 0.6105

$L_{channel}$ = 1.32 [m]

$n_{valve,oven}$ = 0

T_{in} = 25 [C]

$\dot{V}_{3,oven}$ = 0.924

δ_T = 5 [C]

g = 9.81 [m/s^2]

$K_{bend,180}$ = 0.2

μ = 0.0008417

Pr = 5.763

T_{mean} = 27.5

$\dot{V}_{m3s,oven}$ = 0.00007

C.3 Impact of Different Variables on Pressure Drop and Pumping Power

Table 17: The impact of temperature difference (between outlet and inlet water) on pressure drop and pumping power

ΔT (°C)	ΔP (Bar)	W_{pump} (W)
5	0.5387	3.771
10	0.537	3.759
15	0.5354	3.748
20	0.5338	3.736
25	0.5322	3.726
30	0.5307	3.715
35	0.5293	3.705
40	0.5279	3.695
45	0.5265	3.686
50	0.5252	3.676

Table 18: The impact of coolant channel diameter on pressure drop and pumping power

Diameter of coolant (mm)	Pressure drop (Bar)	Pumping power (W)
5.0	1.227	8.59
5.3	0.942	6.59
5.7	0.664	4.65
6.1	0.500	3.50
6.5	0.389	2.72
7.2	0.243	1.70
7.9	0.159	1.11
8.6	0.108	0.76
9.4	0.076	0.54
10.1	0.055	0.39
10.8	0.041	0.29
11.6	0.031	0.22
12.3	0.024	0.17
13.0	0.019	0.13

Table 19: The impact of total channel length on pressure drop and pumping power

Channel length (m)	Pressure drop (Bar)	Pumping power (W)
0.4	0.376	2.63
0.7	0.429	3.00
1.0	0.482	3.38
1.3	0.535	3.75
1.6	0.588	4.12
1.9	0.641	4.49
2.2	0.694	4.86
2.5	0.747	5.23
2.8	0.800	5.60
3.1	0.854	5.97

Table 20: The impact of volumetric flow rate on pressure drop and pumping power

Volumetric flow rate (L/min)	Pressure drop (Bar)	Pumping power (W)
0.5	0.009	0.01
1.5	0.074	0.18
2.5	0.197	0.82
3.5	0.378	2.20
4.5	0.617	4.62
5.5	0.913	8.37
6.5	1.268	13.74
7.5	1.680	21.00
8.5	2.151	30.47
9.5	2.679	42.41

LIST OF PUBLICATIONS

No	Title	Conference /Journal Name	Status	Date
1	A Comparative Study for the Junction Temperature of Green Light Emitting Diodes (LED)s	IEEE Transactions on Components, Packaging and Manufacturing Technology (CPMT)	Published	2019
2	Investigation into Optothermal Behavior of a High Power Red Light Emitting Diode (LED) Considering the Impact of an LED dome	ASME Journal of Electronics Packaging (JEP)	Accepted	2019
3	Impact of Electronics over Localized Hot Spots in Multi-Chip White LED Light Engines	IEEE, ITHERM Conference	Published	2019
4	Challenges for Measuring Multi-chip LED Light Engines for Interior Lighting Applications	LED Professional (LpS) Conference	Published	2019
5	A New Approach for Fast and Accurate Measurement of Light Emitting Diodes Junction Temperatures	LED Professional, May/June 2019	Published	2019
6	Thermal and Optical Challenges for Solid State Automotive Lighting Applications	LED Professional, March/April 2019	Published	2019
7	An Investigation into Phase Change Materials for Thermal Management and Efficiency Improvement of Photovoltaic Power Harvesting Systems	14th International Conference on Heat Transfer, Fluid Mechanics and Thermodynamics (HEFAT)	Published	2019
8	Impact of Junction Temperature over Forward Voltage Drop for Red, Blue and Green High Power Light Emitting Diodes	IEEE, ITHERM Conference	Published	2017
9	Enhanced Thermal Performance of High Flux LED Systems with Two-Phase Immersion Cooling		In Progress	
10	Rapid Heating and Cooling Chamber for Photonics Junctions Measurement System		In Progress	

VITA

Ahmet Mete Muslu

Research Areas
Investigation of optothermal characteristics of high-power photonic systems and development of thermal measurement techniques with analytical, computational and experimental studies.

M.Sc.
Ozyegin University, 2019

B. Sc. Graduate
Ozyegin University, 2018

Ahmet Mete Muslu obtained his B.Sc. in Mechanical Engineering from Ozyegin University in 2018. Currently, he is pursuing the M.Sc. degree at Ozyegin University, focusing on optothermal characterization of photonic systems and developing a junction temperature measurement device for those systems.

During his studies, he was funded as a research assistant by the Scientific and Technological Research Council of Turkey (TÜBİTAK) under the contract number of 217M357. He also took an active role in the establishment of a laboratory management system for Energy Efficient Electronics and Lighting Technologies Research, Development and Demonstration Center (EVATEG) Laboratory. He both undertook technical and management roles in a highly motivated team, and he was responsible for quality control assessment, risk management and uncertainty analysis of lighting systems.

At the end of his studies, 2 journals, 4 conference papers, 2 articles for LED professional Review and 2 patents (pending) have been served to the literature. Furthermore, under the mentorship of Prof. Dr. Mehmet Arık, he was honored by Defense Advanced Research Projects Agency (DARPA), with the "Best Commercial Potential Product" award in the RevCon Thermal Connector Design Competition. He also won the 3rd prize with the EVAtherm project in the Project and Idea Category of the 7th Entrepreneurship Awards Program organized by the Entrepreneurial Businessmen Foundation (GIV).